University of Alberta
Department of Civil &
Environmental Engineering

Structural Engineering Report No. 274

Fatigue of Steel Plate – Elastomer Composite Beams

by

Gary K. Lui

and

Scott D.B. Alexander

December, 2007

Fatigue of Steel Plate – Elastomer Composite Beams

by

Gary. K. Lui
and
S.D.B. Alexander

Structural Engineering Report 274

Department of Civil and Environmental Engineering
University of Alberta
Edmonton, Alberta

December, 2007

ABSTRACT

The test program consists of two sandwich plate system specimen sets, each with six specimens. Five specimens from each set are tested under cyclic loading. The remaining specimen of each set is tested under monotonic load. Ancillary tests measure properties of steel-elastomer interfaces, elastomer and steel layers. Steel surface and interface are fatigue critical locations. Favourable interface properties, such as higher interface shear capacity and surface roughness, improve the fatigue strength of the interface, so that the member is steel fatigue critical. Consequently, the torsion test shows potentials as a quality control tool for interface fatigue strengths. Two deflection models examined are energy and coupled shear wall. The coupled shear wall model provides reasonable estimates of deflection. The energy model provides practical deflection equations, but overestimates the deflection. A consistent ratio between the results from the two models suggests results of one model can approximate results for the other model.

ACKNOWLEDGEMENTS

This research project was made possible by the generosity of Intelligent Engineering with both financial and information support. Insights from Dr. D. L. Kennedy were always helpful and informative.

TABLE OF CONTENT

LIST OF TABLES

LIST OF FIGURES

LIST OF SYMBOLS

General

A	=	Cross sectional area
c	=	Distance from neutral axis to extreme fiber
E	=	Modulus of elasticity
E_e	=	Elastomer modulus of elasticity
E_s	=	Steel modulus of elasticity
G	=	Shear modulus of elasticity
I	=	Moment of Inertia
I_t	=	Transformed moment of inertia
J	=	Polar moment of Inertia
L	=	Half-span length
M	=	Moment
n	=	Transformation ratio
P	=	Applied point load
Q	=	First moment of area with respect to neutral axis
Q_t	=	First moment of the transformed area to the neutral axis
T	=	Torque
t_e	=	Elastomer thickness
t_s	=	Steel plate thickness
V	=	Shear force
δ	=	Deflection
ε	=	Strain
γ	=	Shear angle
ν	=	Poisson's ratio
σ	=	Normal stress
τ	=	Shear stress
τ_{avg}	=	Average shear stress
τ_{max}	=	Maximum shear stress

Energy Model

U	=	Strain energy
U_m	=	Flexural strain energy
U_s	=	Shear strain energy
δ_m	=	Flexural deflection
δ_v	=	Shear deflection

Coupled Shear Wall Model

b	=	Shear medium thickness
d	=	Half thickness of flexural element
H	=	Length of the half span
k	=	Geometry factor
l	=	center to center distance between flexural elements
N	=	Axial force
q	=	Shear flow
w	=	width of composite beam
α	=	Geometric and material factor
δ_1	=	Deflection from bending moment
δ_2	=	Deflection from shear force
δ_3	=	Deflection from axial force

Torsion

L	=	Thickness of elastomer
r	=	Radius to the extreme fiber
φ	=	Angle of rotation

Interface Strain Calculations

b	=	Total specimen width
h	=	Total specimen height
l	=	Distance between strain gauges
t	=	Steel plate thickness

Creep

δ_i	=	Individual deflection amount
δ_o	=	Initial elastic deflection
φ	=	Creep coefficient

1 INTRODUCTION

1.1 Background

Sandwich Plate System (SPS) is a composite plate, designed as an alternative to stiffened steel plates. SPS plates consist of metal exterior layers, usually steel, and an elastomer inner core. The outer layers provide flexural capacity and the inner core is responsible for shear. Some of the structural and maritime applications for the SPS include rehabilitation and new construction of ship decks, hulls, and bridge structures. Because SPS is utilized for elements that experience repeat loadings, fatigue and deflection properties of SPS beams are factors that influence design.

1.2 Scope and Objectives

Two sets of SPS beams, each with six specimens, were used for the test program. Five specimens from each set were tested under dynamic cyclic loading. The remaining specimen of the set was tested under slower monotonic static loads. Ancillary tests provided estimates of the steel and elastomer material properties. Additional ancillary tests measured the shear strength of the interface.

There are four main objectives for the program. The first objective is to document the fatigue life of the SPS beams. Possible factors that influence the fatigue life are also identified. The second objective is to measure deformations of SPS members and identify appropriate deflection models. The third objective is to identify potential quality control tests for the steel-elastomer interface. The fourth objective is to investigate the possibility of simplifying the SPS fatigue test program by bypassing static tests.

2 BACKGROUND INFORMATION

2.1 Introduction

Although research on other composite sandwich systems is available, fatigue results specific to the Sandwich Plate System (SPS) are not in the public domain. As a result, other research is relevant to SPS by illustrating factors that are critical for other sandwich systems.

Four areas of interest will be presented in this chapter. First, relevant work by other researchers are listed. Second, the background information of the sandwich plate system is discussed. Third, general fatigue principles and factors that affect fatigue strength are briefly reviewed. Last, two possible deflection models for the SPS are explored for the SPS.

2.2 Related Work

Different aspects of sandwich systems, with various material and configurations, have been study by others.

Bistac, Vallat, and Schultz (1995) studied the adhesion properties for polymer and steel sandwiches. Thin layers of polymer are inserted between steel sheets, and the strength of the bond was tested by a wedge test. It was found that the surface treatment of the steel influences the adhesive behavior of the bond.

The surface treatment of the steel was also the focus of Naito, Hirakata, and Fujii (1998). A conclusion of Naito et al. (1998) is that fatigue crack propagation occurs at different locations depending on the surface treatment of the adherend, but under static loading, cracks propagated in the adhesive layer regardless of surface treatments. Another finding is that the fatigue crack growth resistance of the adhesive is dependent on the surface treatment.

Tsai, Doyle, and Sun (1985) show that fatigue strength of a graphite/epoxy composite is dependent on strain level and frequency of loading. From their experimental

work, the fatigue life of the graphite/epoxy composite is directly proportional to the loading frequency.

Blanchard, Chateauminois, and Vincent (1996) did similar work. A conclusion from their work is that the strength of a joint is dependent on the strain rate and joint thickness. The failure mode changes from cohesive failure at the interface to the failure of the adhesive depending on joint thickness and strain rates. Fatigue tests were earned out at imposed strain amplitude (Blanchard et al., 1996).

Previous researchers have studied the contribution of adhesives, Melander, Linder, Stensiö, Larsson, Gustasson and Björkman (1999) show the effects on fatigue strength of bonded steel sheets by defect configurations. They found that the stiffness of the composite system varies depend on bonding defect configurations. The fatigue strength of the composite system also differs by defect configuration.

Surface treatment, strain rate, and bonding interface are some of the factors that affect the fatigue properties of a composite structural system.

2.3 Sandwich Plate System

Sandwich plate system, SPS, is a composite structural system that bonds two layers of metal with a continuous polyurethane elastomer layer in the middle. Designed as an alternative to stiffened metal plates, SPS reduces welding associated with stiffeners. The elastomer provides damping, bonding, stabilizing, and shear capacity characteristics.

2.3.1 SPS Applications

SPS can be used both in new design or rehabilitation. Applications of SPS can be maritime or civil engineering oriented. Examples of SPS applications are ship decks, river barges and hulls and bridge decks.

2.3.2 Material Properties

Although SPS can be a product of various exterior metals, steel will be the material discussed because the test specimens have steel plates at the surface. Typical yield strength of steel is 350 MPa. A report from Intelligent Engineering (2003) shows that the elastomer material properties vary with temperature. The modulus of elasticity for the elastomer ranges from 4000 MPa at –80°C to 250 MPa at 80°C. The ultimate strength of the elastomer also varies significantly depending on temperature (85 MPa for -80°C and 10 MPa for 80°C).

2.3.3 Manufacturing Process

There are four stages in the manufacture of a new SPS panel. Figure 2.1 shows the components and schematic of the SPS during manufacturing. The first stage is to prepare the steel surface at the interface by grit blasting. The steel surfaces must be cleaned and dry for proper bonding with the elastomer. The prepared surface requires a surface roughness of 60 μm. The second stage is the welding of perimeter bars and a top steel plate to a bottom plate. Perimeter bars acts as spacers between the two steel plates and divide the cavity between the two plates to form closed cells. The third stage is injecting the elastomer, as a two-part liquid, into the cells. Liquid elastomer is applied at the injection hole at the center of the closed cell until the cavity is filled. Excess liquid elastomer escape through the exhaust vents. The final stage is the curing of the elastomer. The elastomer will set in 10 to 12 minutes and the curing is usually completed in 3 to 4 hours. The elastomer curing process is exothermic, resulting in residual compressive stresses in the steel and residual tensile stresses in the elastomer.

The process for an SPS overlay is similar to that of a new panel, the main difference being that the existing deck serves as the bottom plate.

2.4 Fatigue

2.4.1 Definition

Fatigue failures are caused by diminished strength and ductility of a member because of repeating, fluctuating, alternating stresses below yielding (Ugural & Fenster, 1995). The localized yielding of a member causes the fatigue failures with stresses that are normally in the elastic range (Barsom & Rolfe, 1999). The number of fatigue loading cycles to cause failure defines fatigue life. Boresi and Sidebottom (1985) list two general types of fatigue failures. The two types of fatigue are low cycle with large strains and high cycles with small strains. Fatigue can cause brittle failure in ductile materials. In design, the fatigue life of a member is estimated by s-n curves.

2.4.2 Crack Initiation

The fatigue life of a member is generally dominated by the crack initiation stage. Crack initiation is also referred to as stage I crack. Origins of cracks can be microscopic imperfections in the surface or at high stress concentration locations such as abrupt geometric and material changes (Ugural & Fenster, 1995). Member surfaces are often stress concentration location because of the typically higher stresses and scratches. As the member is loaded, the surface may be subjected to stresses beyond the elastic limit and results in extrusions and intrusions. While tensile and shear loads are dominating factors for fatigue, compressive loads have relative insignificant effects. There are three basic modes of loading for the crack tip: opening, sliding and tearing mode. The opening mode is the predominating stress state for most practical situations. (Ewalds & Wanhill, 1989)

2.4.3 Crack Propagation

The propagation stage, also referred to as stage II crack, is the crack growth after crack initiation. A stress intensity factor is a measure of the stress and strain environment

of the crack tip (Broek, 1989). Any number of cracks with the same stress environment (stress intensity) will show similar crack propagation rates. Using a stress intensity range (numerical difference between the maximum and the minimum stress intensity), the crack growth rate can be estimated by the Paris equation or the Foreman equation (Ewalds & Wanhill, 1989). Fatigue failures occur when the crack reaches a critical crack size.

2.4.4 Endurance Limit

Boresi and Sidebottom (1985) define an endurance limit as a stress level below which a material can resist repeated cyclic stress indefinitely without any evidence of fracture. Generally, an endurance limit is evident for steel. Other materials do not show a distinct endurance limit.

2.4.5 Factors Affecting Fatigue

The primary factor that affects fatigue strength is the fluctuation in the localized stress or strain (Barsom & Rolfe, 1989). Combined stress conditions (uniaxial, biaxial, or bending) can reduce the fatigue life significantly (Fenster & Ugural, 1995). With varying stress levels, the cumulative damage in fatigue can be estimated by the Miner method (Miner, 1945). Boresi and Sidebottom (1985) list some factors that affect the fatigue properties are the frequency of loading, residual stresses, surface conditions, and mean stress. Weibull (1961) lists grain size, surface condition, size and shape of test specimens, and types of loading as factors that influences fatigue results. Weibull (1961) states that fatigue strength of a bending test would be higher than axial test if the maximum stresses were the same.

2.4.6 Residual Stresses

Manufacturing processes cause residual stresses in structural elements. Weibull (1961) states that the presence of residual stress could be either beneficial or detrimental to the fatigue strength of a member. The reason is that the residual stress are additive to stresses caused by external loads. Under fatigue loading, a member with residual tensile stress of will experience a larger tensile stress compared to one with residual compressive stress.

2.5 Mathematical Deflection Models

2.5.1 Energy Method

2.5.1.1 Introduction

The energy method is chosen for its ability to calculate flexural and shear deformations. Castigliano's theorem for deflection calculation is based on the strain energy. As a result, the model is valid in the linear elastic region with small deflections (Boresi & Sidebottom, 1985).

2.5.1.2 Derivation

The member deflection, δ, can be determined by the first derivative of the strain energy, U, with respect to a force, P, acting at the point of the member in the direction of the deflection shown in equation 2.1. The total strain energy, U is the summation of the flexure, U_m, and shear components, U_s, shown in equation 2.2. The flexural deflection is a function of the applied moment, M, Elasticity, E, and moment of inertia, I. The shear deflection is a function of the shear force, V, shape factor, α, cross-section area, A, and shear modulus, G. Equation 2.3 is the general equation for mid-span deflection with the current experimental setup, which is shown in figure 2.2.

$$\delta = \frac{\partial U}{\partial P} \qquad [2.1]$$

$$U = U_m + U_s = \int_0^L \frac{M^2 dz}{2EI} + \alpha \int_0^L \frac{V^2 dz}{2AG} \qquad [2.2]$$

$$\delta = \frac{PL^3}{6EI} + \frac{\alpha PL}{2GA} \qquad [2.3]$$

2.5.2 Coupled Shear Wall Analogy

2.5.2.1 Introduction

From a geometrical perspective, a sandwich plate panel is similar to a coupled shear wall. Both systems consist of two flexural components that are connected by a shearing element as shown in figure 2.3.

Coupled shear walls are used in tall buildings to resist the lateral loads imposed by either wind or earthquake. A coupled shear wall consists of parallel walls that are connected at each floor by a coupling beam. In addition to physical size, the two systems differ in the nature of their shearing element. A coupled shear wall is connected with discrete beams whereas the SPS has a continuous medium in between the steel plates.

The derivation of the deflection model follows that given by Smith and Coull (1991). Because of the material distribution of the SPS, some of the derivation of the coupled shear wall method was modified.

2.5.2.2 Method Assumptions

The continuous medium method, developed for coupled shear walls, is now applied to SPS panels. A coordinate system is shown in figure 2.3. There are four assumptions for the analysis:

1. The properties of flexural elements and the connecting shearing medium are constant along the length of the panel.
2. Plane sections of the shearing element before loading remain plane after loading.
3. Shearing element does not carry any significant load in the y-direction.
4. At any point along the length of the panel, the flexural elements have the same deformed shape. The assumed stiffness of the shearing component in the z-direction is infinite.

2.5.2.3 Derivation

Following the derivation in Smith and Coull (1991), the only forces acting at the shearing layer are the shear flow, *q*, and contact forces, *n*, shown by the free body diagram in figure 2.4. The axial force, *N*, is equal to the integral of the shear flow above the shearing element. Thus the axial force, *N*, is calculated as equation 2.4 and the differential form is equation 2.5.

$$N = \int_z^H q\,dz \qquad [2.4]$$

$$q = -\frac{dN}{dz} \qquad [2.5]$$

Consider the displacement compatibility of the elastomer layer along the z-axis. There are three components to the lateral displacement of the shearing layer at mid-height. Component δ_1 is shown in figure 2.5, results from the bending of the flexural members. The second component, δ_2, shown in figure 2.6 is the result of shearing deformations within the elastomer layer. The last component, δ_3, is caused by axial deformation of the flexural members illustrated in figure 2.7. The three components are calculated with equations 2.6 to 2.8. Where *b* is the thickness of the elastomer, *d* is half of the flexural element thickness, and *w* is the width of the beam. A_1 and A_2 are the area of the flexural members respectively.

$$\delta_1 = \left(\frac{b}{2} + d_1\right)\frac{dy}{dz} + \left(\frac{b}{2} + d_2\right)\frac{dy}{dz} = l\frac{dy}{dz} \qquad [2.6]$$

$$\delta_2 = \frac{-qb}{wG} = \frac{b}{wG}\frac{dN}{dz} \qquad [2.7]$$

$$\delta_3 = -\frac{1}{E}\left(\frac{1}{A_1} + \frac{1}{A_2}\right)\int_0^z N dz \qquad [2.8]$$

Compatibility requires that the sum of all of the relative displacement components be equal to zero.

$$\delta_1 + \delta_2 + \delta_3 = 0 \qquad [2.9]$$

Substituting equations 2.6, 2.7, and 2.8 into 2.9 results in equation 2.10.

$$l\frac{dy}{dz} + \frac{b}{wG}\frac{dN}{dz} - \frac{1}{E}\left(\frac{1}{A_1} + \frac{1}{A_2}\right)\int_0^z N dz = 0 \qquad [2.10]$$

Differentiating equation 2.10 gives:

$$l\frac{d^2y}{dz^2} + \frac{b}{wG}\frac{d^2N}{dz^2} - \frac{N}{E}\left(\frac{1}{A_1} + \frac{1}{A_2}\right) = 0 \qquad [2.11]$$

With the flexural bending from the applied moment and the reverse bending from the elastomer shearing and axial forces, the moment-curvature relationship of the two steel plates is described as follows. Where I_1 and I_2 are the moment of inertia for the two flexural elements and l is the half span length of the member.

$$E(I_1 + I_2)\frac{d^2y}{dz^2} = M - l\int_z^H q dz = M - lN \qquad [2.12]$$

Smith and Coull (1991) mathematically manipulate and solve equation 2.12. Following the solution given by Smith and Coull (1991) and applying the properties of the SPS, α^2 and k^2 of equation 2.13 are defined by equations 2.14 and 2.15.

$$\frac{d^2N}{dz^2} - \alpha^2 k^2 N = -\frac{\alpha^2}{l}M \qquad [2.13]$$

$$\alpha^2 = \frac{wGl^2}{Eb(I_1 + I_2)} \qquad [2.14]$$

$$k^2 = \frac{(I_1 + I_2)}{A_1 l^2} + \frac{(I_1 + I_2)}{A_2 l^2} + 1 \qquad [2.15]$$

Figure 2.8 shows the boundary conditions for the current experiment. Applying simply supported boundary conditions to the solutions given by Smith and Coull (1991),

equation for shear flow and mid-span deflection, *y*, are shown as equations 2.16 and 2.17. F_2 and F_3 are the shear flow and deflection factors, respectively.

$$-\frac{dN}{dz} = q = \frac{V}{k^2 l}\left[1 - \frac{\cosh k\alpha(H-z)}{\cosh k\alpha H}\right] = \frac{V}{k^2 l}F_2 \qquad [2.16]$$

$$y = \frac{VH^3}{3EI}\left[1 - \frac{3}{k^2}\left(\frac{1}{3} + \frac{\sinh\ k\alpha H}{(k\alpha H)^3 \cosh\ k\alpha H} - \frac{1}{(k\alpha H)^2}\right)\right] = \frac{VH^3}{3EI}F_3 \qquad [2.17]$$

Graphical forms of F_2 and F_3 are shown in figures 2.9 and 2.10.

2.6 Conclusion

From other researches, there are three major factors that affect the fatigue strength of sandwich systems. The surface treatment of the layers influences the bonding quality of the sandwich system. The fatigue strength of sandwich systems is directly proportional to the strain rate. Size and configuration of bonding defects affect the stiffness of the sandwich system.

Typical physical properties, manufacturing process, and applications of the sandwich plate system were described. SPS is intended as an alternative to stiffened steel plates. Because some SPS applications involve cyclic loading, experimental data for the fatigue strength of SPS is warranted. As a result, some general fatigue concepts and factors affecting the fatigue strength were reviewed.

Because deflection can be a critical limit in design, two deflection models for the SPS were explored. The experimental data obtain can be used to evaluate the two deflection models.

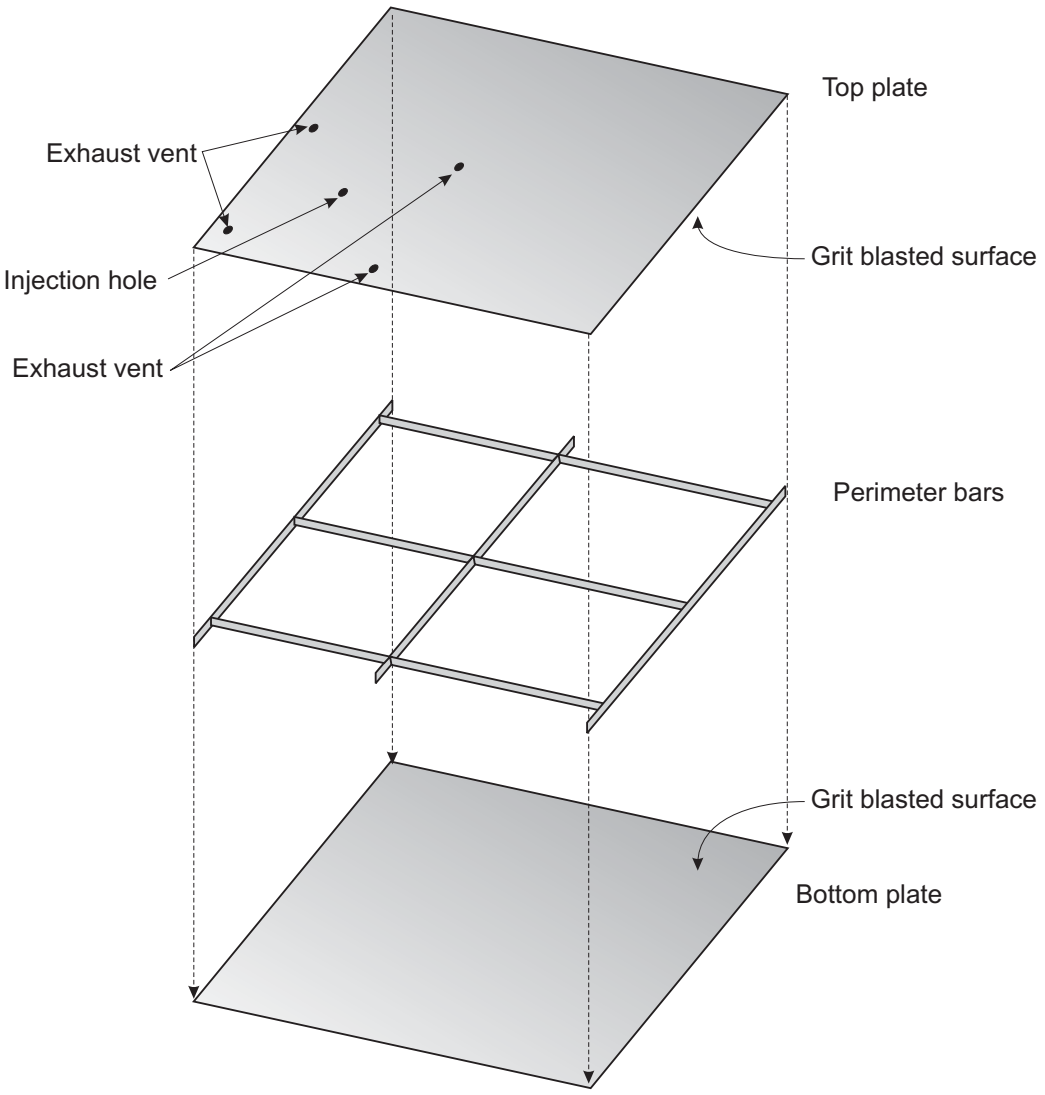

Figure 2.1: SPS components.

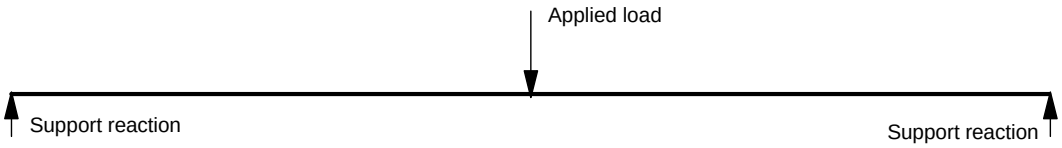

Figure 2.2: Free body diagram for current experiment.

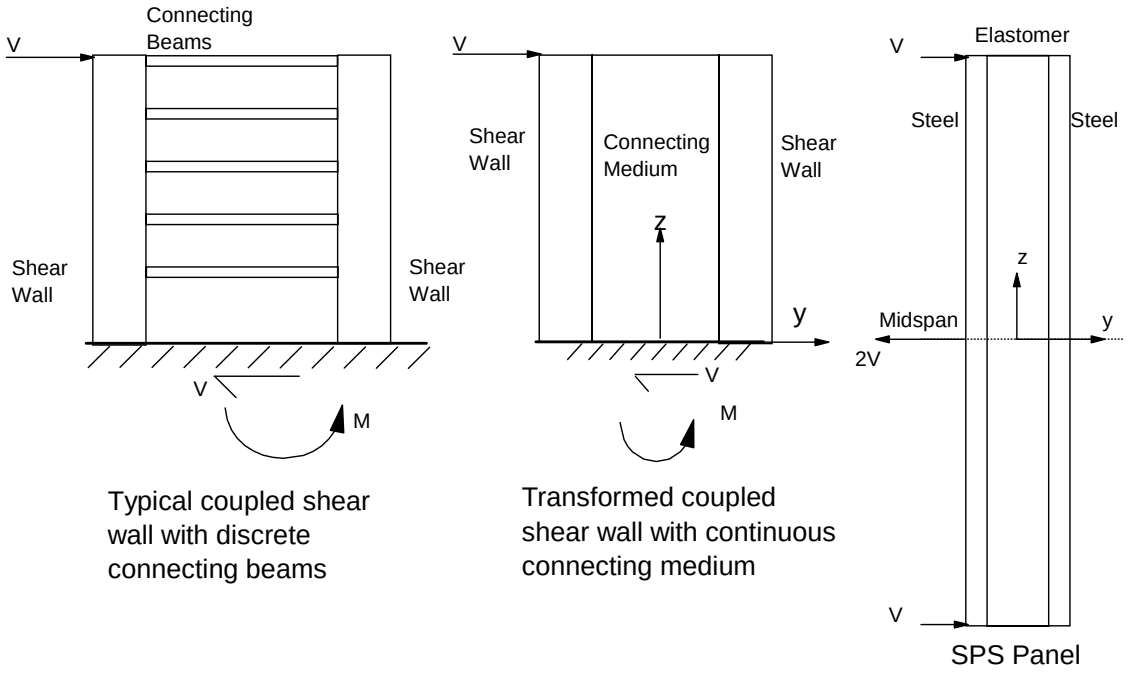

Figure 2.3: Coupled shear wall and SPS panel similarities.

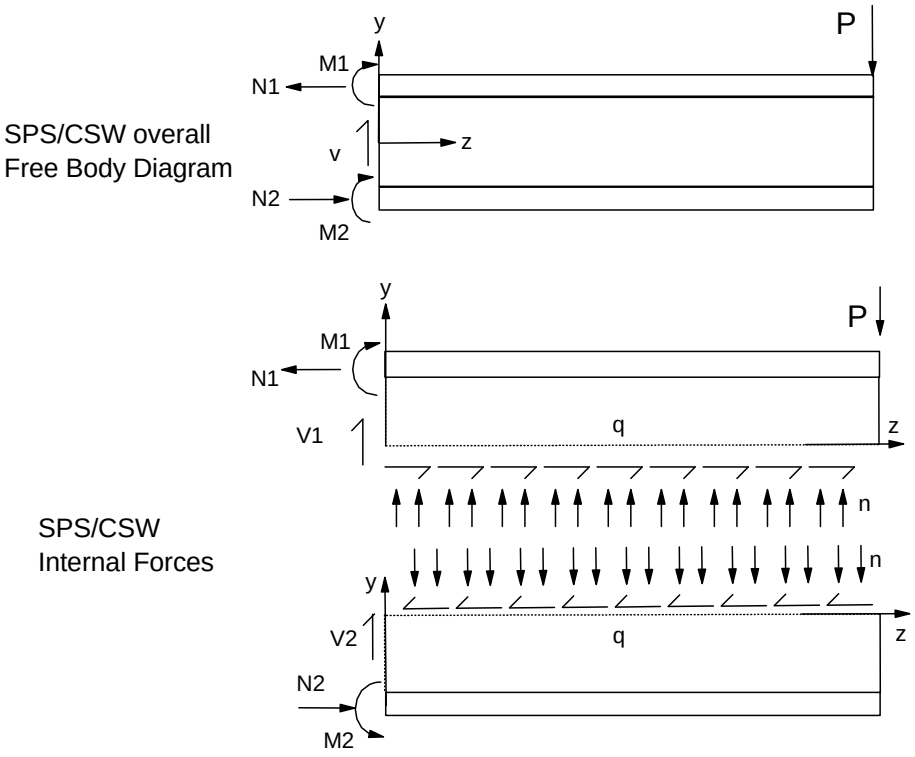

Figure 2.4: SPS forces diagrams.

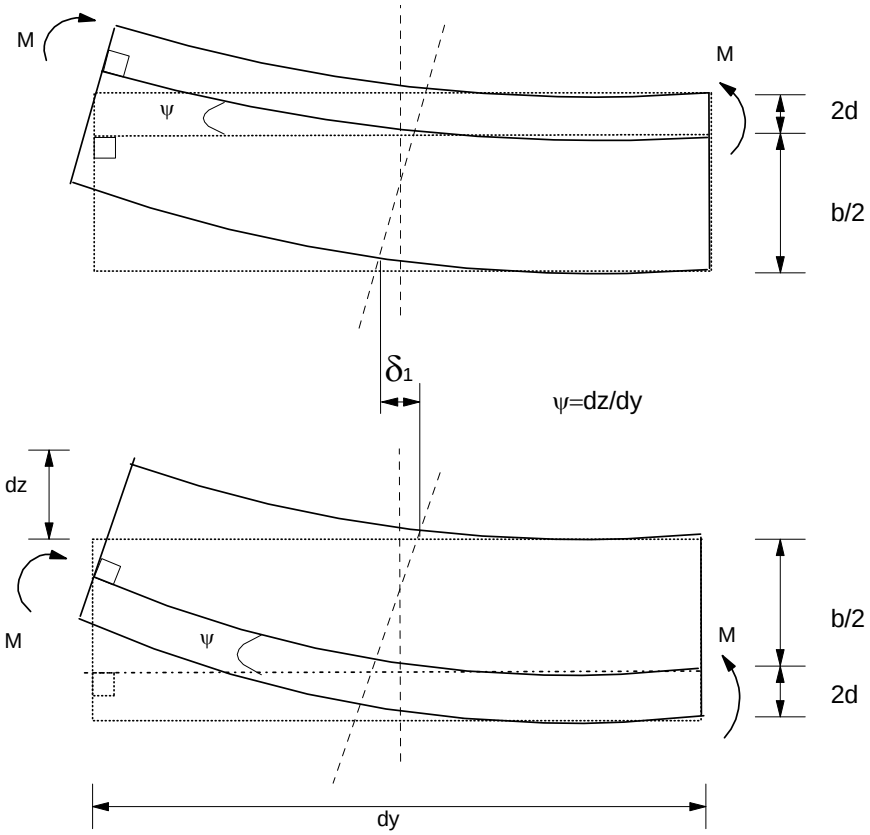

Figure 2.5: Diagram for δ1.

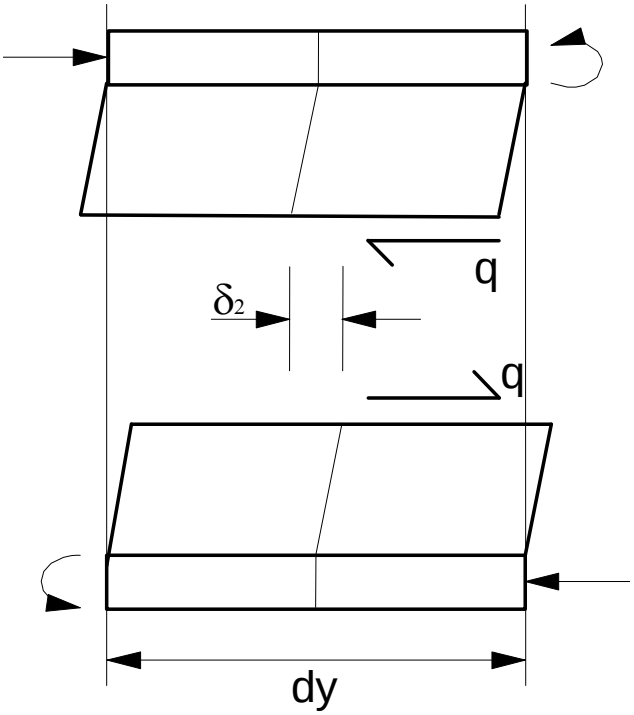

Figure 2.6: Diagram for δ2.

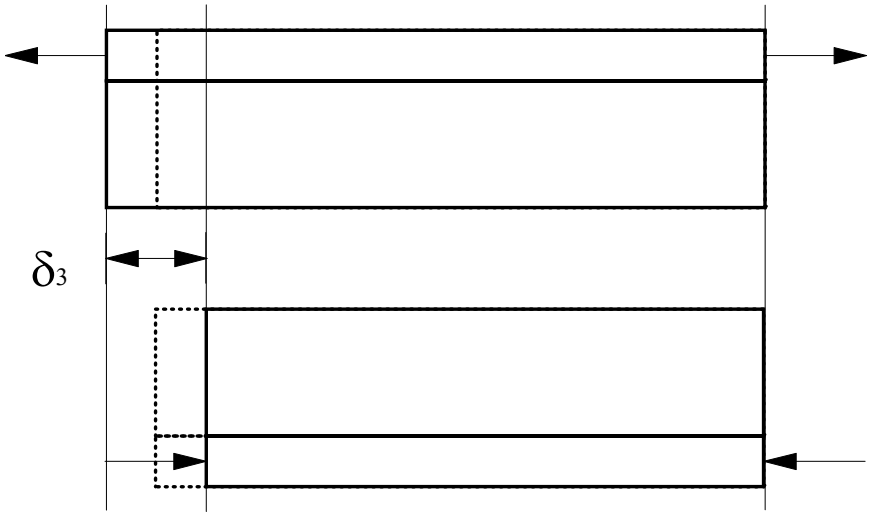

Figure 2.7: Diagram for δ3.

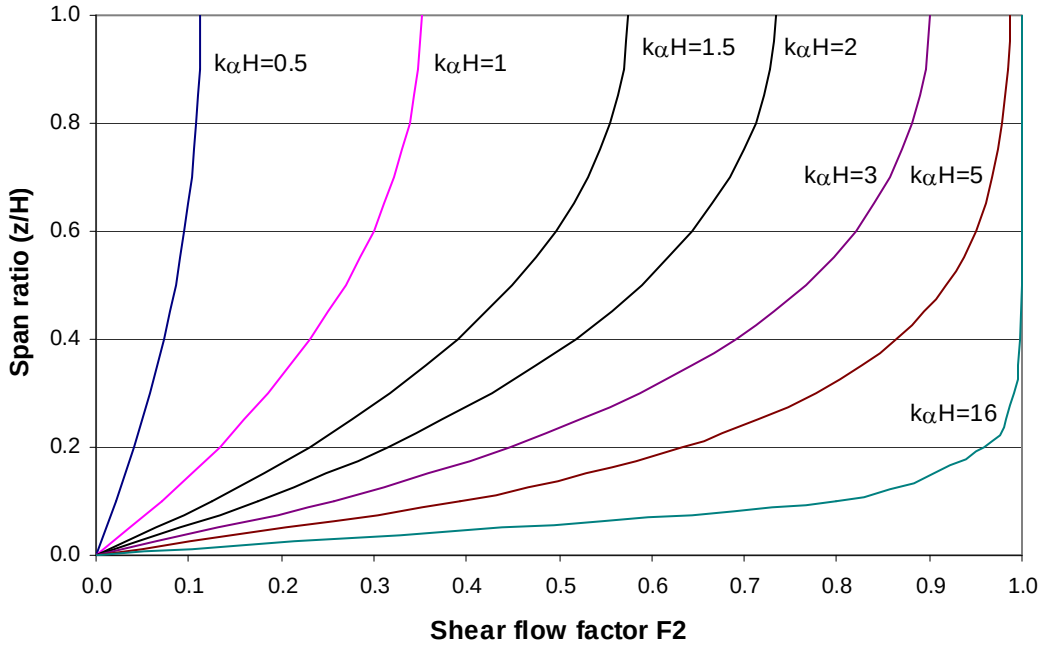

Figure 2.8: Shear flow factor F2 for coupled shear wall.

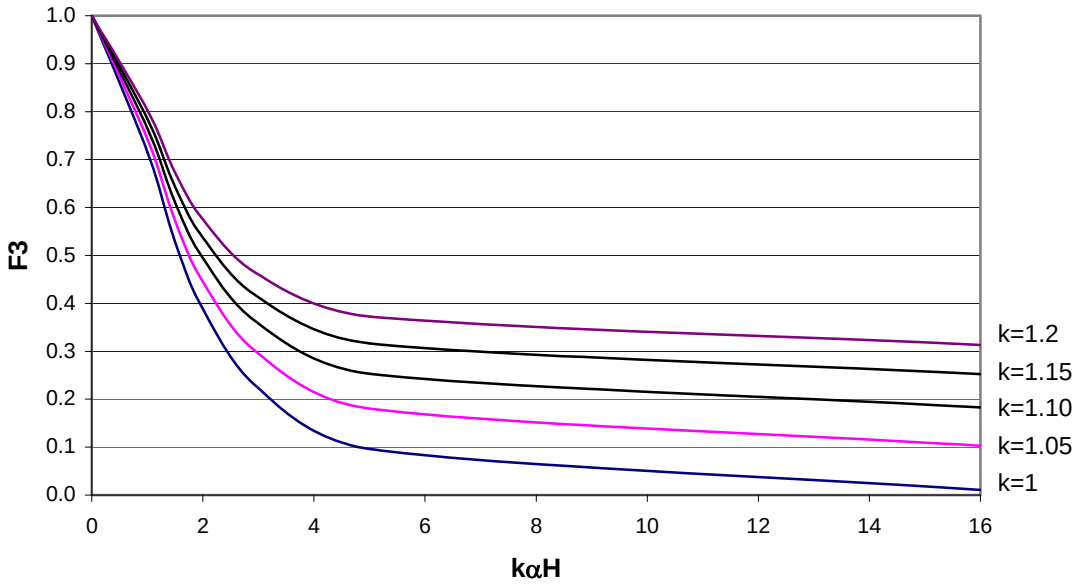

Figure 2.9: Deflection factor F3 for coupled shear wall.

3 EXPERIMENTAL PROGRAM

3.1 Overview

The experimental program consisted of two sets of six sandwich plate system (SPS) specimens. Five specimens from each set were tested under fatigue loading. The remaining specimen from each set was tested under monotonic static load. Ancillary tests provide the material properties of the steel, the elastomer, and the bonding strength of the interface between the two materials.

There are multiple objectives for the current experiment. The main objective is to estimate the fatigue resistance of the bonding interface between the steel layer and the elastomer. Secondarily, stress and strain distribution models are needed so deflection models can be developed. Lastly, alternative fatigue test methods were also desired.

3.2 Test Specimens

The nominal thickness of the three layers designates the SPS. For example, 10-50-10 designates a SPS panel of 10 mm top steel plate, 50 mm elastomer, and 10 mm bottom steel plate.

The two sets of test specimens, labeled A and B, were cut from two separate 10-50-10 panels. Each specimen was labeled “xy”, where “x” identifies the set, and “y” the specimen number. The specimens labeled “A” are the first set and “B” designate the second set. “y” ranged from 1 to 6. A6 and B1 were tested statically and the remaining specimens are tested under cyclic load. Figure 3.1 identifies the dimensions for each specimen and table 3.1 lists the measurements for the dimensions.

Each specimen was initially 2000 mm in length as shown in figure 3.2. Prior to testing, 500 mm was removed from each specimen to provide material for ancillary testing. Each specimen was checked for defects in the bonding interface by chain drag tests and the edges were inspected visually for delaminations. No defects were found.

3.3 Test Setup

3.3.1 Fatigue Test

The setup for the fatigue tests consisted of a single point load at the mid-point of the specimen with simple supports at each end. This arrangement was chosen for its stability and simplicity. The loading points extended the full width of the specimens. Figure 3.3 shows the testing regions and coordinate system for the fatigue tests. Figures 3.4 and 3.5 illustrate the fatigue test setups with overall dimensions. Figures 3.6 and 3.7 show photographs of the test setup.

Safety measures included steel blockings, steel supports, and hydraulic cut-off switch. Steel blockings were positioned at the ends to prevent the reaction rollers from falling. Steel supports, shown in figures 3.4 and 3.5, were to support the specimen in the event of a collapse. A hydraulic cut-off switch that limits mid-span deflection was installed to shut down the hydraulic pressure to prevent further damage to the failed specimens.

3.3.2 Static Test

Figure 3.8 shows the configuration and figure 3.9 shows a photograph of the static test. The specimen was loaded by two point loads and supported by two reactions. The test setup was designed to augment the shearing load that could be applied prior to yielding the steel plates. From the bending moment diagram shown in figure 3.10, the static test setup will permit higher shear loads compare to the fatigue test setup because of a higher moment gradient.

3.4 Instrumentation

Each fatigue test consisted of two test phases: dynamic and interval. The difference between the phases is the type of data collected. In the dynamic phase, the

reference zero is undefined. Therefore, only the maximum and minimum values are recorded. In the interval phase, the reference zero is defined and absolute values are recorded. Absolute values are also recorded in the static tests.

All strain gauges are manufactured by Showa with the model type as N11-FA-5-120-11. All strain gauges had a gauge length of 5 mm, nominal factor of 2.13, and resistance of 120 ohms.

3.4.1 Fatigue Interval Test

Figure 3.4 shows the location and numbering of the Linear Variable Differential Transformers (LVDT's) used in interval tests for set "A" specimens. Figure 3.5 shows the LVDT locations for set "B" specimens. The loading system provided the stroke of the actuator. Figure 3.11 shows a detailed diagram for end LVDT setup set "A" specimens.

Load cells were placed at all contact points during the fatigue experiments. The load cell located at the actuator had a capacity of 667 kN (150 kips). Reaction load cells have capacities of 222 kN (50 kips).

Strain gauges had a numbering scheme shown in figure 3.12 and 3.13 for the specimen sets.

3.4.2 Fatigue Dynamic Data

The dynamic test used essentially the same instrumentation as the interval tests. For dynamic testing, the LVDT's located under the specimen as shown in figure 3.4 and 3.5 were removed to avoid damaging them in the event of a collapse. Also, the rate of change of the load intensities exceeded the response time of the load cells. As a result, the reaction load cells were not active during dynamic testing.

3.4.3 Static Test

Figure 3.14 shows the location of the LVDT's and the Rotary Variable Displacement Transformers (RVDT) for the static tests. Figure 3.8 shows the location for load cell. Figure 3.15 illustrates the locations for the strain gauges in the test region.

3.5 Testing Protocol

3.5.1 Fatigue Test Modes

The fatigue test program consisted of two data modes, interval and dynamic. Fatigue specimens are to fail by tests alternating between the two test modes. Interval mode is a quasi-static test where the loading rate is slower than the dynamic mode. Interval mode tests are conducted on cycles 1, 10, 100, 1000, 10 000, 100 000, 250 000, and at increments of 250 000 thereafter. Dynamic mode tests are conducted after each interval mode test. Table 3.2 lists the order of testing for the fatigue test program.

3.5.1.1 Interval Mode

Fatigue interval data were obtained under manual control of the actuator. Load was applied in 5 kN load steps from 0 kN to maximum load then unload at intervals to 0 kN. Data were collected each load step.

3.5.1.2 Dynamic Mode

Fatigue dynamic data were acquired with the actuator in automated load control. Because fatigue life can be affected by strain rate and frequency of loading (Tsai et al, 1985), the actuator was set to follow a sinusoidal control signal at a frequency of about 3.0 Hz. With loading at 3.0 Hz, the experience for the test specimens are equivalent to a

4.6 m SPS beam resisting traffic load at 50 km/h. Table 3.2 lists the cycles required for each dynamic data set. Data were collected automatically at set time intervals. The data ranges for the active instrumentations were recorded.

Loading was automatically halted upon meeting any one of the three conditions. The three conditions are the completion of the preset number of loading cycles, the stroke exceeding a preset displacement limit, and the load intensity falling outside of a preset tolerance.

Stroke displacement limits were imposed to prevent excessive damage in the event of a specimen failure. The loading tolerance was 1.0 kN. Fatigue test programs were continued until failure of the member or completion of 10,000,000 cycles.

3.5.2 Static Test

A 6000kN capacity universal test machine was used for the static tests. The load was increased monotonically until failure of the specimen. Loading was controlled by an automated stroke signal. Data collected at points of interest supplemented a larger set of data collected automatically at set time intervals.

3.6 Ancillary Tests

Four different types of ancillary test were performed to estimate the material properties and the bonding interface shear capacities of the SPS.

3.6.1 Steel Tension Coupon

Longitudinal and transverse direction steel coupons were taken from the top and bottom steel plates. The elastomer layer was removed from the coupons. Figure 3.16 shows the nominal dimensions of the tension coupons.

Stroke-controlled tension tests collected the data electronically. After initial yielding, static lower yield values were taken after maintaining a constant stroke value for approximately twenty seconds. The coupon ultimate capacity was obtained at failure. Figure 3.17 shows a failed coupon.

Table 3.3 summarizes the results of the steel tension test. Results are grouped by the location and direction of the steel coupon in the specimen. The low coefficient of variance shows the steel properties have a high consistency. The tension capacity of the steel in set “B” specimens are higher than set “A” specimens. There are no significant variations within individual specimen sets.

3.6.2 Interface Shear

Two independent test methods were used to measure the static shear strength of the interface between the steel and the elastomer. The first test method is a block shear test and the other is a torsion test.

3.6.2.1 Block Shear Test

The first test method for the interface shear capacity was the shear block test. Block shear tests method tested Set “A” specimens. A universal test machine applied an overall tension to a test frame, shown in figure 3.18, which attempts to convert an overall tensile force to shear forces acting at the plane of the interface. Figure 3.19 shows the nominal dimensions of the shear block specimens. The tests apply loads to each specimen until the separation of the steel plate from the elastomer. After testing the first interface, the shear block specimen was realigned to test the second interface, provided that the second interface had not been obviously damage from the first test. Figure 3.20 shows a photograph of a test for the second interface.

Problems were observed during testing for some of the shear block tests. Figures 3.21 and 3.22 show free body diagrams for the various components of the block shear tests. Because the test frame applies both shear and moment to the test specimen, the

distribution of normal stress on the interface is non-uniform. The test does not provide a simple shearing failure.

The misalignment of resultant forces within the test specimen caused rotation of the test frame and potentially delaminate the non-testing interface. A modification to the test frame was implemented to mitigate the rotation. Figure 3.23 shows the modifications to the test frame. The screws prevented excessive rotation of the frame. Figure 3.24 shows separations of both interfaces caused by a diagonal tensile force, which is the result of test frame rotation.

Table 3.4 lists the shearing stress results for this method. Histogram in figure 3.25 illustrates the effects of the undetected damage second interface. The results from the second interface are generally lower than the first test in the histogram.

3.6.2.2 Torsion Method

Figure 3.26 shows the nominal dimensions of a torsion test specimen. Figure 3.27 to 3.29 show the shear cylinder during various states of testing. Only pristine set B SPS specimens and select fatigue tested specimens are available to provide material of the torsion tests.

A torsion test is the second method used to test the static interface strength. A manually stroke-controlled torsion machine applied torque to thin-walled cylinder specimens to failure. Because the loading rate affects the accuracy of the results, a load rate independent data set supplements the rate dependent results. “Active” data recorded the torque immediately between loadings. The loading rate influences the “active” data. “Static” data are values obtained after holding the angle of twist constant for a period of 5 minutes. Loading rate does not affect the “static” data. Table 3.5 shows the ultimate shear stress sustained by the interface during static and active loads.

Equation 3.1 (Ugural & Fenster, 1995) is a torsion formula that calculates the maximum stress at the interface for a torsion specimen. Maximum shear stress, τ_{max} is a function of the torque, T, outer radius, r, and polar moment of inertia, J.

$$\tau_{\max} = \frac{Tr}{J} \qquad [3.1]$$

Figure 3.30 shows a graph of shear stress vs. rotation for a typical torsion test. The graph includes both of the “active” and “static” data points. Lines inserted in figure 3.30 show the general trends of the two data sets. Figure 3.31 and 3.32 compiles the “active” and “static” data from all test specimens into graphs. Figure 3.31 shows a tight band for the “active” data in the elastic region, but the data scatter at higher stress levels. Being load rate dependent, “active” data are scattered at higher stress levels. By being load rate independent, “static” results are less scattered. The loading rate of a fatigue test might have an effect on the fatigue life for the SPS, but the effects are beyond the scope of the current experimental program.

Figure 3.33 summarizes the ultimate static shear stresses results. To determine effects of fatigue cyclic loading on the static shear strength, the torsion tests were performed on tested set “A” and tested set “B” specimens. Table 3.5 compares the effects of fatigue loading on interface shear capacities. The table shows that the differences between virgin and tested set B torsion samples are insignificant. The result suggests that fatigue cyclic loading does not necessary reduce the ultimate shear strength or the shear modulus of the torsion samples. Although static interface shear capacities for set virgin “A” specimens are not available, a comparison between tested set “A” and set “B” specimens show that set “A” specimens have lower interface strengths.

3.6.2.3 Interface Shear Comparison

Comparing figure 3.25 and 3.33, the torsion method provides better shear stress results than the shear block method. The torsion method produces results that are more consistent. The stress state of the specimen is well-defined.

The torsion test may be a viable quality control tool for SPS interface strength during SPS production because of its relatively small test specimens, exact failure locations, well-defined stress state, and consistent results.

3.6.3 Elastomer Shear Modulus

Two methods can estimate the shear modulus, G, of the elastomer. The methods are tension and torsion.

3.6.3.1 Elastomer Tension Test

Figure 3.34 shows a photograph of a coupon tension test. Table 3.6 lists the tension coupon test results for the elastomer. The results provide *E* and Poisson's ratio, ν, of the elastomer. Equation 3.2 (Beer & Johnston, 1992) calculates *G* of the elastomer from *E* and ν.

$$G = \frac{E}{2(1+\upsilon)} \qquad [3.2]$$

3.6.3.2 Torsion Method

Torsion ancillary test results can estimate the shear modulus of the elastomer by using equation 3.3 (Ugural and Fenster, 1995) for small twist angles. The measured length of the elastomer layer, *l*, and the rotation, φ, can affect the quality of the results. Because the testing equipments have large increments between angle measurements, the results might have exceeded the small angle of twist requirement. Sensitive data-recording equipments will improve the accuracy of the results from this method. Table 3.7 lists the results from this method.

$$G = \frac{TL}{J\phi} \qquad [3.3]$$

3.6.3.3 Shear Modulus Comparison

The tension tests show consistent shear modulus results compared with the torsions tests. The tension tests reported a higher shear modulus (186 MPa) than the torsions tests (average of 142 MPa). For elastomer shear modulus measurements, the tension test is a better test method.

3.6.4 Surface Roughness

A tracer type machine that records the profile of a surface was used to determine the surface roughness of the steel plates at the polymer interface. The results reported were “Centerline Averages” in units of micro-inches.

Centerline average for surface roughness is defined as a line parallel to the direction of the profile throughout the roughness-width cutoff length such that the sums of the areas contained between it and those parts of the profile that lie on either side of it are equal (ASA, 1955). Equation 3.4 (ASA, 1955) defines the surface roughness value, *Y*, from deviations, *y*, in the sampled distance, *l*.

$$Y = \frac{1}{l}\int_{x=0}^{x=l}|y|dx \qquad [3.4]$$

Steel plates from tested shear blocks and failed test specimen are the subjects for the roughness test. Samples are chosen to identify any correlations between the surface roughness and fatigue properties.

Each sample was tested in two perpendicular directions. Table 3.8 shows the test results. Figure 3.35 illustrates a substantial difference in surface roughness between the two sets of specimens.

3.7 Plastic Capacity

Table 3.9 lists the plastic capacities for the specimens. Figure 3.36 shows a sample diagram of applied moment vs. stroke for a specimen tested after 10 million

cycles. The idealized loading diagrams overestimate the applied moment by 4.7%. With idealized loading diagrams, the calculated applied moment exceeds the calculated plastic moment by 5.5%. Adjustments to realistic conditions reduce the difference between the recorded applied moments and calculated plastic moment to 0.8%. The error magnitude is acceptable and the plastic moment calculated is satisfactory.

Table 3.1: Specimen dimension (mm) refer to Figure 3.1.

	A1	A2	A3	A4	A5	A6
PN	198.0	199.1	201.8	202.2	200.8	201.9
PM	199.4	200.6	200.8	200.6	200.3	200.1
PS	201.4	201.3	199.4	199.9	199.9	199.3
EN	67.4	67.3	69.0	68.0	67.5	69.0
EM	67.8	68.4	68.5	68.5	68.4	68.6
ES	68.3	68.0	68.0	69.2	68.7	68.9
	B1	**B2**	**B3**	**B4**	**B5**	**B6**
PN	149	200	197	200	199	200
PM	150	200	198	200	198	200
PS	151	200	200	200	200	204
EN	69.0	62	62	61	68	64
EM	67.0	62	63	64	68	67
ES	67.0	62	62	64	68	68

Table 3.2: Cycles and test mode for fatigue test program.

Cycle Number	Test Mode
1	Interval
2 to 9	Dynamic
10	Interval
11 to 99	Dynamic
100	Interval
101 to 999	Dynamic
1000	Interval
1001 to 9999	Dynamic
10,000	Interval

Cycle Number	Test Mode
10,001 to 99,999	Dynamic
100,000	Interval
100,001 to 249,999	Dynamic
250,000	Interval
250,001 to 499,999	Dynamic
500,000	Interval
500,001 to 749,999	Dynamic
Pattern repeats every 250,000 cycles	Interval
	Dynamic

Table 3.3: Steel tension coupon test result summary.

Set "A"	Overall	Top	Bottom	Transverse	Longitudinal
Average (MPa)	360	359	361	358	361
StDev (MPa)	8.4	8.6	8.1	9.9	7.3
CoV	2.3%	2.4%	2.2%	2.8%	2.0%
Ultimate (MPa)	561	561	562	562	561
StDev (MPa)	6.4	6.7	6.1	6.6	6.3
CoV	1.1%	1.2%	1.1%	1.2%	1.1%
E (MPa)	200269	199240	201229	201386	199681

Set "B"	Overall	Top	Bottom	Transverse	Longitudinal
Yield (MPa)	463	460	466	465	461
StDev (MPa)	10.0	7.0	12.1	6.1	12.9
CoV	2.2%	1.5%	2.6%	1.3%	2.8%
Ultimate (MPa)	533	532	534	536	531
StDev (MPa)	6.2	4.9	7.4	5.6	5.7
CoV	1.2%	0.9%	1.4%	1.0%	1.1%
E (MPa)	202143	200407	203880	209557	194730

Table 3.4: Shear block test results.

	V1 (MPa)		V2 (MPa)		V3 (MPa)		V4 (MPa)	
	Top	**Bottom**	**Top**	**Bottom**	**Top**	**Bottom**	**Top**	**Bottom**
A1	NA	9.60	NA	10.24	NA	8.53	NA	7.16
A2	NA	9.97	NA	6.16	NA	9.80	NA	6.88
A3	6.99	6.36	5.41	7.06	6.80	5.02	6.15	5.17
A4	5.22	6.06	7.39	6.55	6.19	6.90	6.69	4.62
A5	5.77	7.13	5.52	7.51	6.36	NA	4.25	6.56
A6	NA	NA	9.15	5.24	8.04	9.59	7.16	8.23

Table 3.5: Torsion test results.

Ultimate Interface Stress (Static MPa)									
	Prior to fatigue						After fatigue		
	B1	B2	B3	B4	B5	B6	B3	A3	A4
Sample 1	12.1	12.9	NA	13.6	11.9	13.3	13.3	10.2	10.9
Sample 2	NA	15.0	NA	12.1	13.1	4.0	13.6	11.0	NA
Sample 3	11.8	12.6	13.9	11.5	11.2	13.0	13.3	9.2	NA
Sample 4	11.8	11.7	13.1	11.4	12.8	11.7			
Sample 5	NA	11.3	11.1	12.3	12.4	NA			
Sample 6	NA	NA	11.0	12.6	10.9	NA			
Average	11.9	12.7	12.3	12.2	12.1	10.5	13.4	10.1	10.9
St Dev	0.2	1.4	1.4	0.8	0.9	4.4	0.2	0.9	0.0
CoV	1.5%	11.4%	11.7%	6.6%	7.4%	42.1%	1.2%	8.7%	0.0%

Ultimate Interface Stress (Active MPa)									
	Prior to fatigue						After fatigue		
	B1	B2	B3	B4	B5	B6	B3	A3	A4
Sample 1	23.8	22.8	24.9	22.1	22.7	27.3	24.1	17.9	15.5
Sample 2	NA	27.0	27.8	22.3	25.3	6.7	24.3	18.8	18.0
Sample 3	22.9	25.4	25.2	22.8	22.9	25.9	23.8	17.3	15.3
Sample 4	24.5	22.4	26.4	23.4	21.7	22.3			
Sample 5	NA	22.6	22.4	24.5	25.2	NA			
Sample 6	NA	NA	22.0	24.1	21.7	NA			
Average	23.7	24.0	24.8	23.2	23.2	20.5	24.1	18.0	16.3
St Dev	0.8	2.1	2.2	1.0	1.6	9.5	0.3	0.8	1.5
CoV	3.4%	8.5%	9.0%	4.1%	7.0%	46.0%	1.2%	4.2%	9.3%

Table 3.6: Elastomer tension test results.

	E (Slope, MPa)	Poisson ratio	G (MPa)	Ultimate Stress (Static, MPa)	Ultimate Stress (dynamic, MPa)
Overall					
Average	501.6	0.355	185.1	18.3	21.2
St Dev	10.0	0.0	3.5	2.1	2.6
CoV	2.0%	5.8%	1.9%	11.7%	12.1%
Set A					
Average	510.0	0.367	186.6	16.9	19.3
St Dev	5.3	0.0	4.0	1.3	1.6
CoV	1.0%	5.8%	2.1%	7.5%	8.4%
Set B					
Average	493.3	0.344	183.6	20.5	23.2
St Dev	5.1	0.0	2.5	0.8	1.7
CoV	1.0%	3.7%	1.4%	3.7%	7.5%

Table 3.7: Shear modulus results from torsion tests.

Shear Modulus (MPa)									
	Prior to fatigue tests						After fatigue test		
	B1	B2	B3	B4	B5	B6	B3	A3	A4
Sample 1	110.2	150.8	225.0	169.5	142.4	190.9	117.3	107.8	141.1
Sample 2	NA	200.7	178.9	141.9	171.2	85.7	214.7	135.9	182.9
Sample 3	112.1	182.3	154.6	112.9	112.2	70.5	208.6	164.2	103.1
Sample 4	151.6	128.2	117.7	155.7	179.0	148.3			
Sample 5	NA	117.6	141.2	166.4	131.7	NA			
Sample 6	NA	NA	134.5	138.3	138.1	NA			
Average	124.6	155.9	158.7	147.4	145.8	123.8	180.2	136.0	142.4
ST Dev	23.3	35.2	38.4	21.1	25.1	56.0	54.5	28.2	39.9
CoV	18.7%	22.6%	24.2%	14.3%	17.2%	45.2%	30.3%	20.7%	28.1%

Table 3.8: Average surface roughness test results.

Specimen	Roughness (μm)
A4V4B	5.42
A5V2B	5.72
A5V4T	4.95
A6V3B	5.28
A6V3T	5.18
B3	7.85

Table 3.9: Calculated plastic moment.

Specimen	A1	A2	A3	A4	A5	A6
Steel MP (kNm)	41.5	41.8	42.3	42.3	42.0	42.4
Elastomer MP (kNm)	1.9	1.9	2.0	2.0	2.0	2.0
Total MP (kNm)	43.5	43.7	44.3	44.3	43.9	44.4
Specimen	B1	B2	B3	B4	B5	B6
Steel MP(kNm)	40.3	47.8	47.9	48.3	53.2	52.2
Elastomer MP (kNm)	1.8	1.8	1.8	1.9	2.4	2.2
Total MP (kNm)	42.1	49.6	49.7	50.2	55.6	54.4

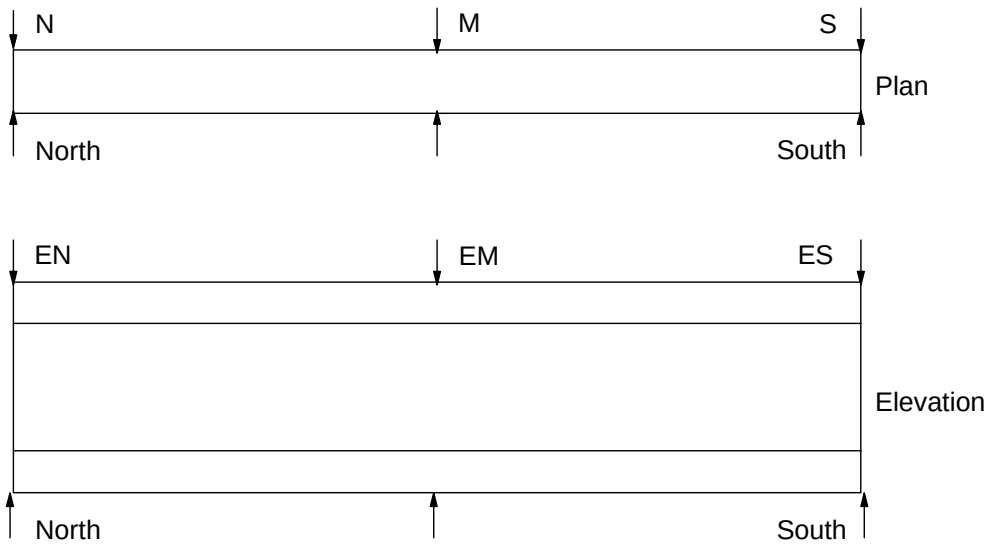

Figure 3.1: Description for specimen dimensions.

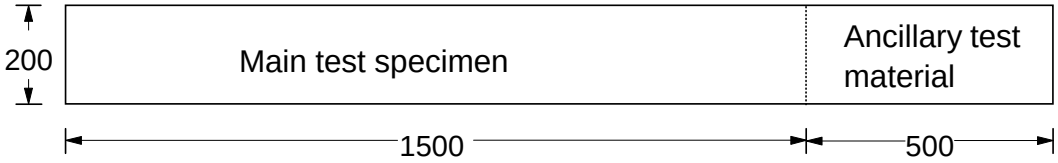

Figure 3.2: Original specimen dimensions.

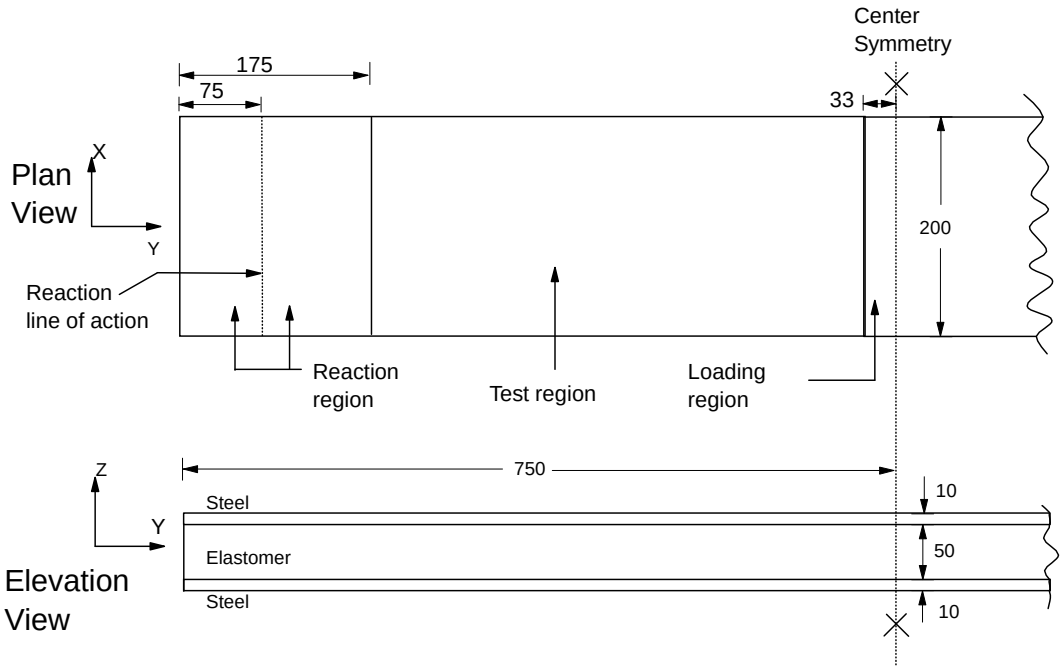

Figure 3.3: Nominal specimen dimension and coordinate system.

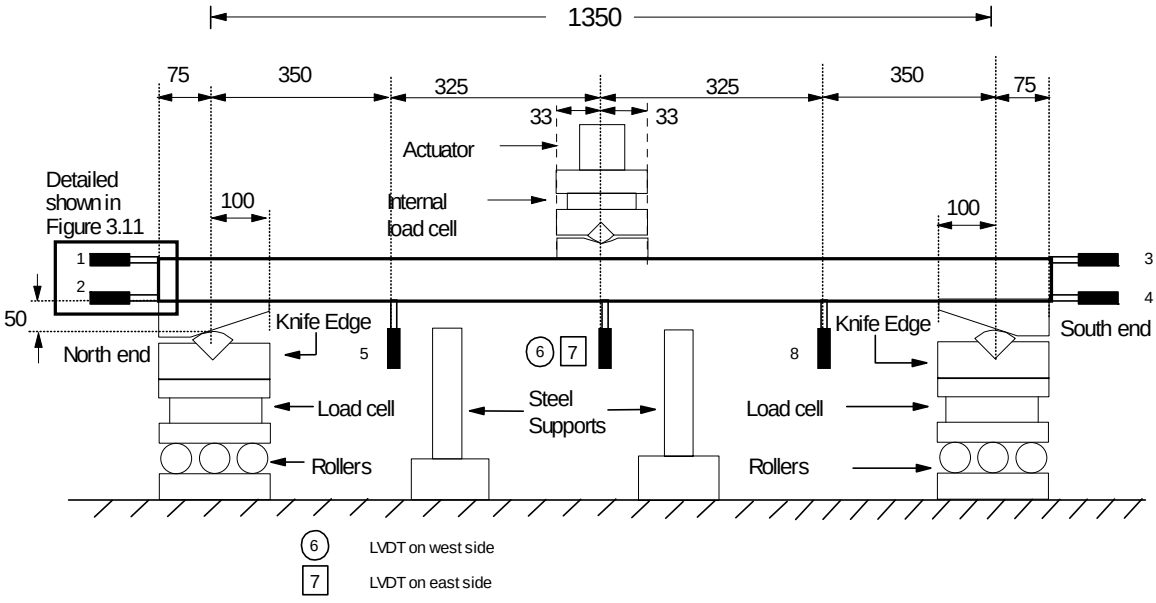

Figure 3.4: Fatigue test setup for A1 to A5 and LVDT locations.

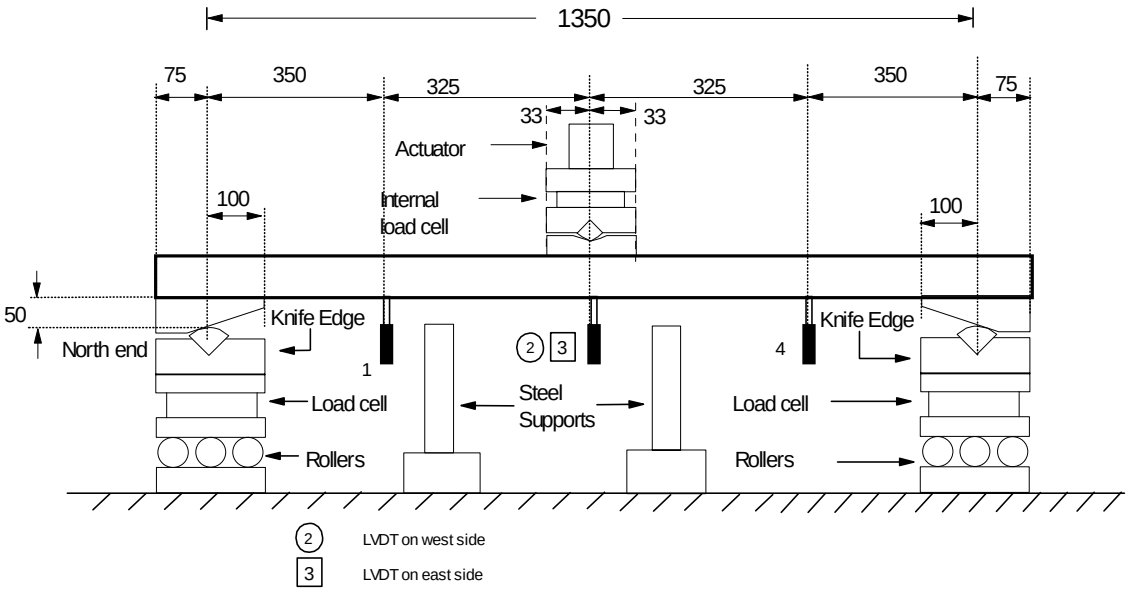

Figure 3.5: Fatigue test setup for B2 to B6 and LVDT locations.

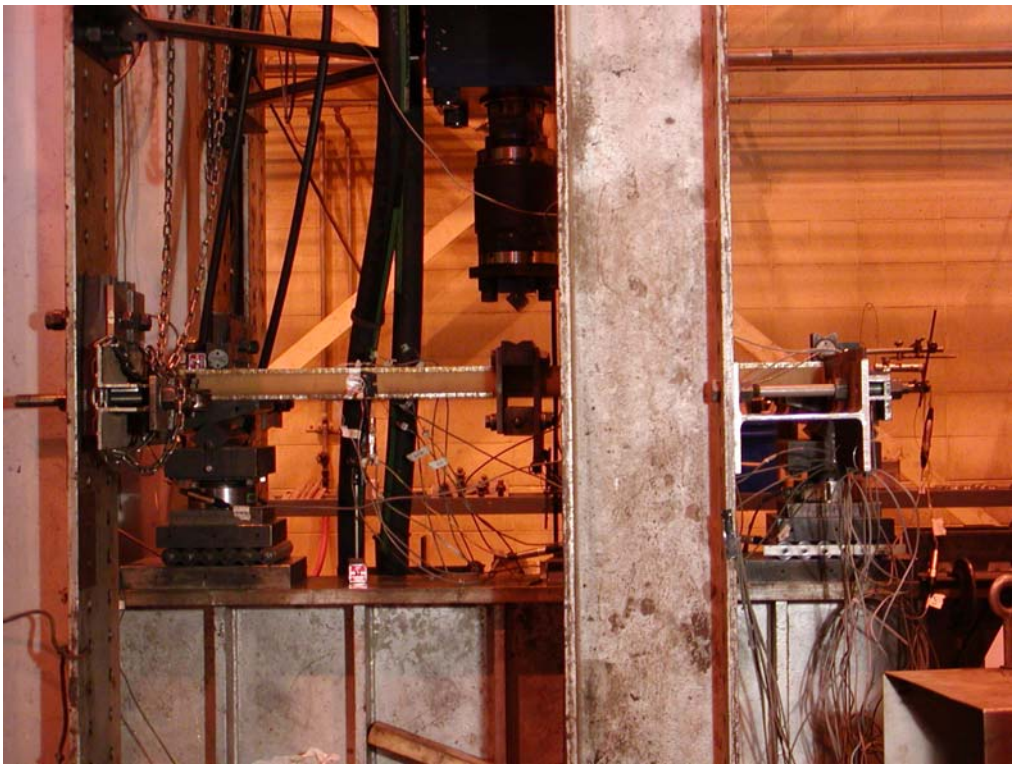

Figure 3.6: Fatigue test setup side view.

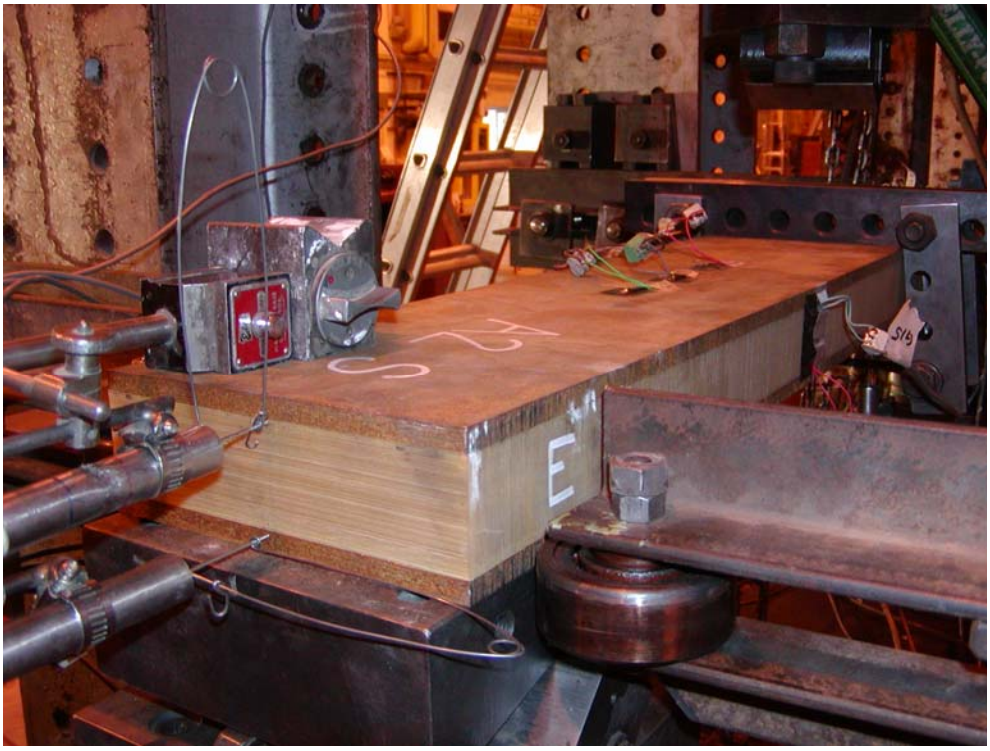

Figure 3.7: Fatigue test setup end view (A2 shown).

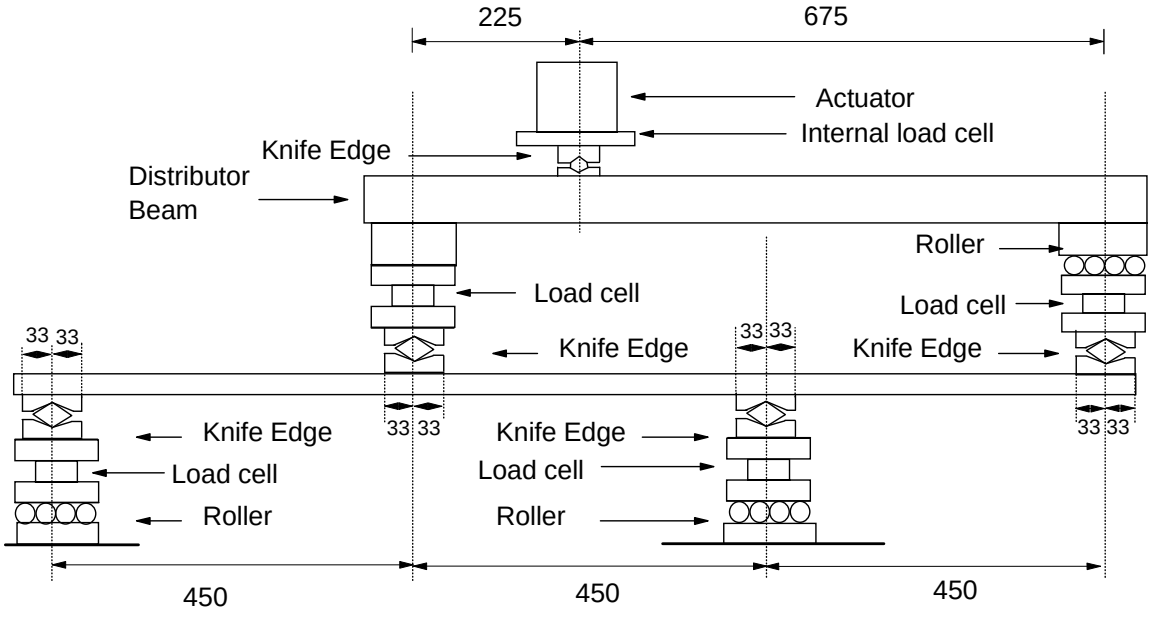

Figure 3.8: Static test setup.

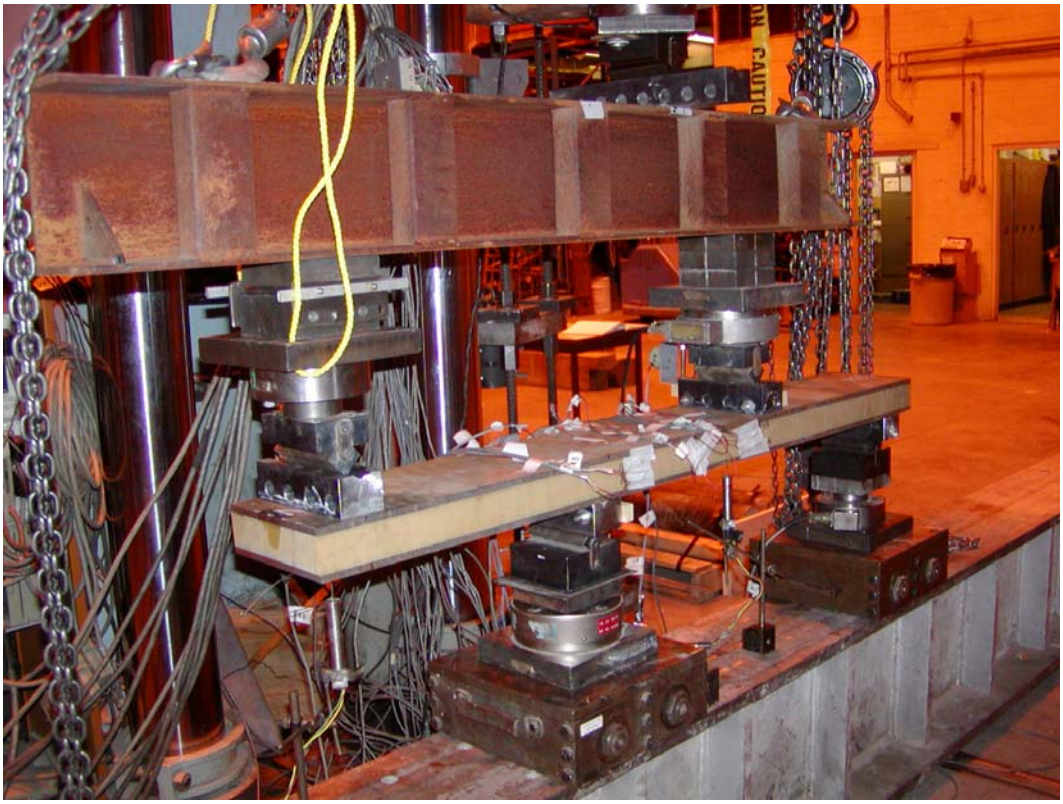

Figure 3.9: Photograph of static test setup.

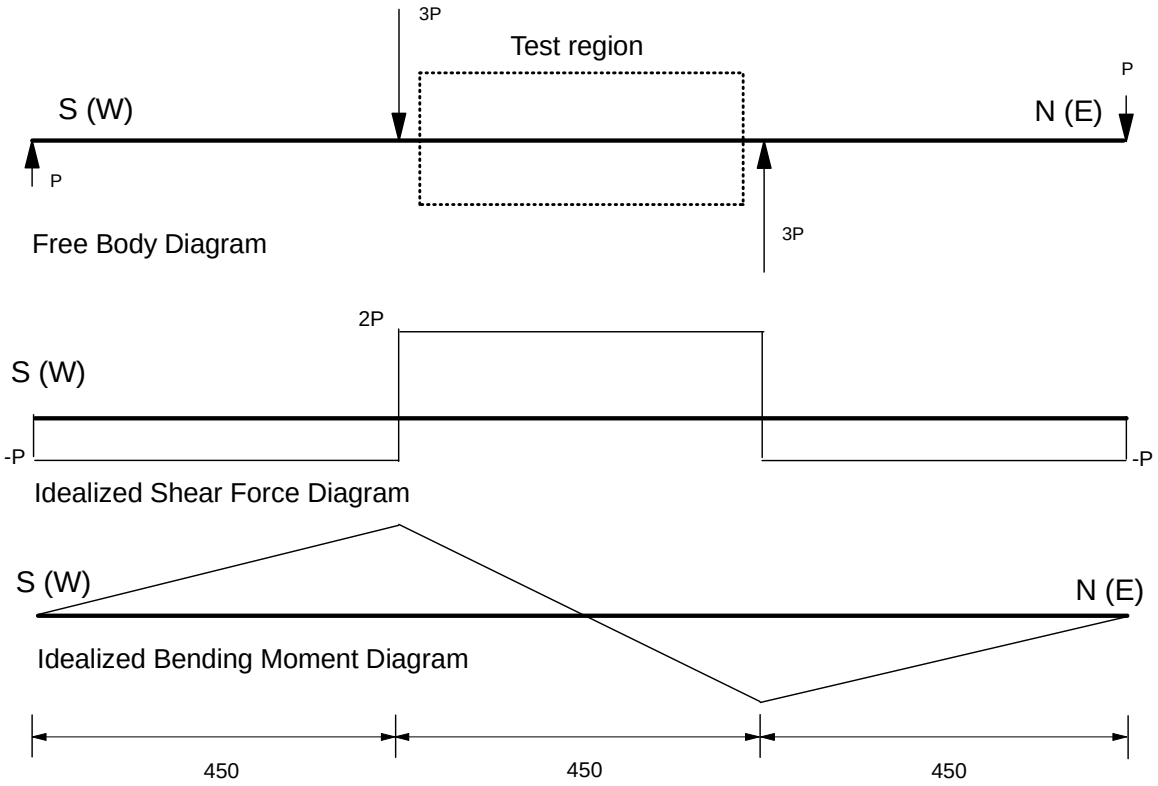

Figure 3.10: Load diagrams for static tests.

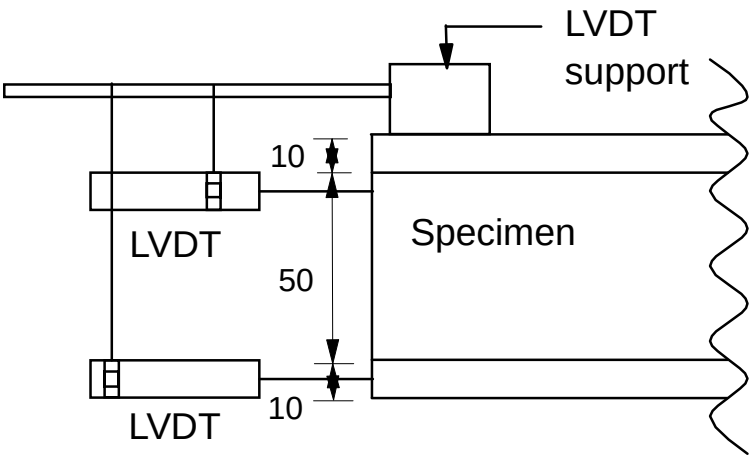

Figure 3.11: Detailed diagram of LVDT locations (Applicable to set A specimens).

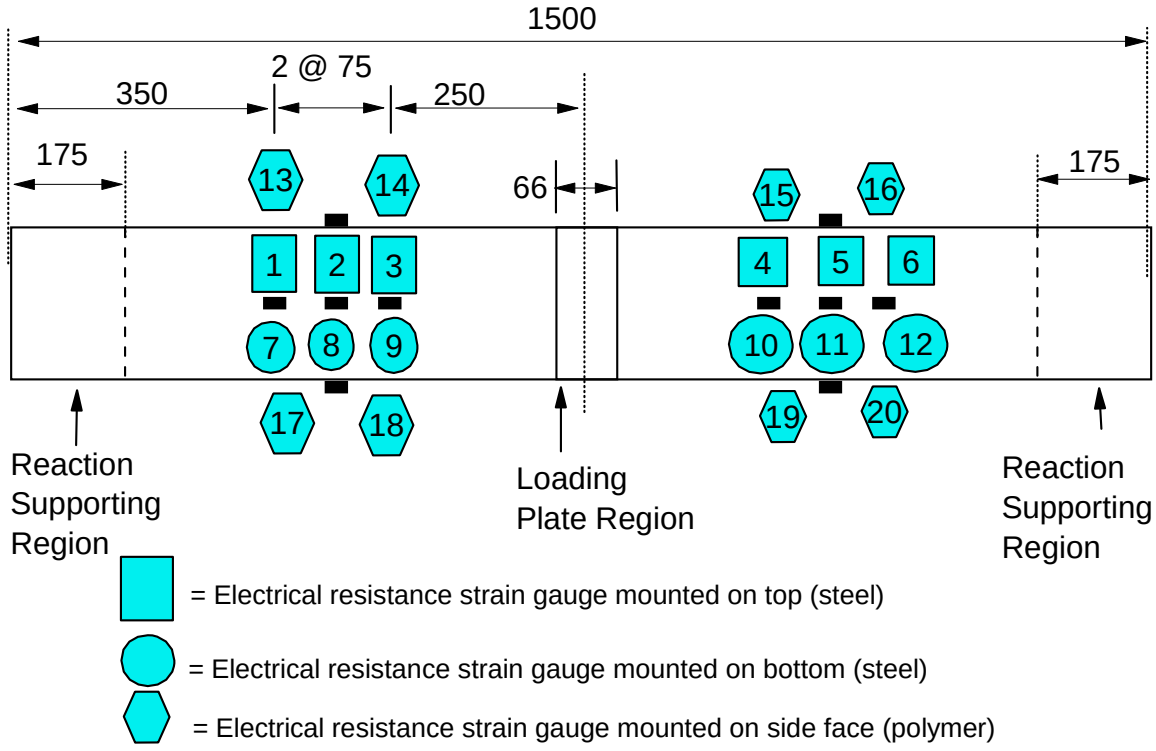

Figure 3.12: Strain gauge locations for set A fatigue specimens.

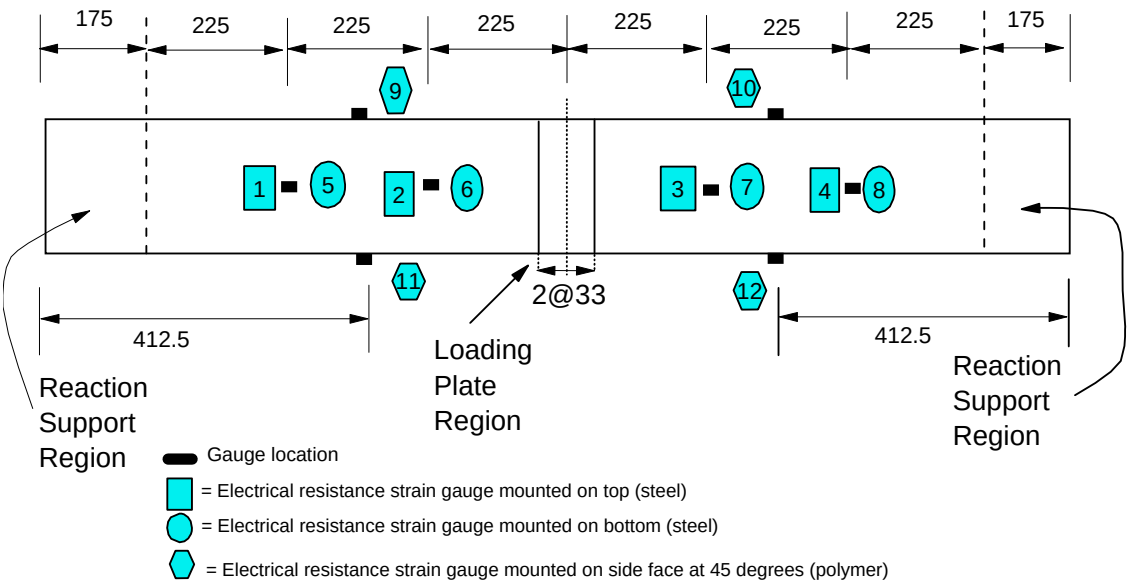

Figure 3.13: Strain gauge locations for set B fatigue specimens.

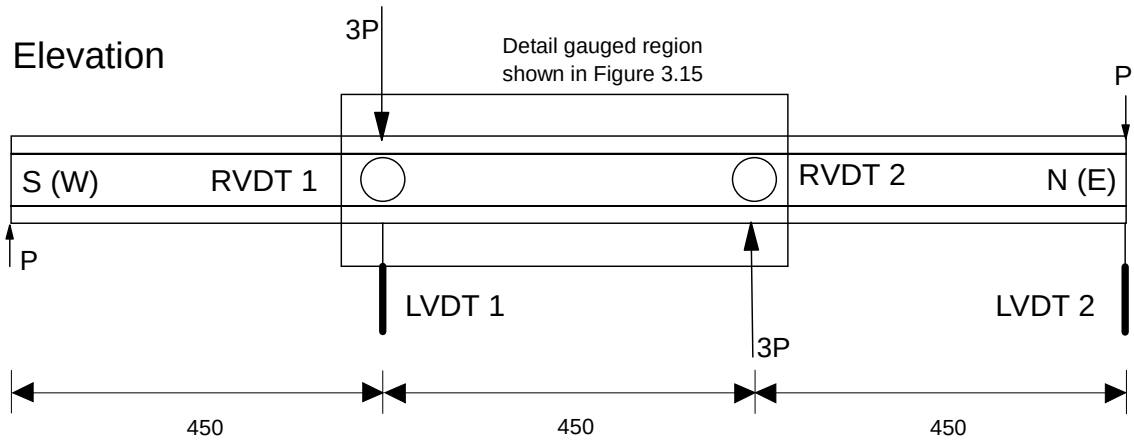

Figure 3.14: LVDT and RVDT locations for static tests.

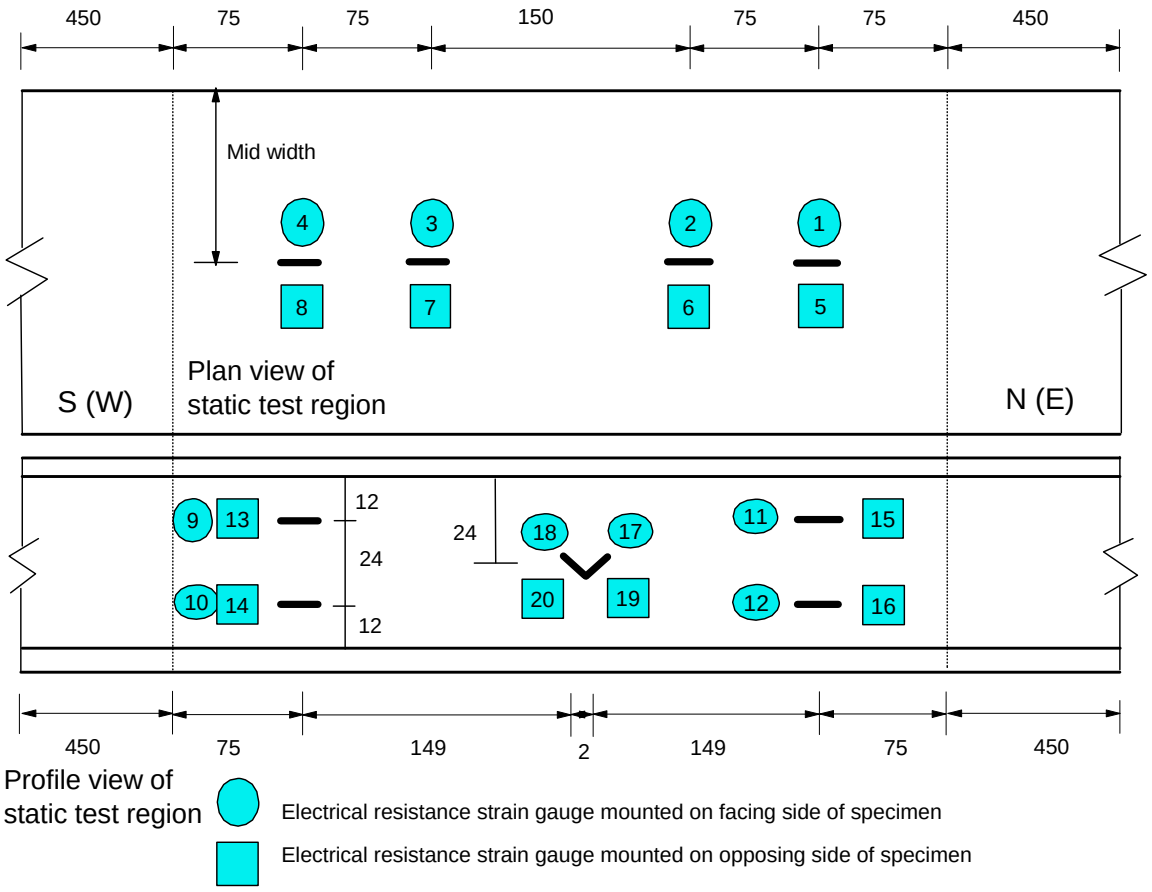

Figure 3.15: Strain gauge locations for static test region.

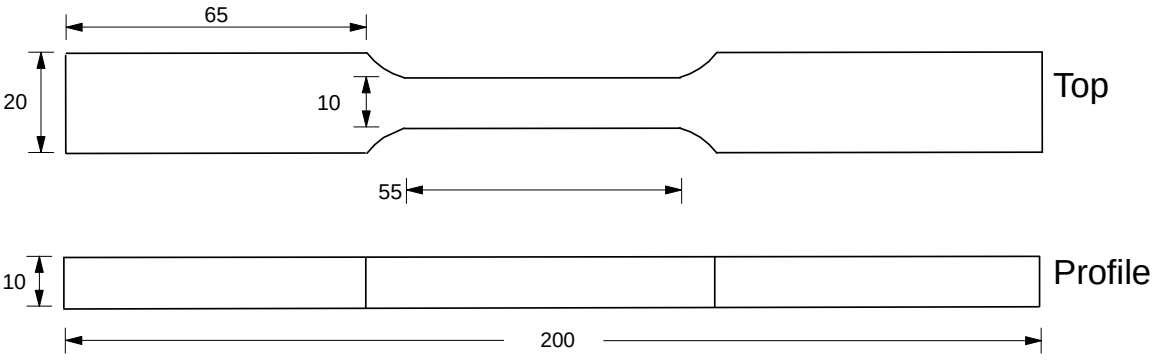

Figure 3.16: Steel tension coupon specimen dimensions.

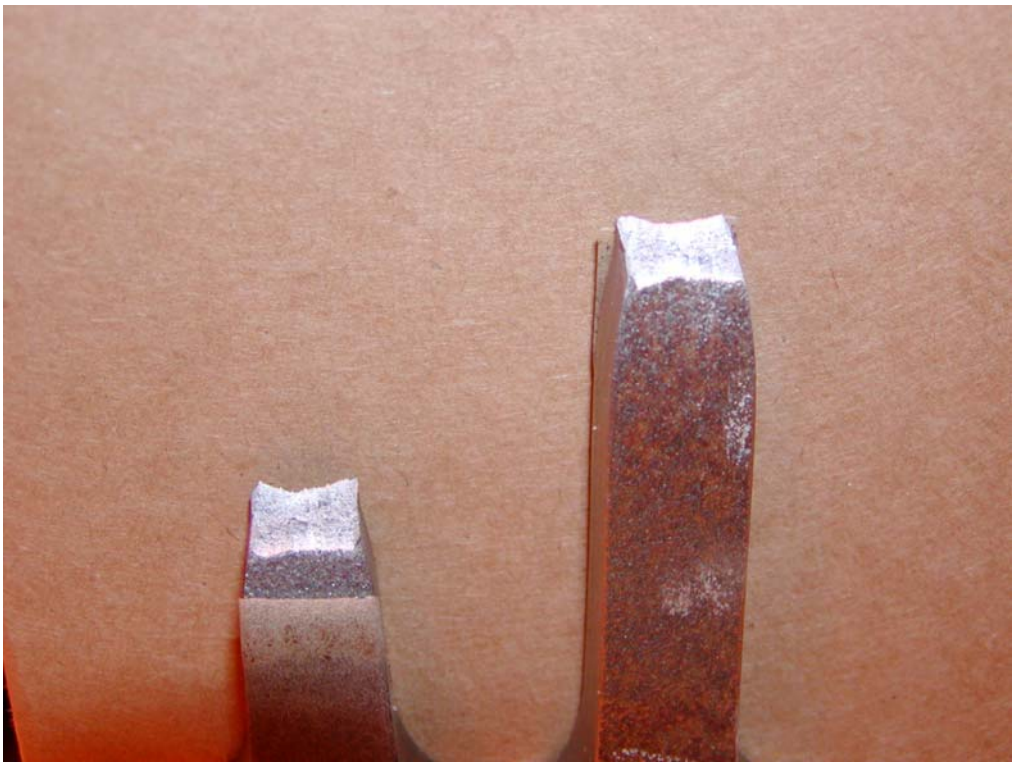

Figure 3.17: Tested steel tension coupon.

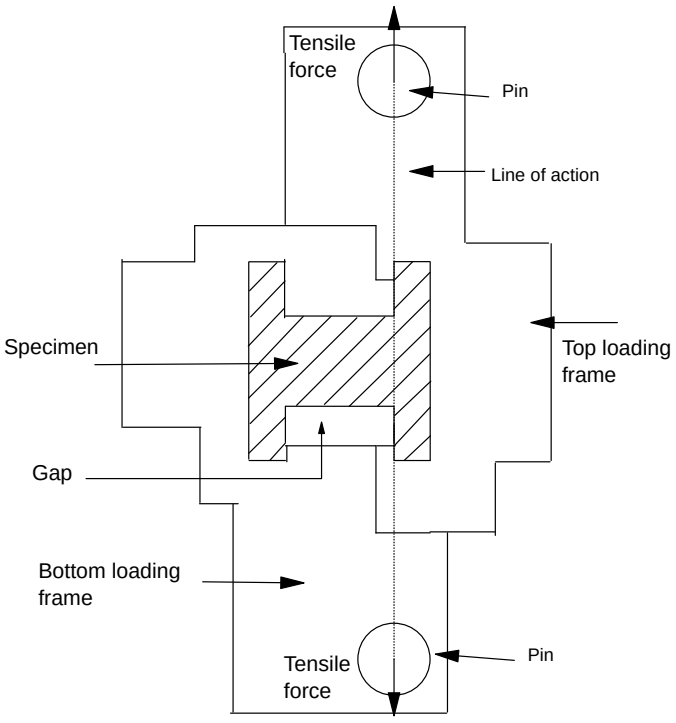

Figure 3.18: Shear block method loading frame.

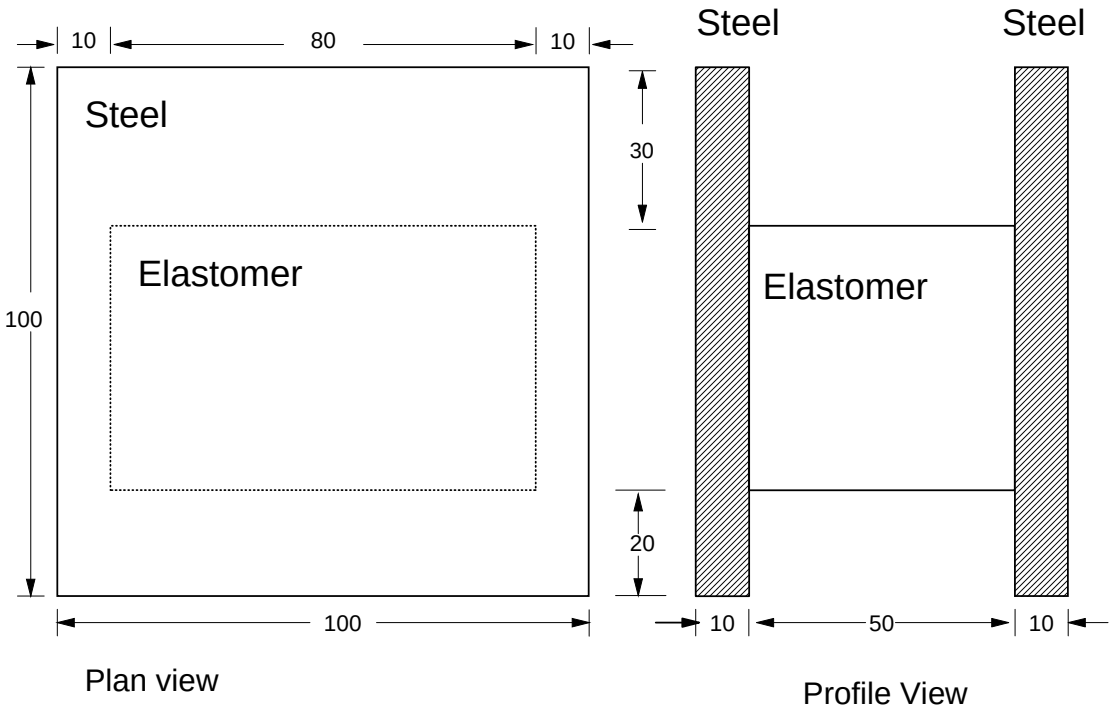

Figure 3.19: Nominal shear block specimen dimensions.

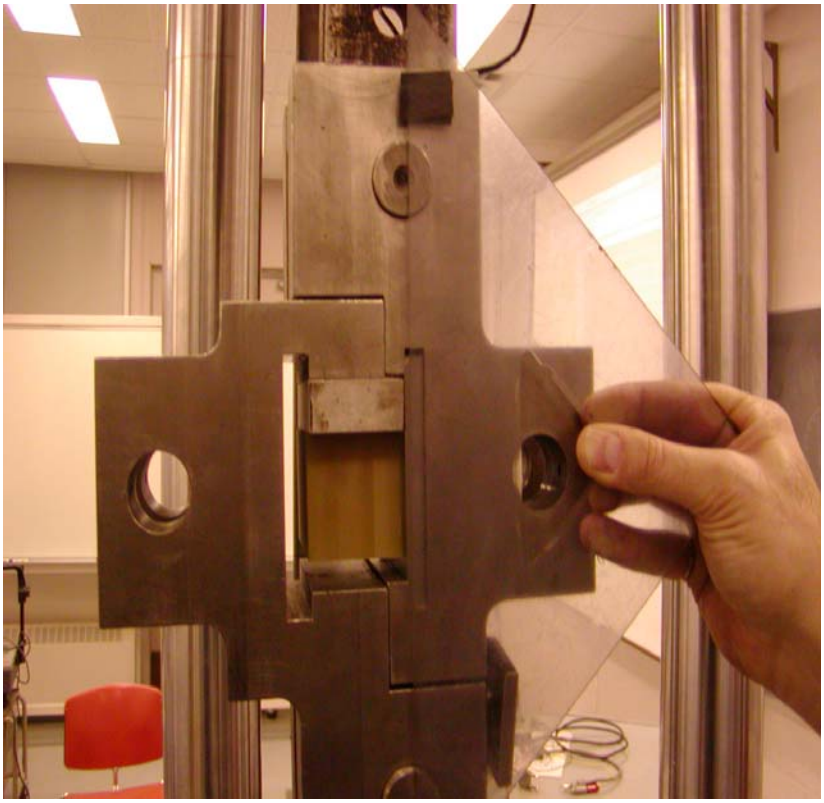

Figure 3.20: Elastomer shear test setup. (Testing of second interface)

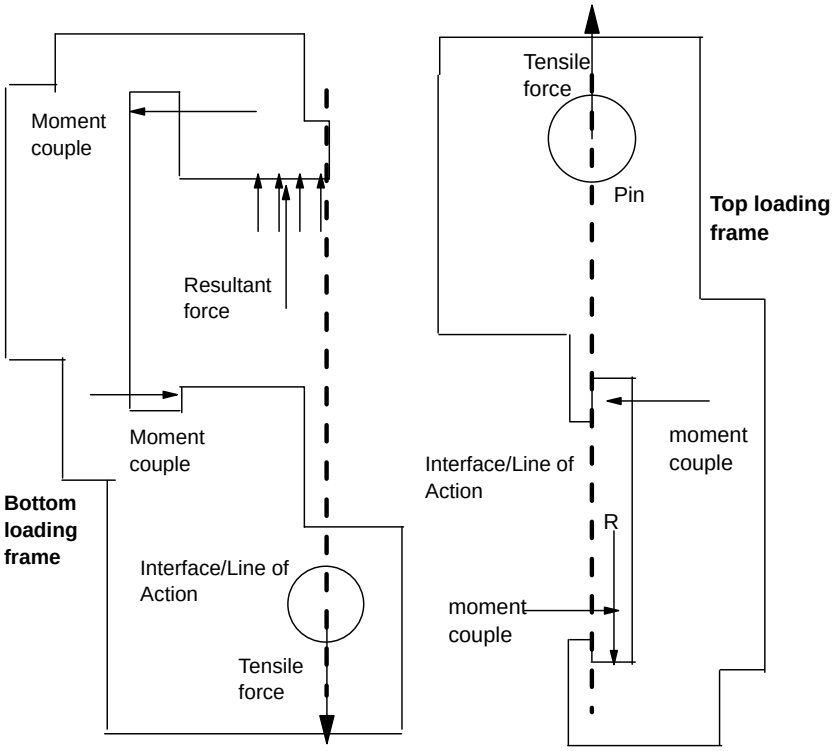

Figure 3.21: Possible forces acting upon the test frame.

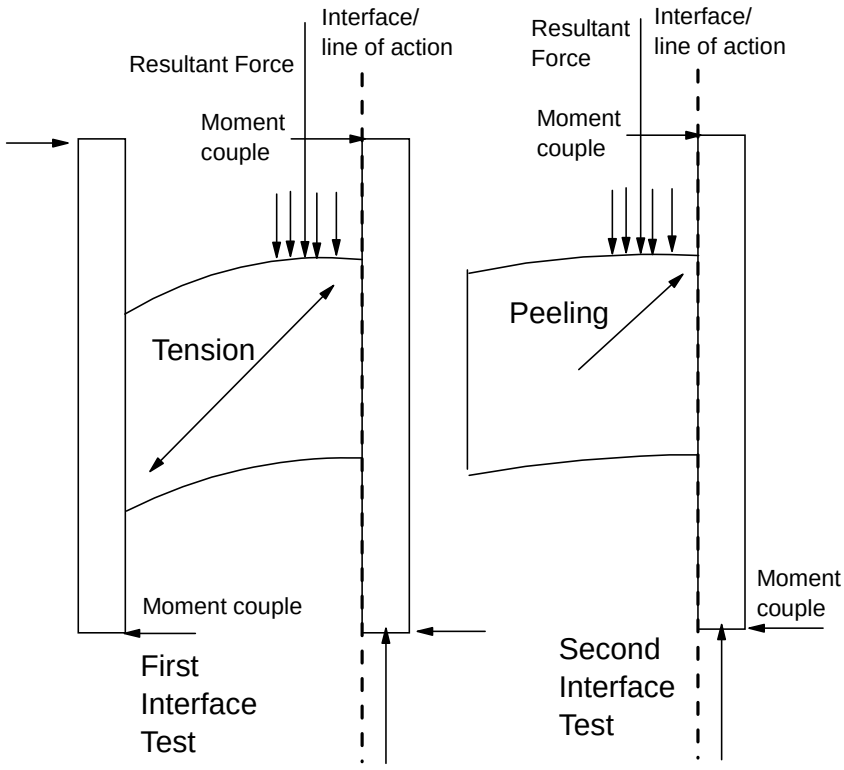

Figure 3.22: Possible forces acting on the shear block specimen.

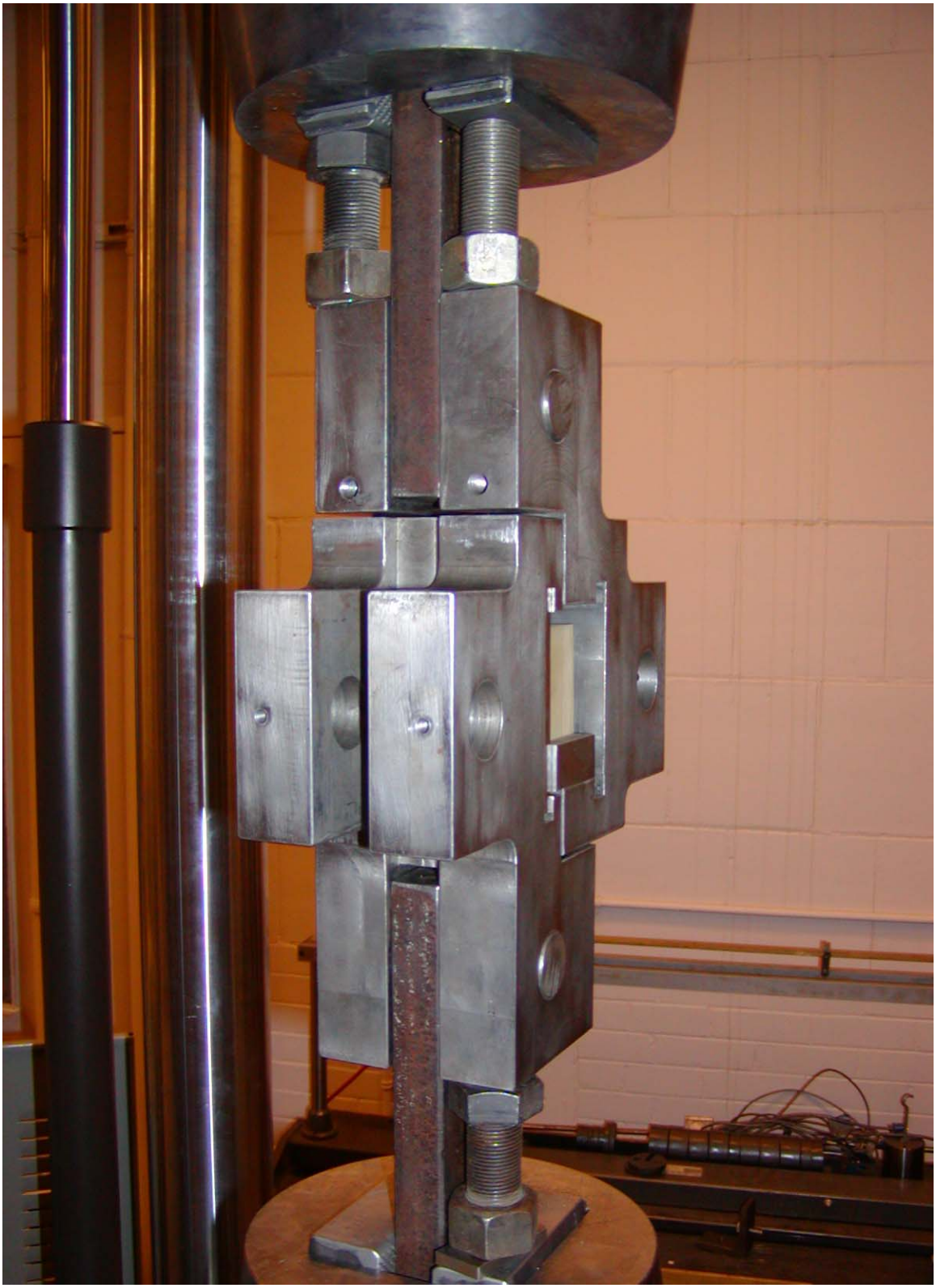

Figure 3.23: Screw studs implemented to resist excessive test frame rotation.

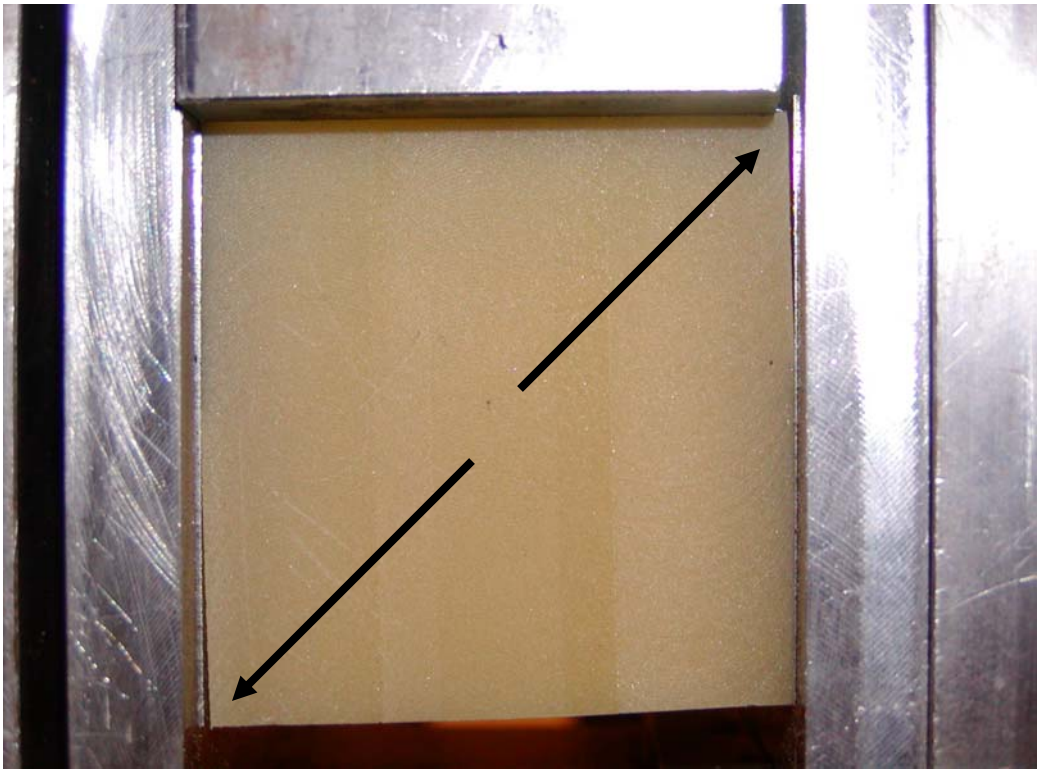

Figure 3.24: Tensile force acted diagonally.

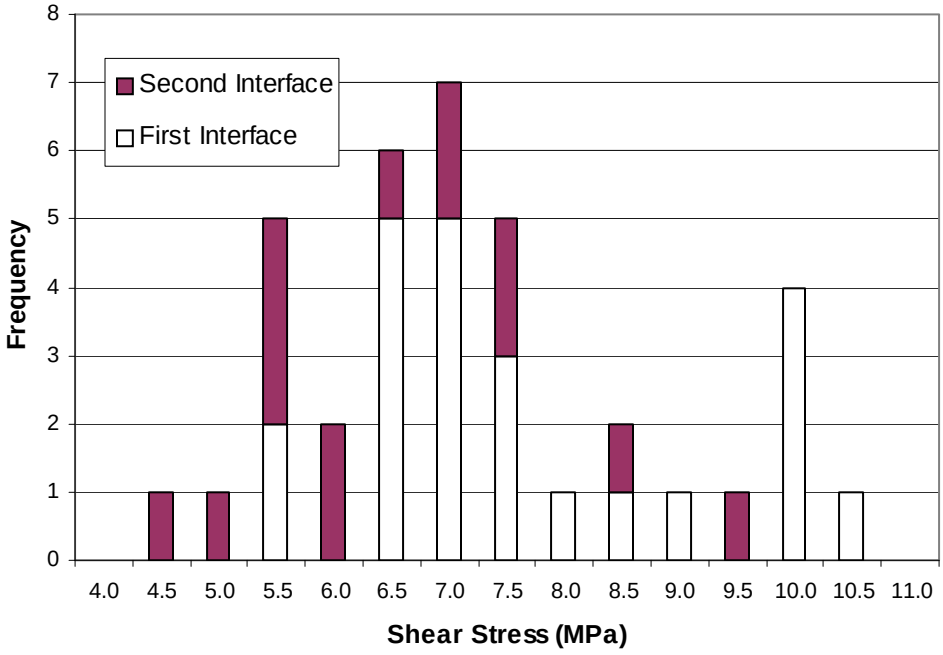

Figure 3.25: Ancillary shear block test result histogram.

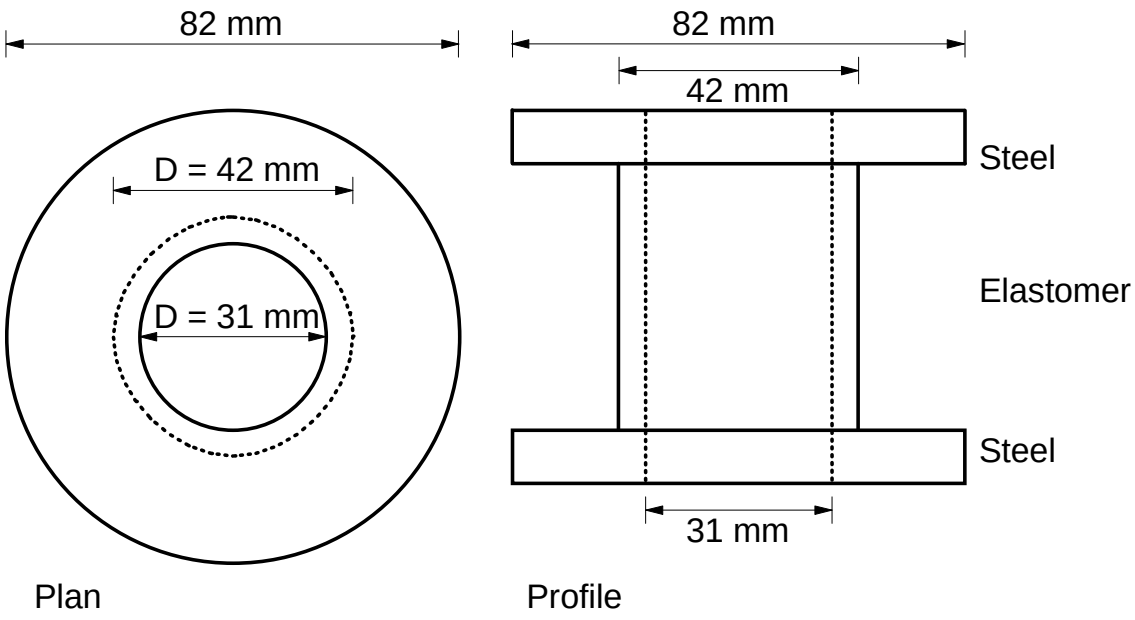

Figure 3.26: Typical ancillary shear cylinder specimen dimensions.

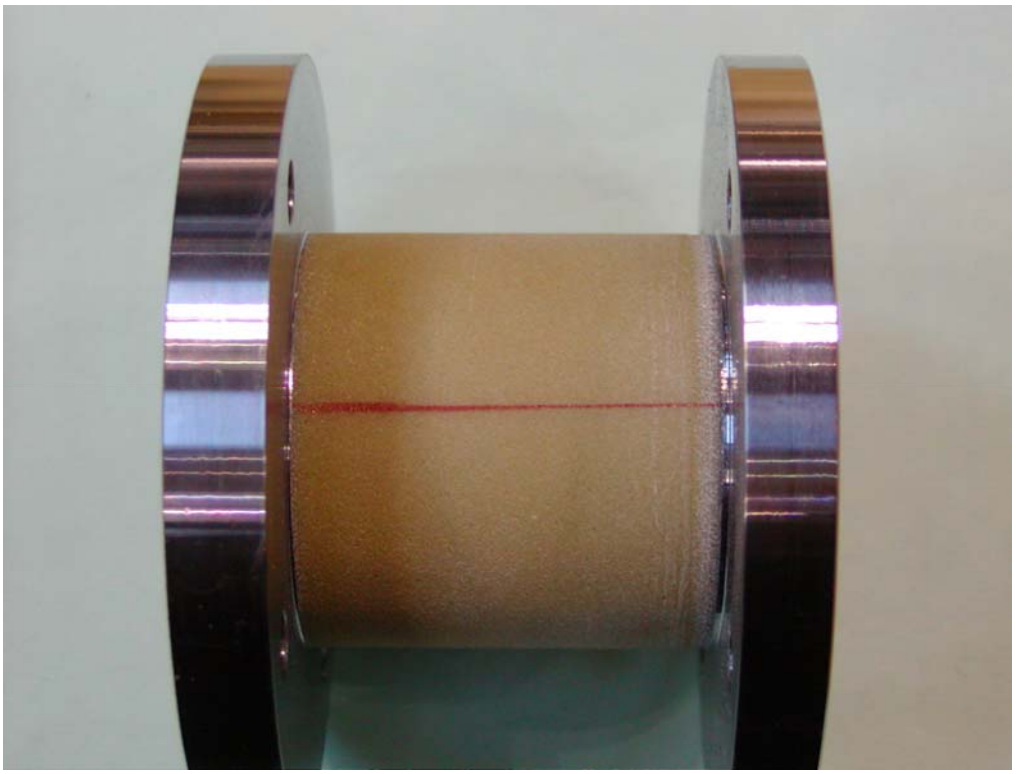

Figure 3.27: Shear cylinder specimen before testing.

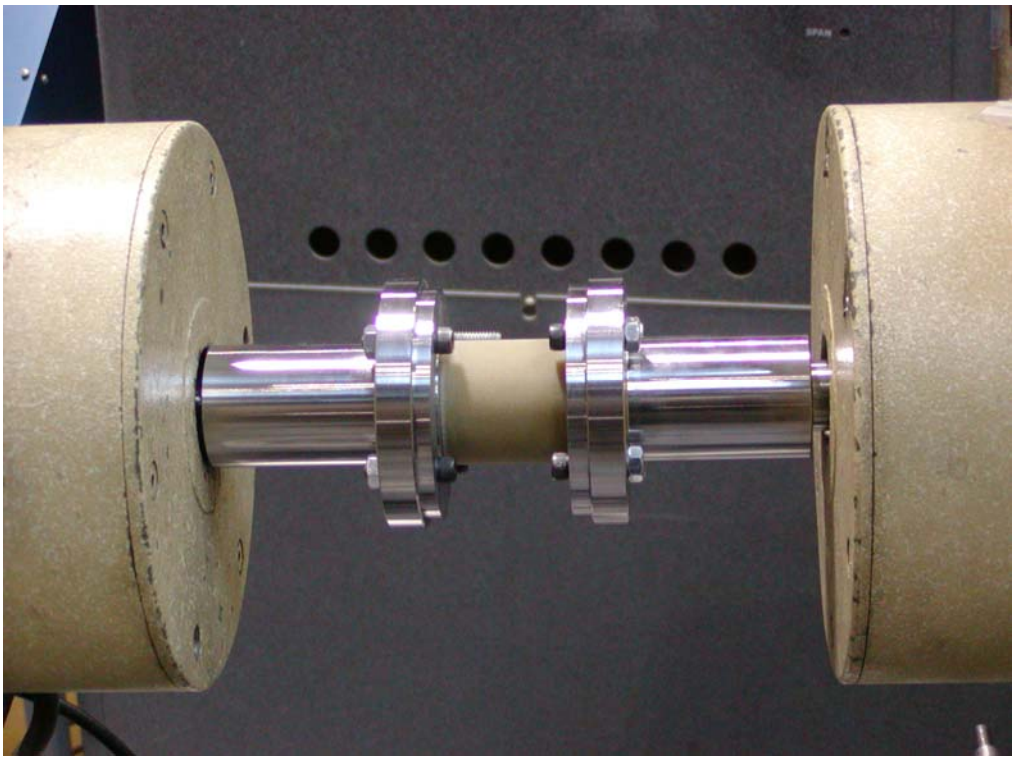

Figure 3.28: Shear cylinder tested in torsion machine.

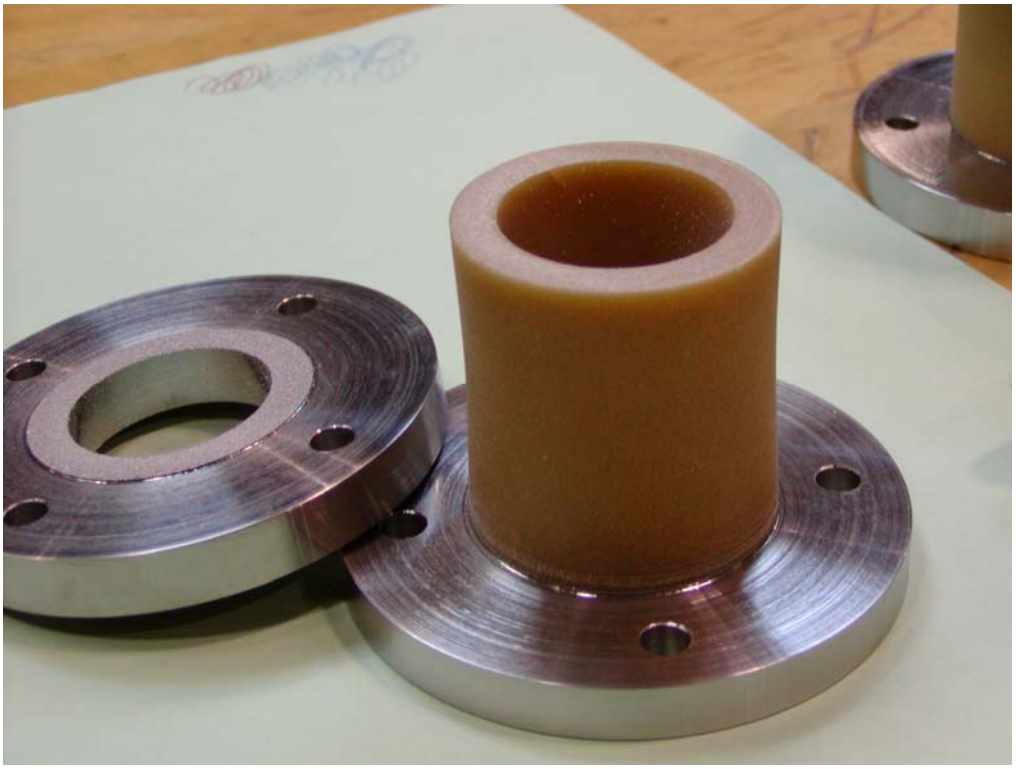

Figure 3.29: Shear cylinder after failure.

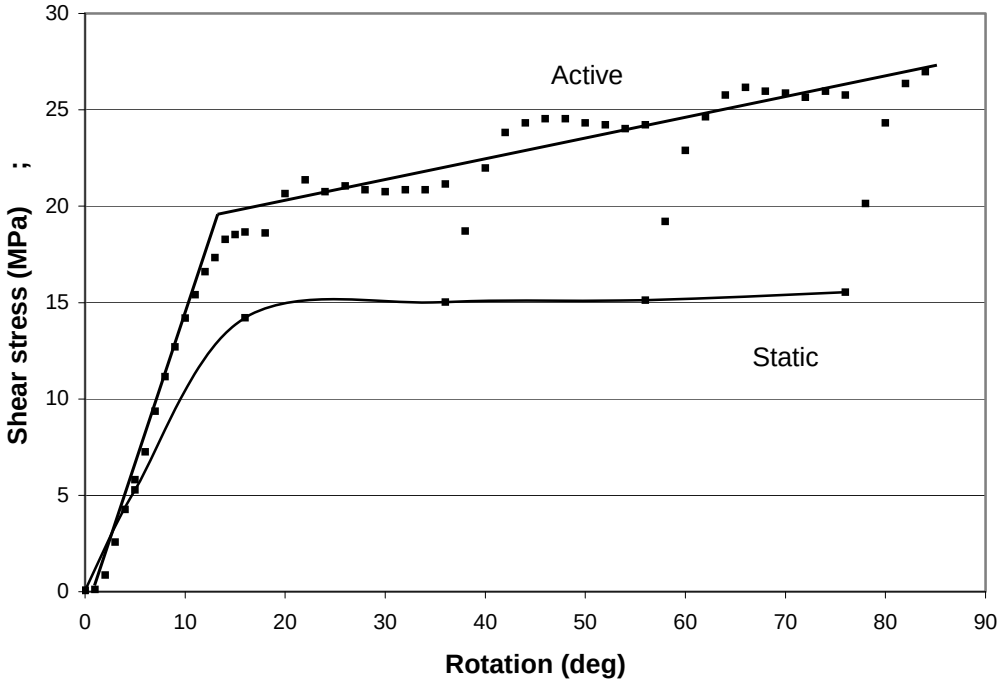

Figure 3.30: Typical torsion test result with both active load and static results.

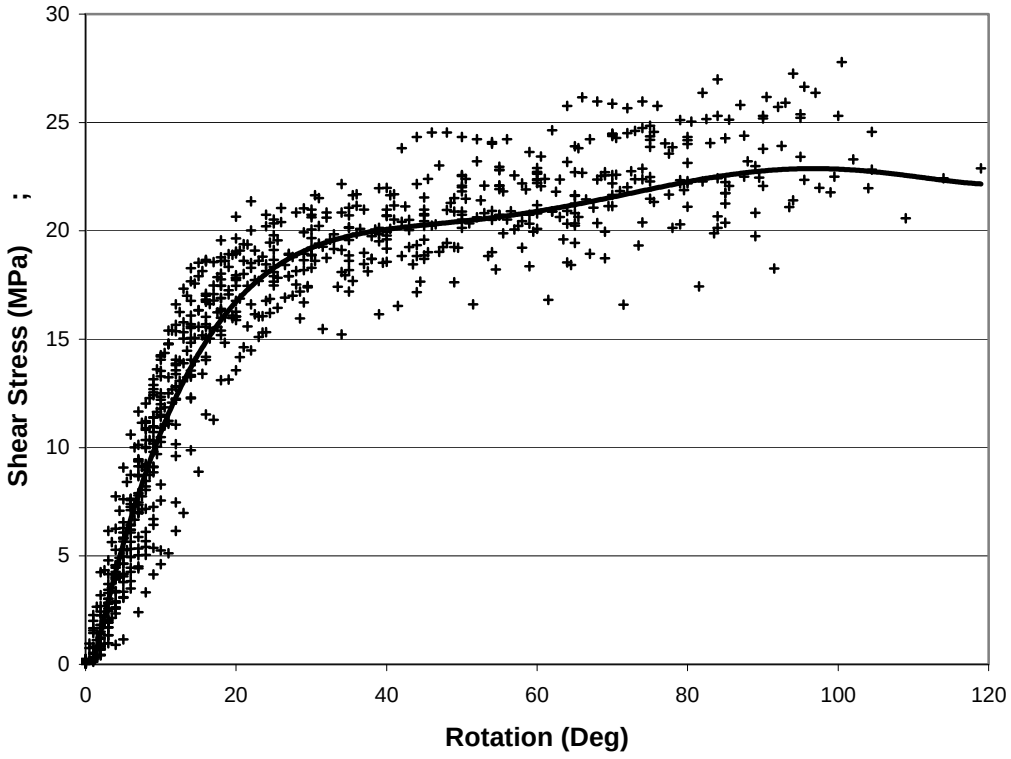

Figure 3.31: Active data from all torsion test specimens.

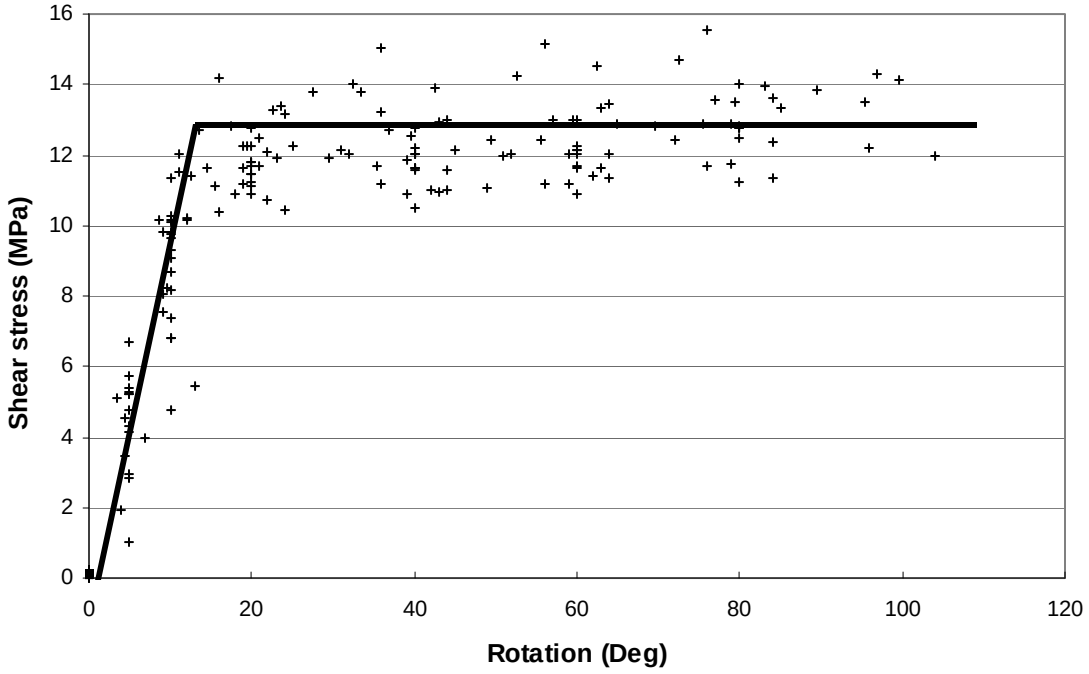

Figure 3.32: Static data from all torsion test specimens.

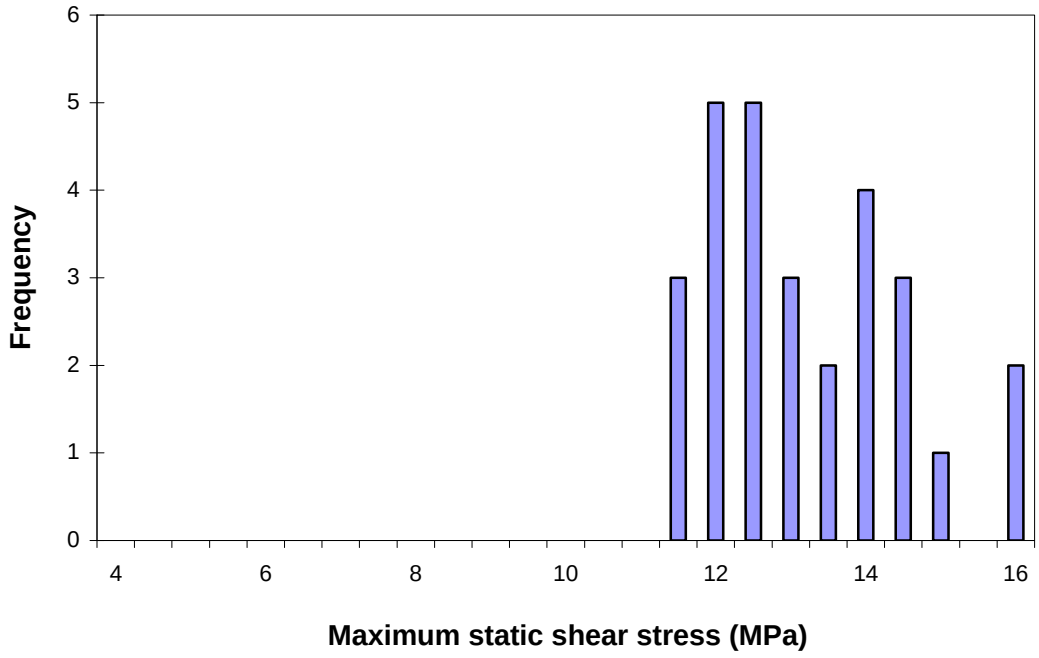

Figure 3.33: Histogram of torsion test results.

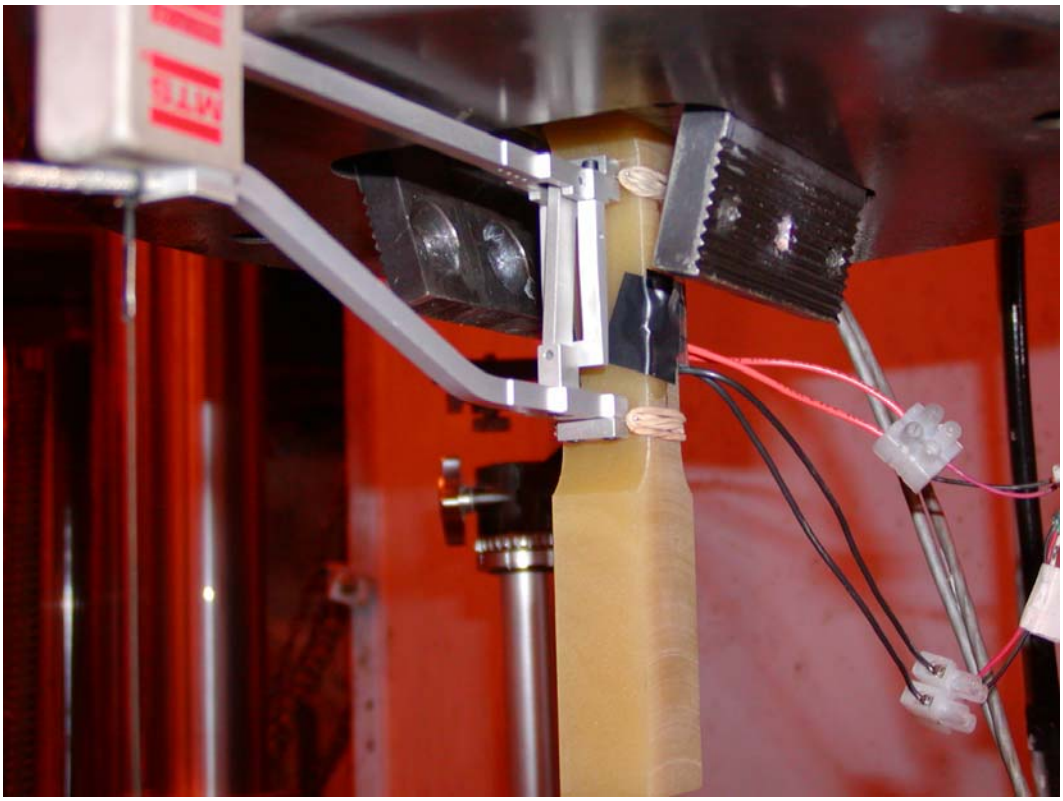

Figure 3.34: Elastomer tension coupon test.

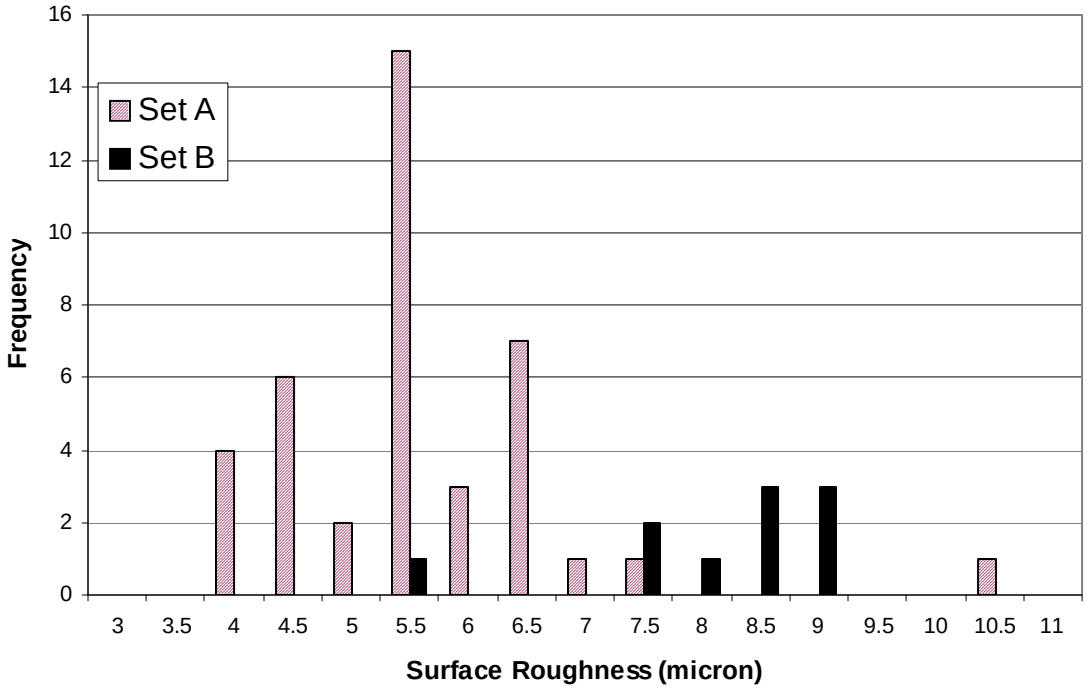

Figure 3.35: Ancillary surface roughness result histogram.

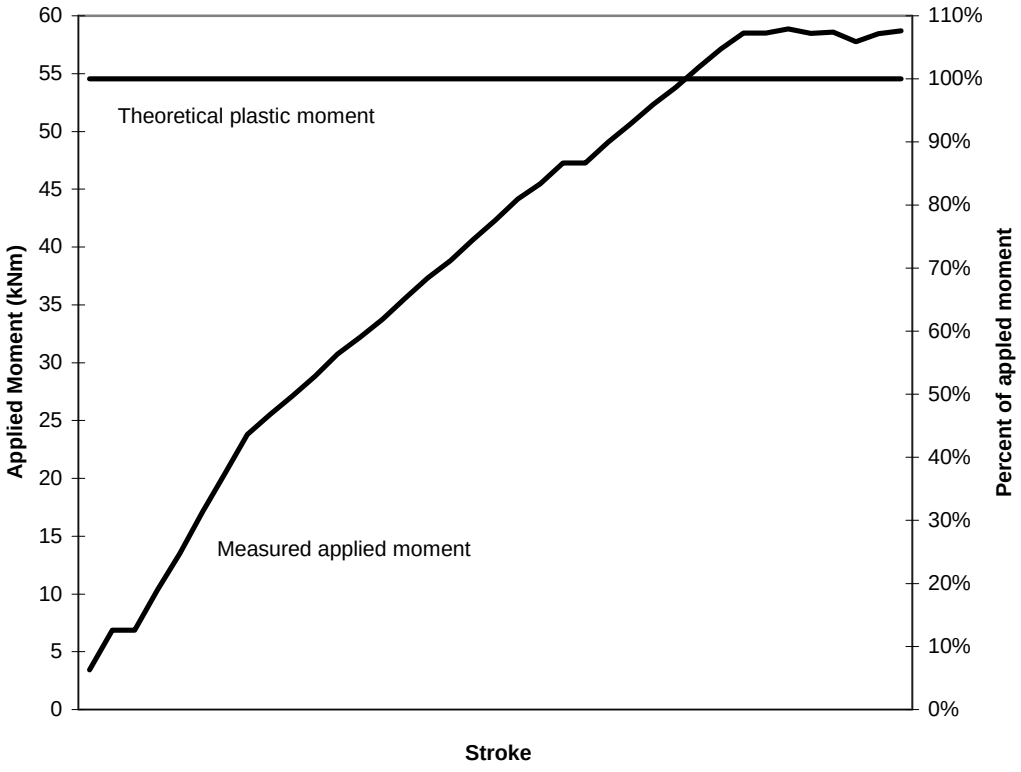

Figure 3.36: Sample applied moment vs. stroke diagram. (B6 shown)

4 EXPERIMENTAL RESULTS

This chapter presents the experimental results from the fatigue and static tests of the sandwich plate system (SPS) specimens. Section 4.1 presents the fatigue lives, load deflection, and strain range results for the fatigue test program. Section 4.2 presents load-shear deflection and load-strain results for the static tests.

4.1 Fatigue Tests

4.1.1 Fatigue Life

Table 4.1 lists the applied shear load range, shear stress range and the number of loading cycles endured by each specimen. Figure 4.1 presents the same data graphically. The static tests results are included as results with one cycle of loading.

Set “A” fatigue specimens failed by the separation at the steel-elastomer interface. Subsequent loading cycles after member failure at the interface caused the steel to deform plastically. Most cases of separation are visually obvious, as shown in figure 4.2. The steel plates show permanent deformations without any evidence of cracking or fatigue damage.

Set “B” specimens had one of two outcomes. First was the retirement of the fatigue test upon reaching 10 million loading cycles. Second was fatigue failure of the bottom steel plate.

The two specimens that survived the 10 million cycles without failure underwent further monotonic static load testing until failure. The monotonic static load has the same test setup as the fatigue test program. Figure 4.3 shows the subsequent test for the surviving specimens.

Figure 4.4 shows a fatigue crack from the bottom steel plate of one of the remaining three specimens. Because fatigue properties of the interface are the focal point of the current test program, fatigue failure of the steel layer provides little relevant information.

4.1.2 Load Deflection for Interval Tests

Figure 4.5 shows a typical load vs. actuator stroke diagram for a set of interval tests. There are minor variations in the member stiffness, as measured by the slope of the lines, over the course of testing. The starting and ending point (minimum and maximum load) of the test is drifting over the fatigue life of the specimen. There are two possible explanations for the varying deflections. Majority of the increased deflection can be attributed to creeping of the test specimen after cyclic loads. A portion of the drift at the beginning of the test can be attributed to seating of the test setup.

Table 4.2 lists the recorded applied load and stroke measurements for the interval tests. Initial values are data obtained from the interval test before any cyclic loading on the specimens. Final values are data obtained during the last interval test before specimen failure from cyclic loads.

4.1.3 Load Deflection for Dynamic Tests

Figure 4.6 to 4.15 show graphs of cycle vs. stroke for each specimen. The data in the graphs are the recorded actuator stroke at maximum and minimum loads. The mid-span deflections at both minimum and maximum loads increased over the course of testing but the deflection at minimum load increased less than that at maximum loads.

4.1.4 Shear Span Strain Rate from Interval Tests

Figure 4.16 shows typical steel surface strains vs. applied loads. Results for other specimens are similar. Figures 3.12 and 3.13 show the strain gauge locations. There is good agreement between strain data from geometrically similar locations. The data shows the specimen responded symmetrically to the applied load.

4.1.5 Shear Span Strain Rate for Dynamic Tests

The strain readings for this experiment did not respond fast enough to keep up with the loading rate. The strains recorded have amplitudes lower than the expected values. The exact cause of the attenuated strain data is unknown, but it is believed to be related to the difference in the way the data acquisition system treats differential voltage reading associated with load cells and strain gauges. The amplitude data remain meaningful because they are proportional to the actual strains and provide continual indication to member response.

Figure 4.17 and 4.18 show two examples of steel surface strain amplitudes recorded during dynamic tests. Geometrically similar locations show amplitude values and data trends similar to the presented values. The figures show stable strain amplitude readings over the majority of the fatigue life with significant changes toward the end of the tests.

4.2 Static Test Results

The static tests were designed to permit higher shear loads before the yielding of steel plates, but steel strain gauge data show parts of the member were yielded before a shear failure. The recorded static results are obtained for yielding failures.

4.2.1 Shear Force vs. Shear Displacement

Figure 4.19 defines the shear deformation for the static tests, A6 and B1. Figure 4.20 presents a diagram for the applied shear force vs. shear deflection. The wider cross-section of specimen A6 provided a higher elastic stiffness and hence, a stiffer response than B1. B1 sustained higher shear loads compare to A6 because B1 steel layers had higher yield strengths.

4.2.2 Shear Force vs. Steel Strain

Figure 4.21 and 4.22 shows the applied shear force and the responding steel strains. Figure 3.15 shows the gauge locations and numberings. The diagrams show the strains of the specimens to beyond the yielding point. The strains responded linearly to the applied load in the elastic range. Gauges in geometrically anti-symmetrical locations recorded similar values, indicating that the members were loaded and responded as intended.

4.2.3 Shear Force vs. Elastomer Principal Strain

Figure 4.23 shows a diagram comparing the shear force vs. principal strain for the static tests. Diagonally oriented gauges installed at the elastomer layer recorded the principal strains. The range of the electronic data acquisition limited the maximum strain values recorded. The strains recorded on both sides of the elastomer had similar magnitudes, which indicated the member experienced similar loading across its cross-section and there is no evidence of twisting. The similar magnitudes of tension and compression strain values indicate the strain gauges are correctly orientated and recorded the anticipated principal strains. With the strain gauges located on the elastomer under biaxial loading, the accuracy of the recorded strains is affected. The strain gauges are manufactured for uni-axial loading of steel with a Poisson ratio of 0.28, the difference in Poisson ratio and stress field would cause 2% variations in the strain data assuming ±10% transverse sensitivity and elastomer Poisson ratio of 0.35. (Measurements Group, 1993)

Table 4.1: Nominal Load range and fatigue life of specimen.

	Shear Load Range (kN)			Shear Stress Range (MPa)			
Specimen	**Minimum**	**Maximum**	**Range**	**Minimum**	**Maximum**	**Range**	**Fatigue life**
A1	2.4	37.4	35.0	0.2	3.2	3.0	74,956
A2	2.6	27.1	24.5	0.2	2.3	2.1	310,036
A3	2.7	22.9	20.2	0.2	1.9	1.7	1,741,373
A4	2.2	20.4	18.2	0.2	1.7	1.5	530,509
A5	2.5	20.7	18.2	0.2	1.8	1.5	623,059
A6	0.0	125.5	125.5	0.0	10.5	10.5	1
B1	0.0	159.0	159.0	0.0	18.0	18.0	1
B2	4.0	23.7	19.7	0.4	2.2	1.8	2,809,077
B3	2.6	31.9	29.4	0.2	3.1	2.8	10,000,000
B4	12.8	43.2	30.4	1.1	3.7	2.6	3,137,126
B5	2.5	48.0	45.5	0.2	4.1	3.9	893,752
B6	34.7	45.1	10.4	3.0	3.9	0.9	10,000,000

Table 4.2: Applied load and stroke values obtained from interval tests.

	Initial				Final			
Specimen	**Min applied load (kN)**	**Min stroke (mm)**	**Max applied load (kN)**	**Max stroke (mm)**	**Min applied Load (kN)**	**Min stroke (mm)**	**Max applied Load (kN)**	**Max stroke (mm)**
A1	5.08	1.33	75.28	13.79	5.19	1.92	75.34	14.06
A2	4.64	1.01	54.67	9.79	4.53	1.45	54.71	10.21
A3	5.21	14.22	45.06	20.67	5.25	1.29	44.78	8.79
A4	5.19	1.32	40.79	7.36	4.71	0.93	40.68	8.06
A5	4.51	0.83	40.54	6.92	5.05	0.88	41.06	6.97
B2	-0.08	0.00	46.39	8.03	-0.16	10.56	46.96	18.68
B3	4.77	9.12	64.78	19.78	0.82	10.62	64.75	21.85
B4	0.06	0.00	84.31	14.61	1.26	-25.51	85.86	-8.96
B5	1.36	-36.79	95.95	-22.96	0.90	-34.03	96.52	-21.74
B6	1.26	0.00	90.05	13.78	1.47	5.10	90.82	17.49

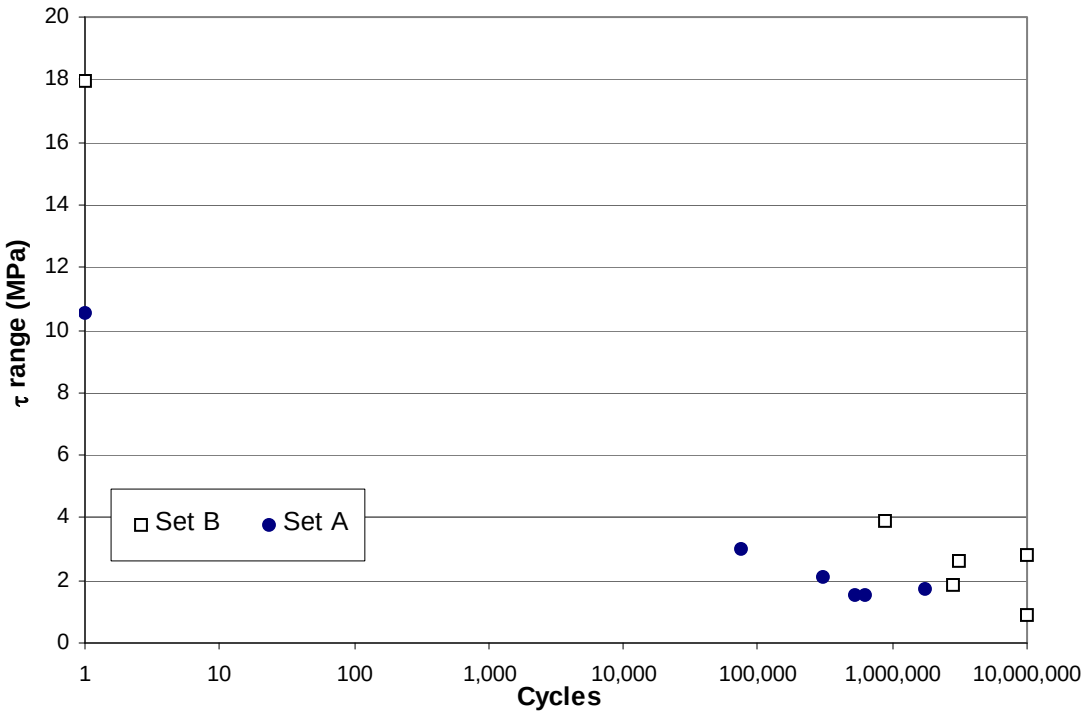

Figure 4.1: Fatigue live for set "A" and "B".

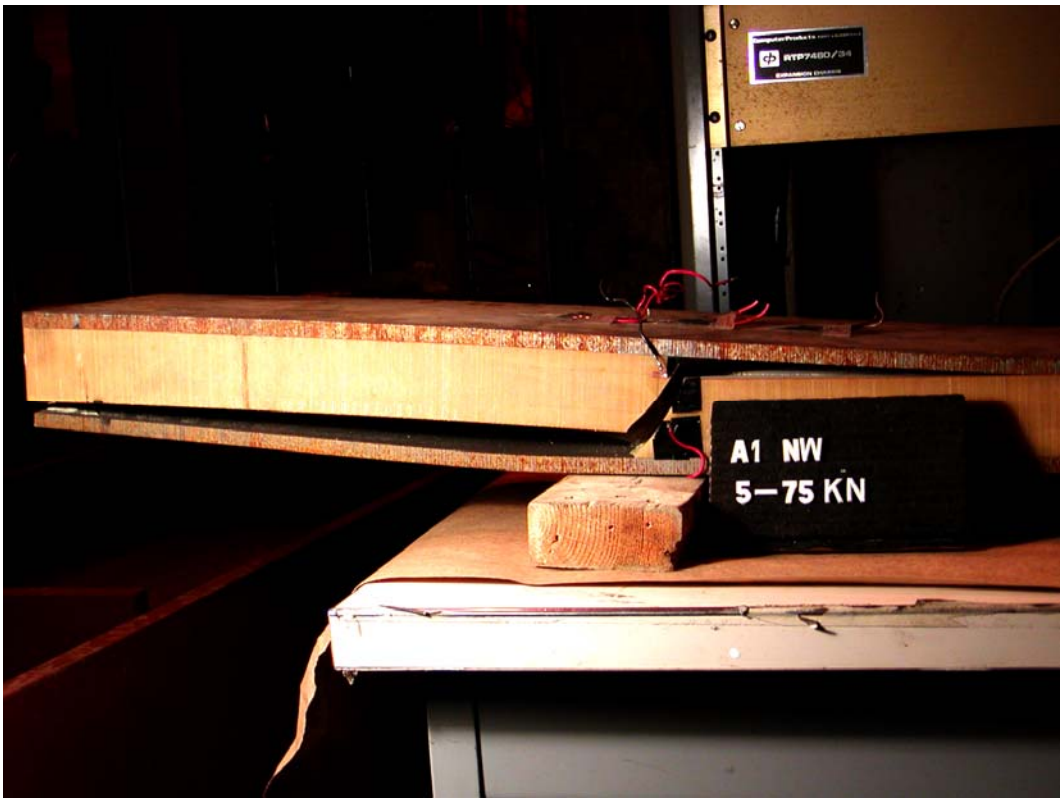

Figure 4.2: Failure of the steel-elastomer interface (A1 shown).

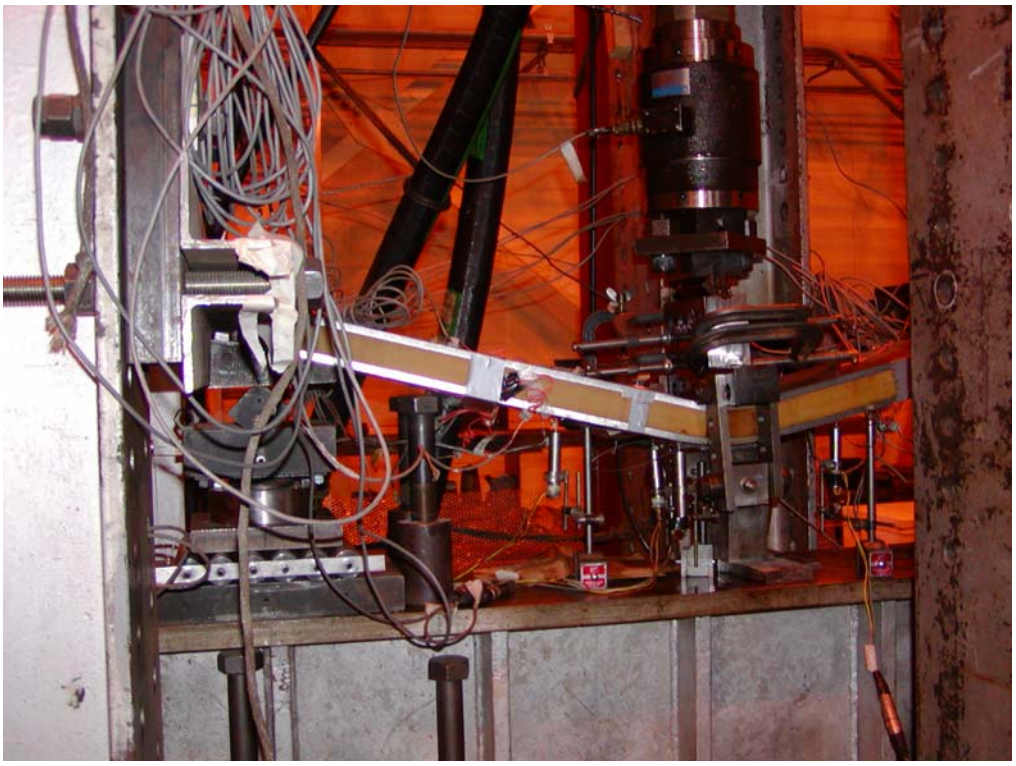

Figure 4.3: Static loading of specimen after 10 million loading cycles (B3 shown).

Figure 4.4: Fatigue failure of bottom steel plate (B5 shown).

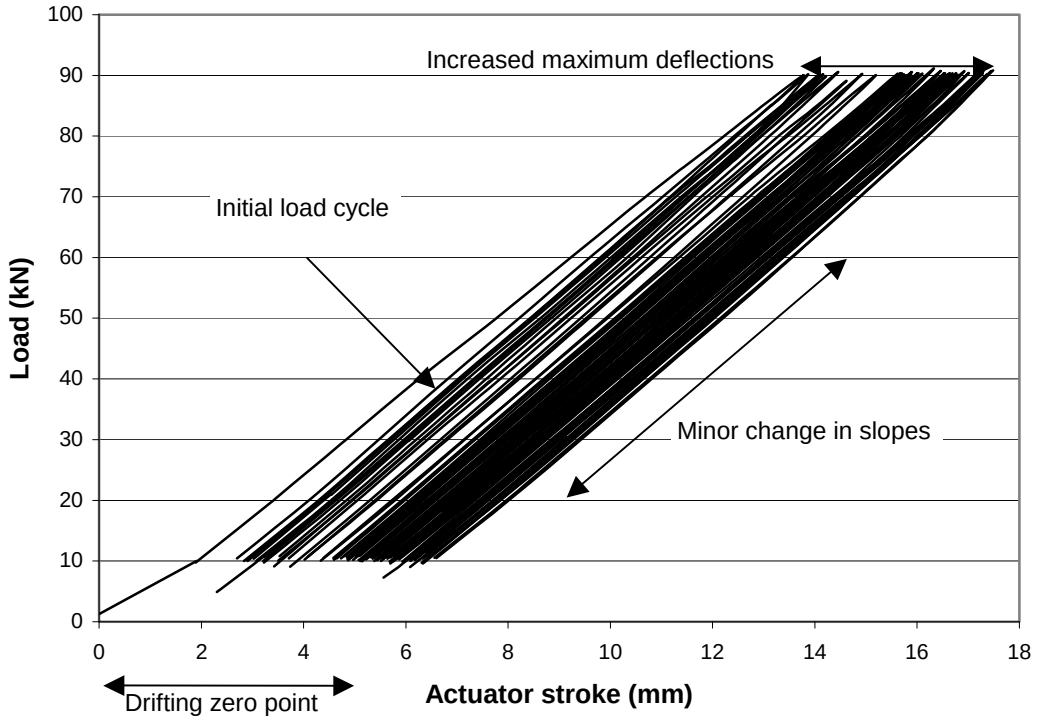

Figure 4.5: Sample load-displacement of interval tests (Data obtained from B6).

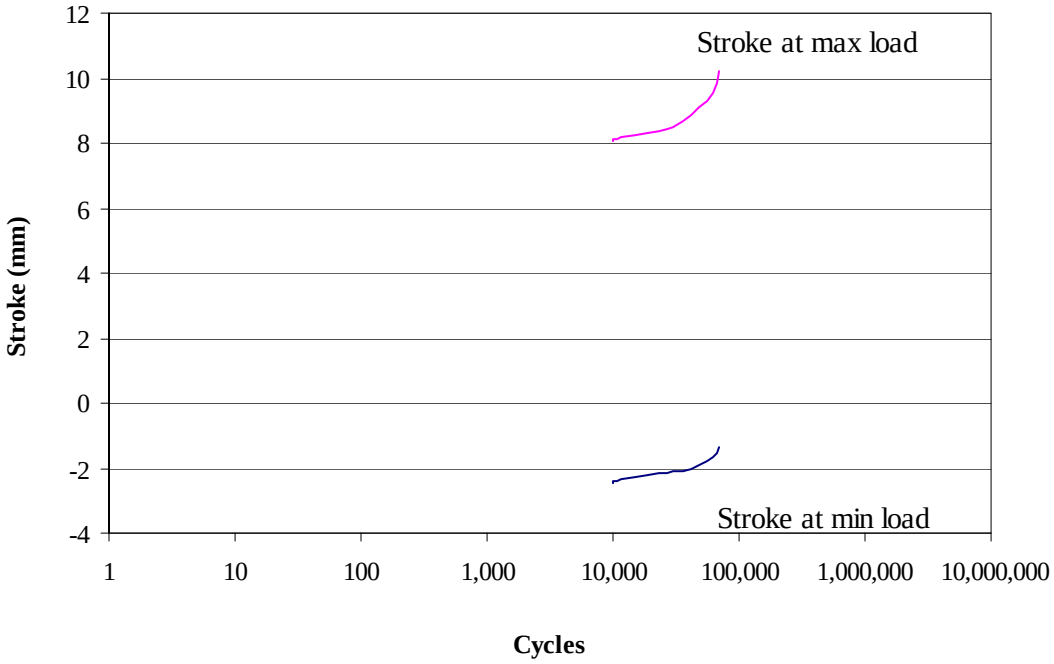

Figure 4.6: Stroke vs. cycle diagram from dynamic test results for A1.

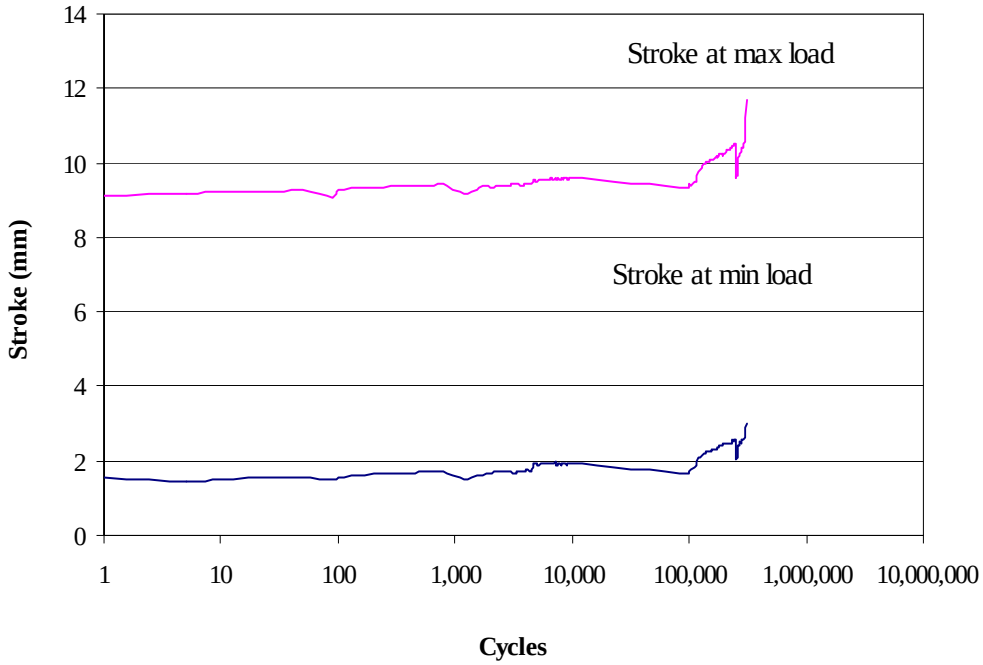

Figure 4.7: Stroke vs. cycle diagram from dynamic test results for A2.

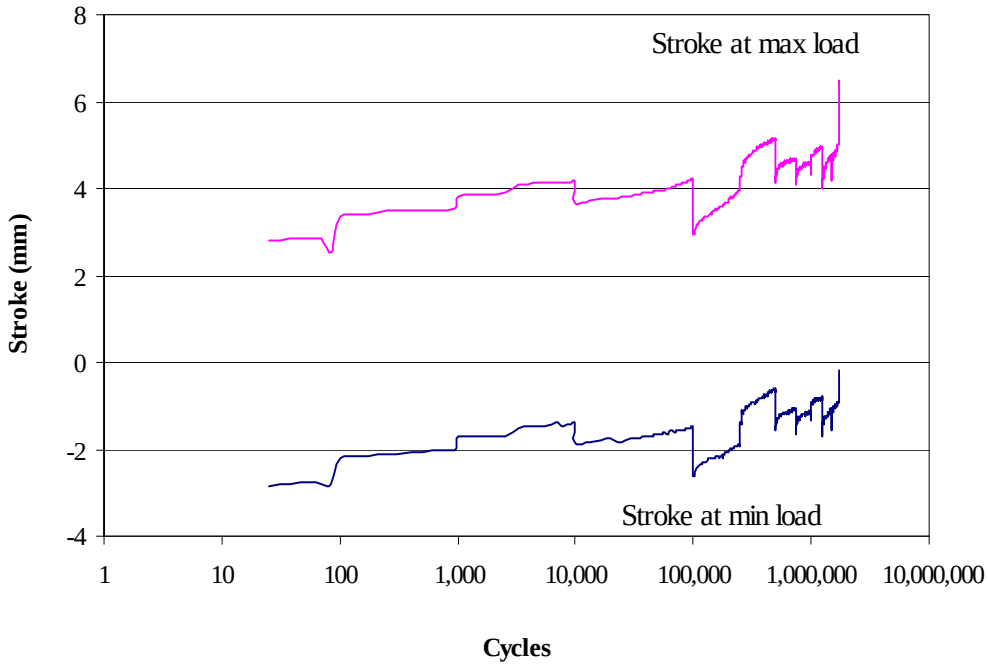

Figure 4.8: Stroke vs. cycle diagram from dynamic test results for A3.

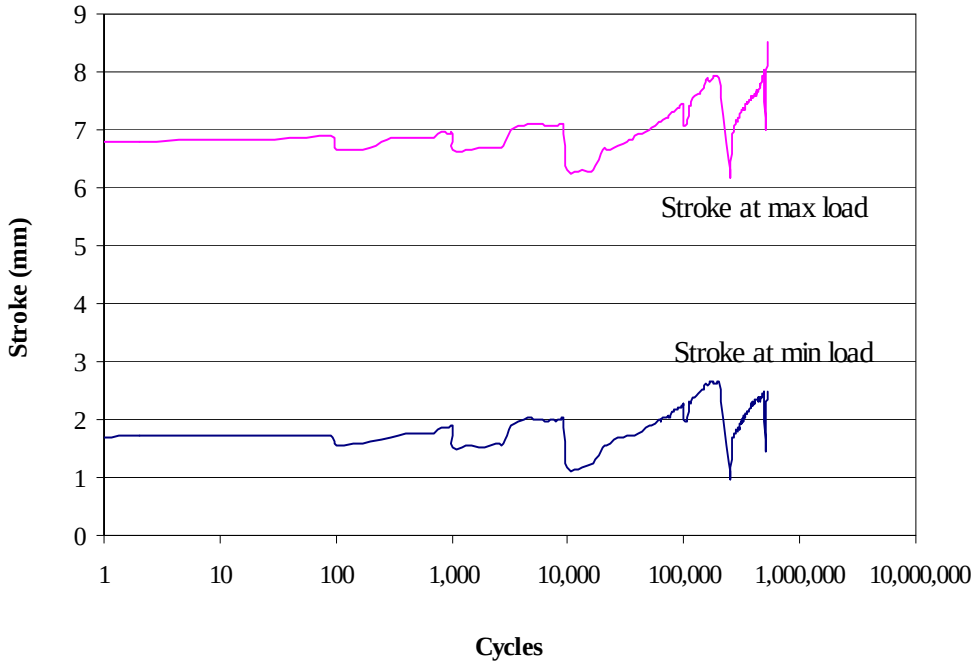

Figure 4.9: Stroke vs. cycle diagram from dynamic test results for A4.

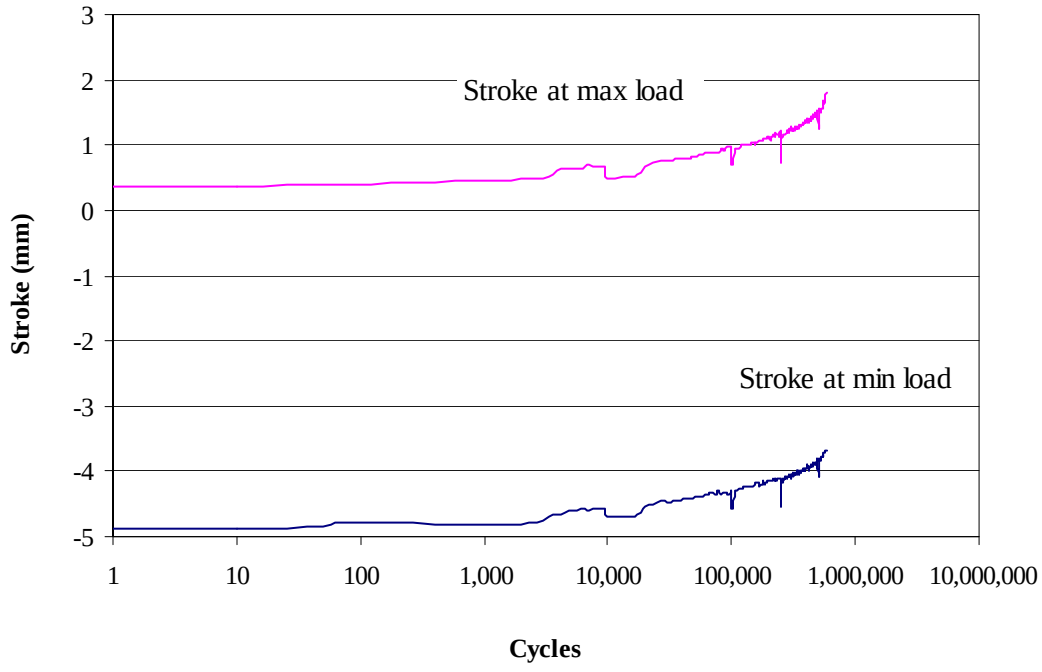

Figure 4.10: Stroke vs. cycle diagram from dynamic test results for A5.

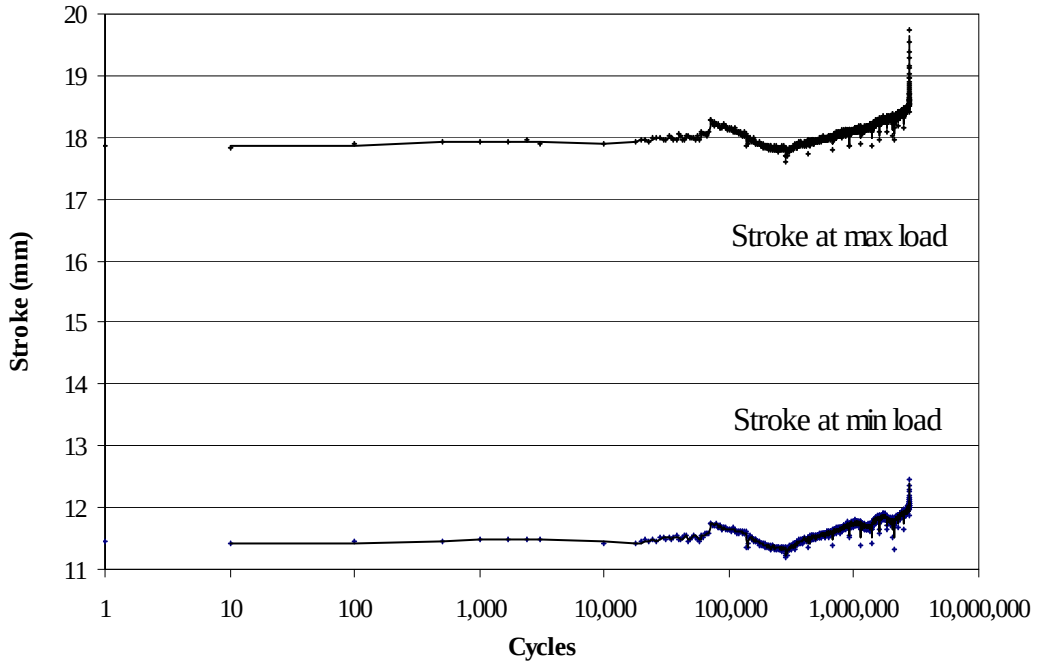

Figure 4.11: Stroke vs. cycle diagram from dynamic test results for B2.

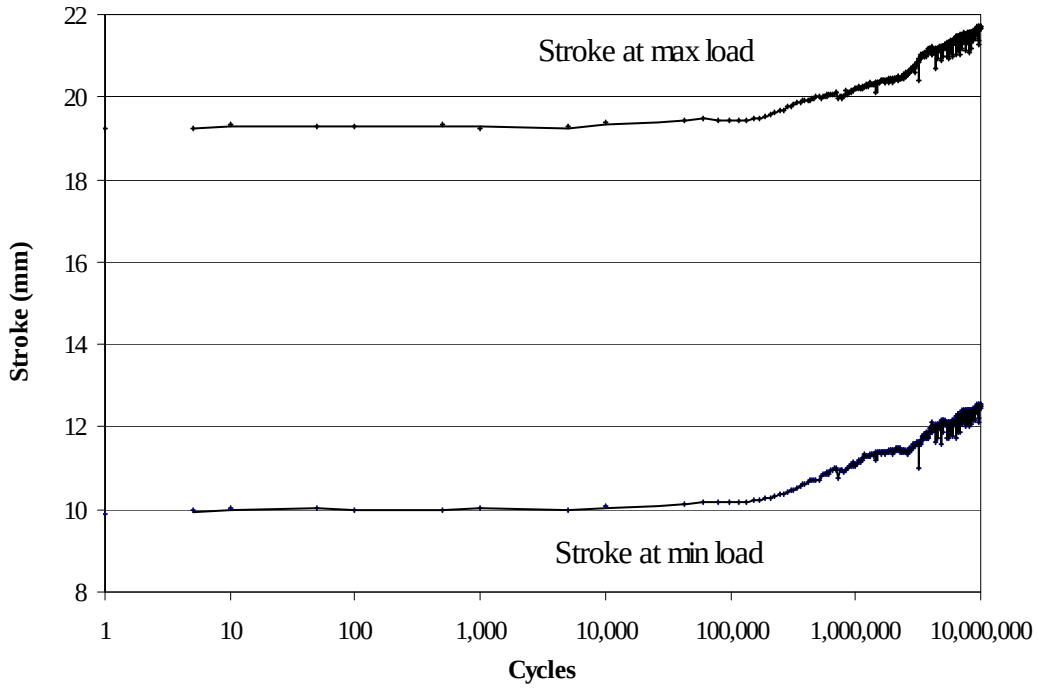

Figure 4.12: Stroke vs. cycle diagram from dynamic test results for B3.

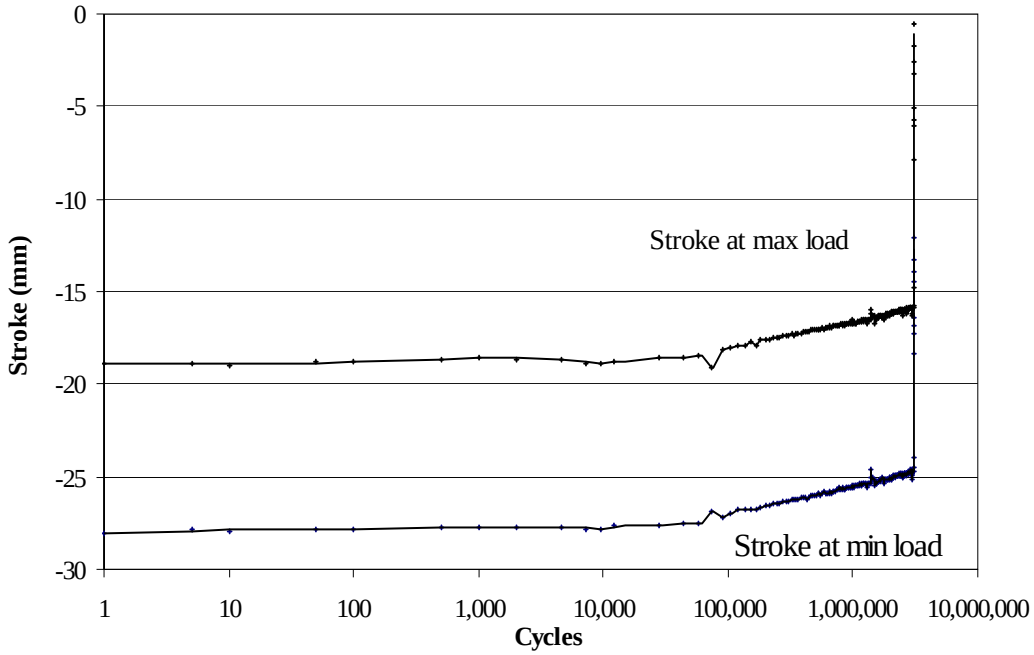

Figure 4.13: Stroke vs. cycle diagram from dynamic test results for B4.

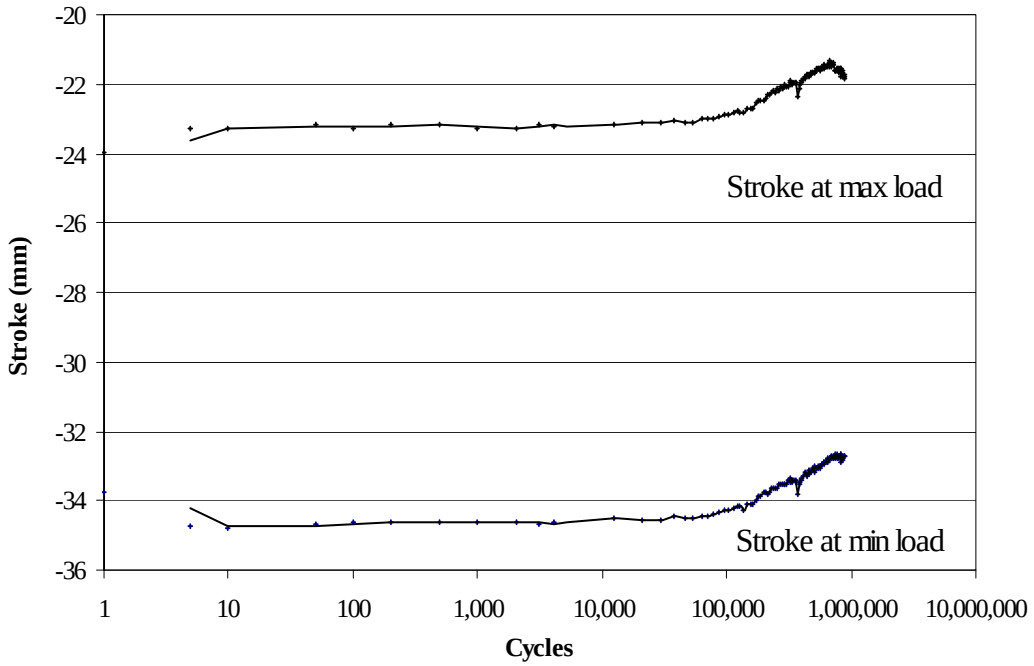

Figure 4.14: Stroke vs. cycle diagram from dynamic test results for B5.

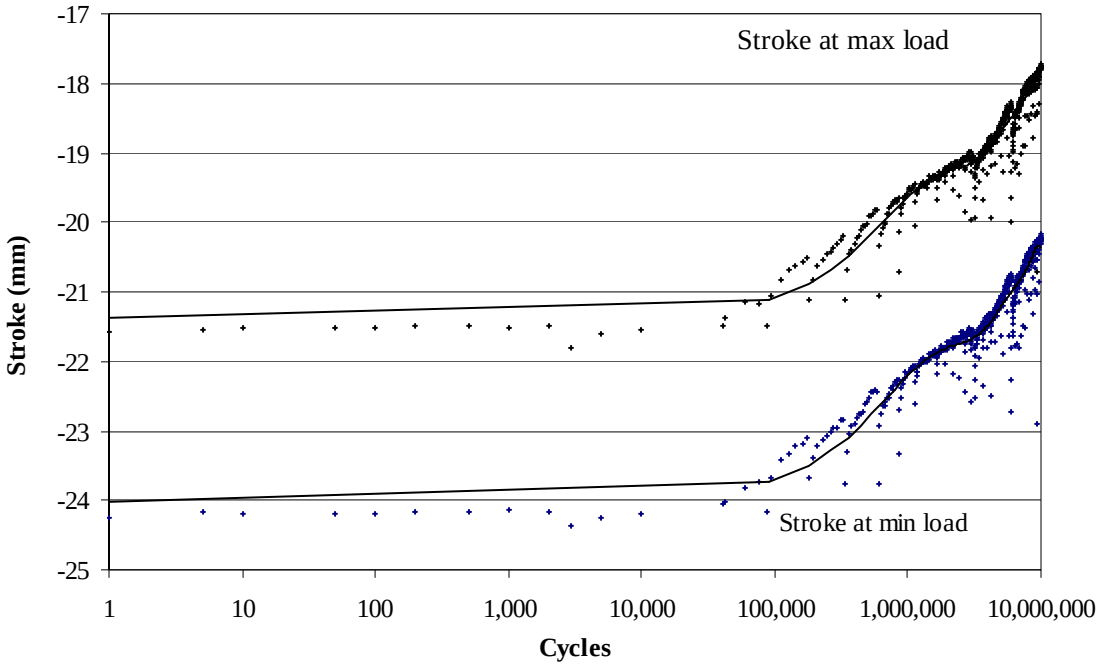

Figure 4.15: Stroke vs. cycle diagram from dynamic test results for B6.

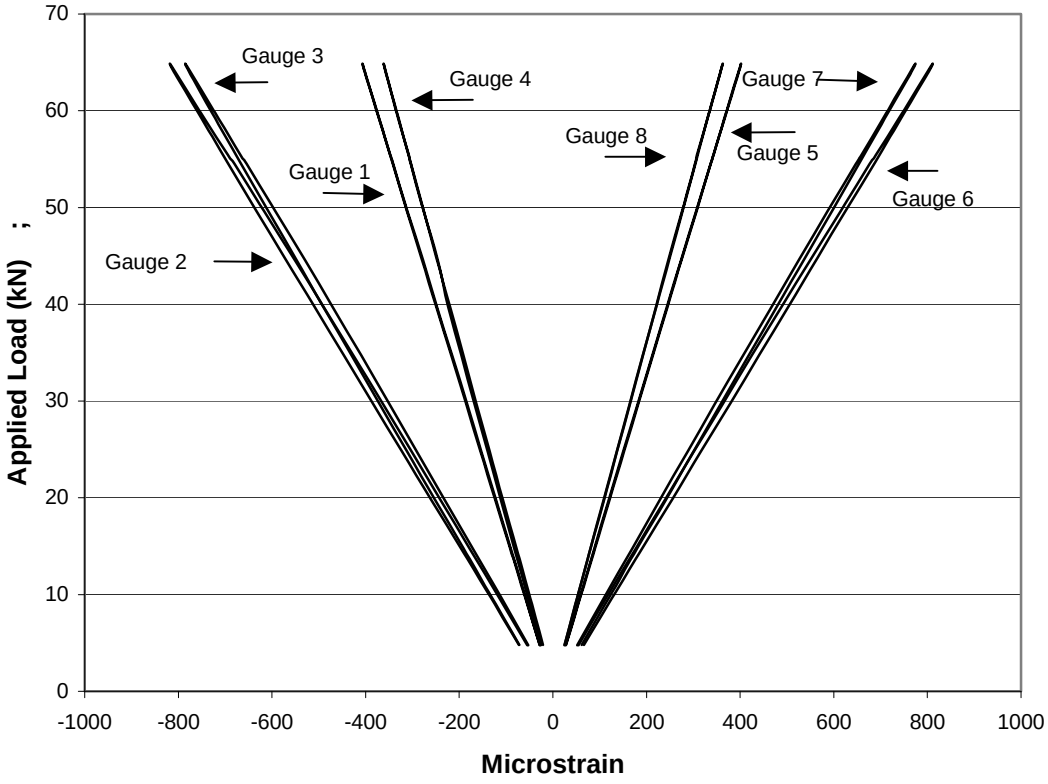

Figure 4.16: Strain vs. applied load (B3 shown).

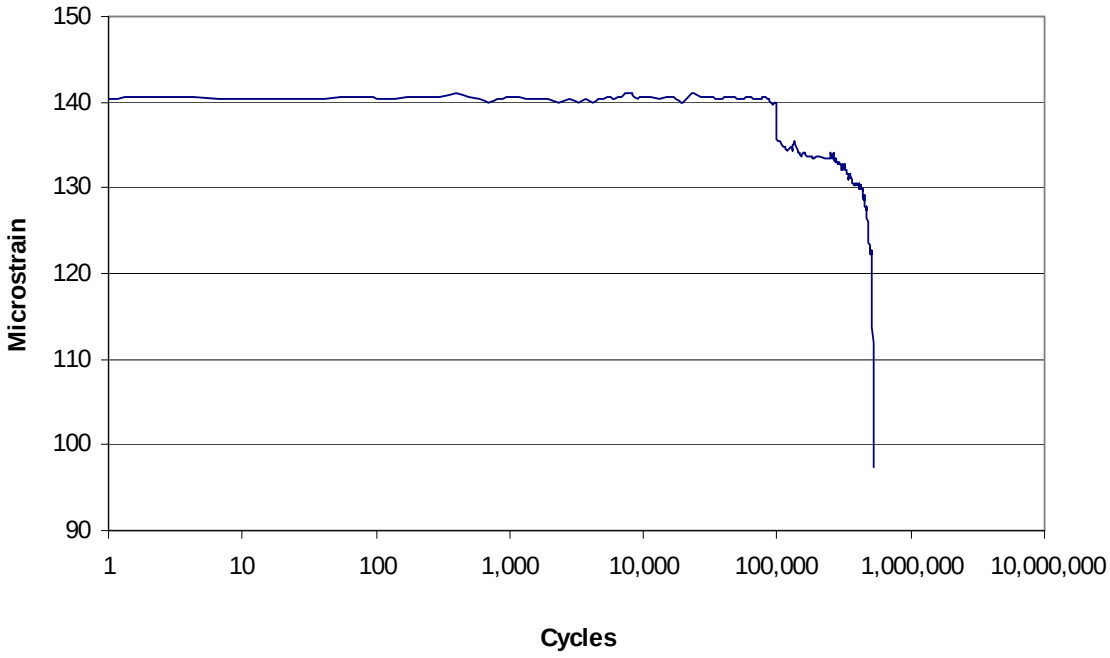

Figure 4.17: Strain at steel surface during dynamic test. (Gauge #2 of A4 shown)

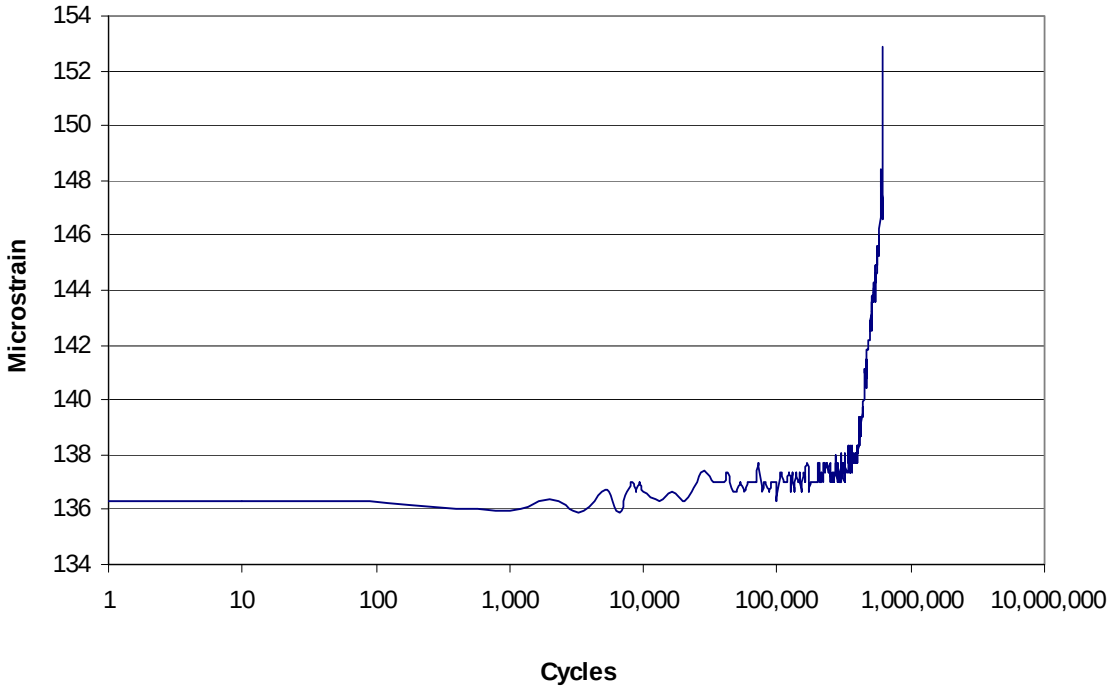

Figure 4.18: Strain at steel surface during dynamic test. (Gauge #2 of A5 shown)

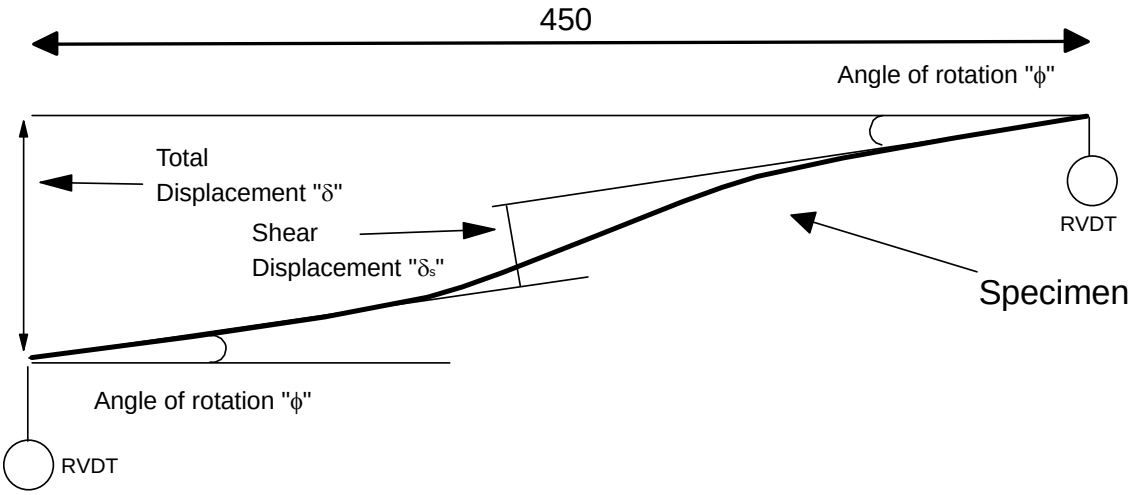

Figure 4.19: Definition of shear displacement for the static tests.

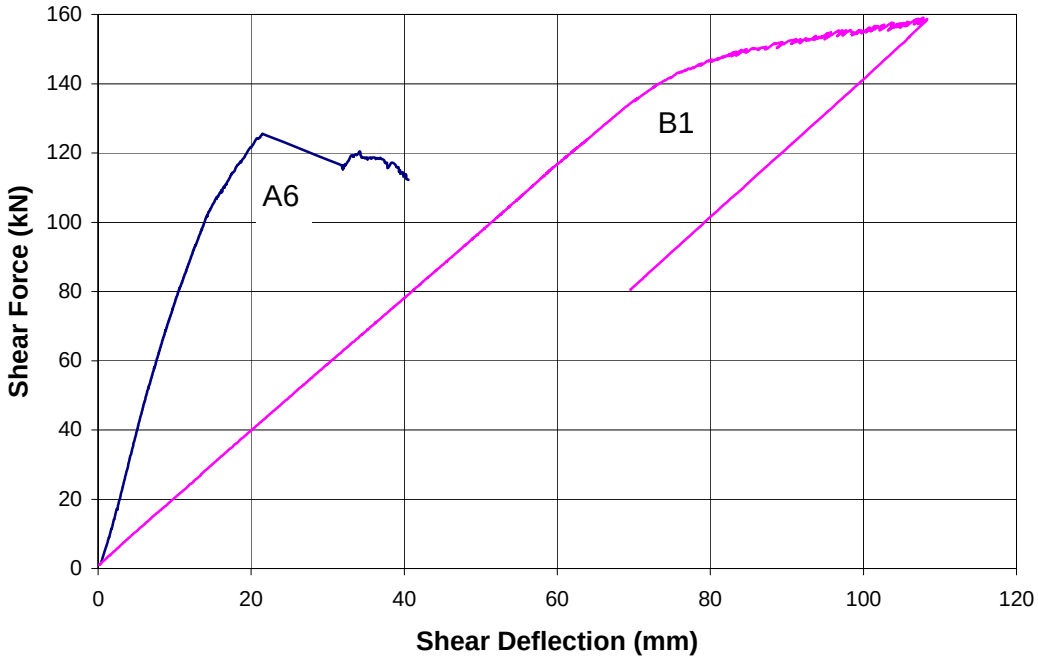

Figure 4.20: Applied load verses shear deformation for the static tests.

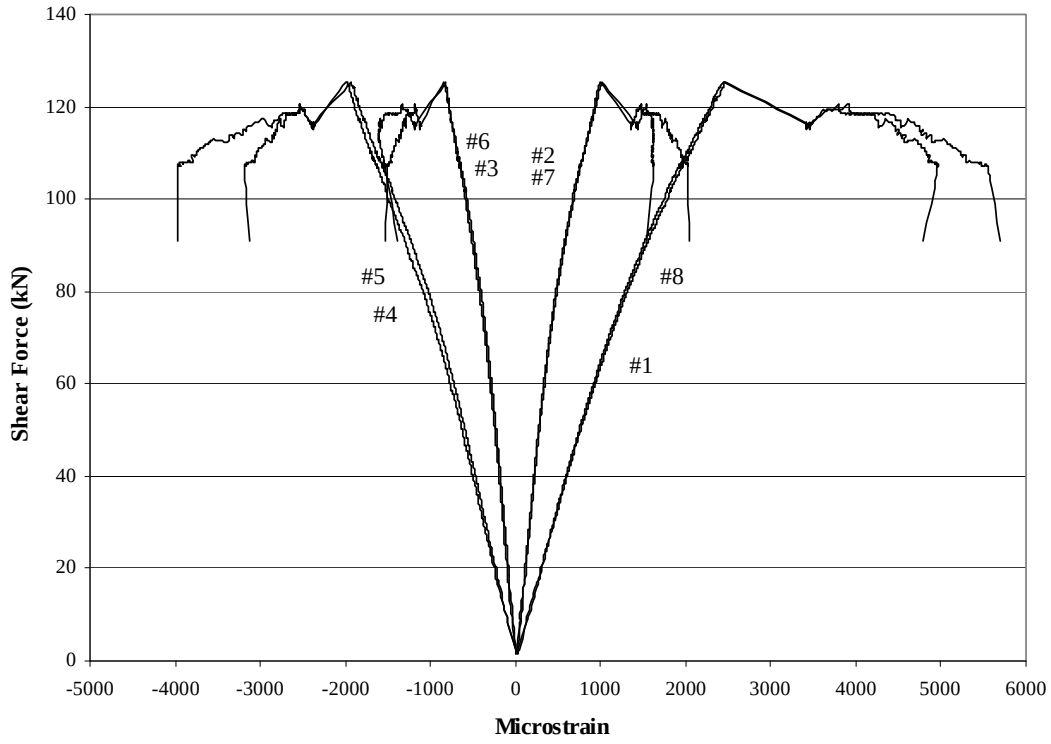

Figure 4.21: Steel strain vs. shear force for A6.

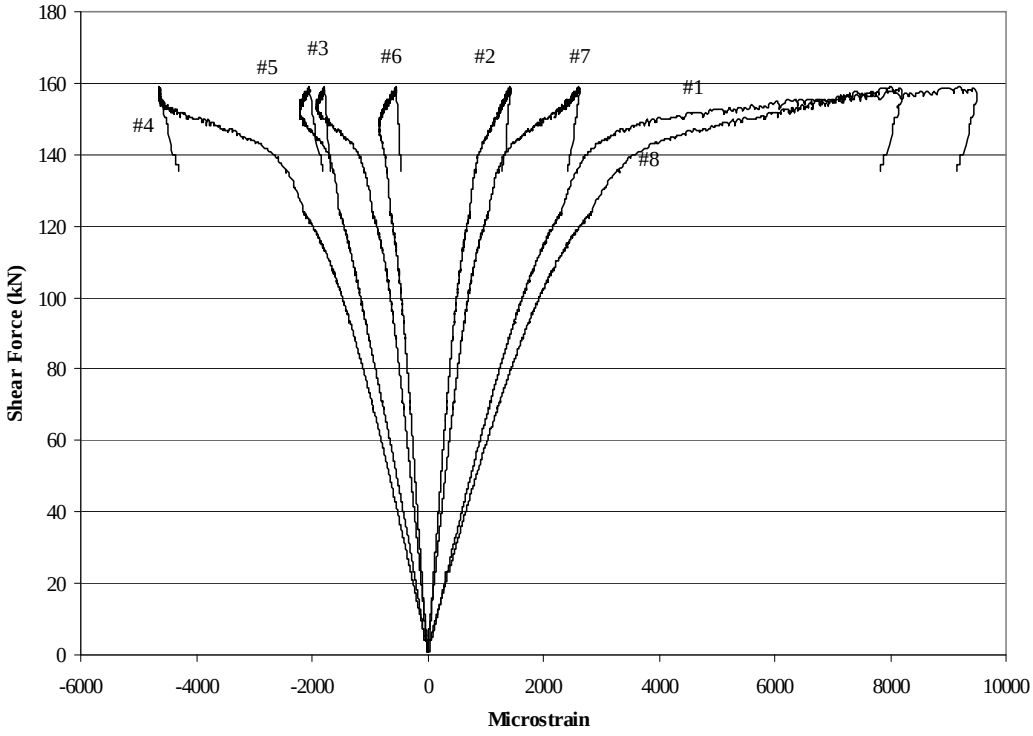

Figure 4.22: Steel strain vs. shear force for B1.

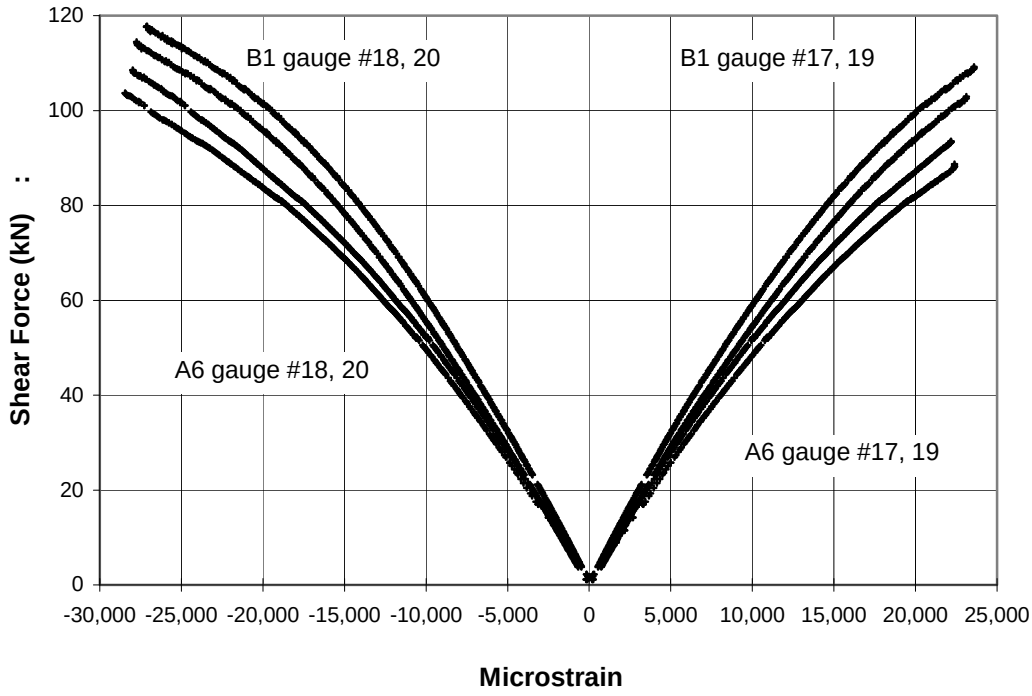

Figure 4.23: Principal strain at elastomer layer during static tests.

5 DATA ANALYSIS

5.1 Detailed vs. Idealized Loading Diagrams

5.1.1 Dynamic Loading Diagram

Figure 5.1 shows the detailed free body, shear force and bending moment diagrams for the fatigue tests. The diagrams illustrate the effects of the boundary conditions. The width of the loading plate separates the mid-span load into two point loads. Figure 5.2 shows the idealized diagrams. The idealized diagram treats the mid span load as a single point load.

Although the actual diagrams represent realistic loading conditions, the idealized diagrams provide simpler geometries and form the basic foundation for the coupled shear wall deflection model. The magnitude of error associated with the idealized diagrams is a combination of second order effects and differences between the shear and moment diagrams.

5.1.1.1 Second Order Effects

As the beam deflects, the reaction points, vertically supported by rollers, move away from the applied load. The deflected member shape and the movement of the reaction points increase the shear span, defined as the distance between the reaction and applied load points, of the member. The shear span increase is approximately linear with load and is about 0.7% at an applied load of 90 kN, assuming that the deflected shape is parabolic.

5.1.1.2 Shear Force Diagram

The maximum magnitude of shear for the two diagrams is identical. The boundary condition at the load point causes a disturbed region at the mid-span. However, the disturbed region has minimal effects on the test region where the strain gauges are located. Assuming shear deflection is proportional to the area under the shear force diagram, the idealized diagram overestimates the shear deflection by 4.8%.

5.1.1.3 Bending Moment Diagram

The magnitude of bending moment is similar between the two diagrams for the most of the specimen. The idealized diagram overestimates the moment at mid-span by 4.7%. The area of the bending moment diagram is assumed directly proportional to flexural deflection. In combination with second-order effects, which increased the shear span by 0.7%, the idealized loading diagram should underestimate flexural deflection by 0.2%.

5.1.1.4 Conclusion for Dynamic Loading Diagrams

The comparison between the idealized diagrams and the detailed loading diagrams, with second order effects accounted for, shows minimal differences. With idealized diagrams, overestimations of the shear deflection partially compensate the underestimation of the flexural deformation.

5.1.2 Static Tests Diagrams

Figure 5.3 shows the idealized free body; shear force, and bending moment diagrams for the static test. The justification for the idealized diagrams is the boundary conditions do not affect the interface forces within the test region.

5.2 Strain Distribution

A strain distribution for the cross-section for the sandwich plate system (SPS) is assumed and justifications for the distribution are given. A realistic strain distribution is needed to guide the choice of appropriate analytical models for the SPS.

5.2.1 Linear Strain Distribution

A linear strain distribution is assumed for the SPS based on practical conveniences and experimental justifications.

A linear strain distribution provides three practical benefits. The first is simplicity because only data from the steel strain gauges are required. The second is the amount of redundancy obtained from measurements of other steel surface gauges. With redundant measurements, strains from geometrically similar locations provide averages that are statistically more reliable than any single measurement. The third is that by using the large strains at the steel surfaces, the random errors associated with electronic noise are less significant.

There are three experimental justifications for a linear strain distribution for the SPS.

First, a linear strain distribution provides satisfactory agreement between measured and calculated steel surface strains as shown in section 5.2.3.

Second, the recorded strain values show only minor deviations from linear approximations as illustrated in figure 5.4. The figure shows strain values at peak loads for specimen A1 through A5 during interval tests.

Third, the only basis for rejecting a linear distribution would be the strain results from gauges on the elastomer. The elastomer strain results are less reliable than those at the steel surface for two reasons. First, the strain gauges are calibrated for uniaxial stress in steel, which is the stress state of the steel plates. The strain gauges will register higher strain values at the elastomer because of the higher Poisson's ratio and biaxial stress condition of the elastomer. The errors associated are estimated to be less than 2% with a

gauge transverse sensitivity range of ± 10% (Measurements Group, 1993). Second, the strain gauges on the steel surface have exact elevations for the whole gauge while the gauges on the elastomer surface are vulnerable to elevation errors. The gauges also covered a finite width of the elastomer. An elevation error of 1.0 mm can influence strain results by 10 με, which is approximately 3% of the expected strain. The result of covering a finite width of the elastomer is that the exact elevation for the results is not definite.

5.2.2 Section Transformation

The method of section transformation is used for the analysis of composite members. Assuming planar sections for the SPS, the section transformation method provides an equivalent section of a homogenous material with a linear distribution from the composite SPS. A transformation ratio, *n*, calculated in equation 5.1 by comparing the steel and elastomer elasticity, E_s and E_e, adjusts the elastomer width to an equivalent width of steel. The original elastomer width is transformed to an equivalent steel width with a factor of n. Figure 5.5 illustrates a transformed section of a SPS panel. A moment of inertia for a transformed section, I_t, can be calculated.

$$n = \frac{E_s}{E_e} \qquad [5.1]$$

5.2.3 Surface Strain from Applied Load

Within the SPS elastic range and assuming a linear strain distribution, equation 5.2 is used to calculate the surface strains, ε, as a function of the applied moment. c is the distance from the neutral axis to the extreme fiber. Table 5.1 shows comparison of the measured strains to the calculated strains.

$$\varepsilon = \frac{Mc}{E_s I_t} \qquad [5.2]$$

Table 5.1 shows that equation 5.2 provides reasonable estimates of steel surface strain results, with errors less than 5%.

5.3 Shear Stress Distribution

5.3.1 Average Longitudinal Shear Stress

Because the flexural stress distribution in the transformed SPS section is essentially linear, the distribution of longitudinal shear stress of SPS members is given by equation 5.3 (Beer & Johnston, 1992). τ_{avg} is a function of the shear force, first moment of the transformed area, Q_t, moment of inertia of the transformed section, and the width of the beam, t.

$$\tau_{ave} = \frac{VQ_t}{I_t t} \qquad [5.3]$$

5.3.2 Longitudinal Shear Stress Profile

Using equation 5.3 one can estimate the average shear stress for the SPS at any specific elevations. Figure 5.6 shows the shear stress distribution of a 10-50-10 SPS member. There are two observations regarding the shear stress in the SPS panel.

The first observation is that the figure is essentially tri-linear. The stress increases linearly from zero at the steel surface to maximum at the bonding interface. Shear stress remains at a constant maximum in the elastomer layer. The tri-linear diagram is the result of a high stiffness material at the geometric extreme combined with a less stiff material in the center.

The second observation is the significant amount of shear resisted by the steel layers in the elastic range. The flanges of a typical steel wide-flange section provide minimal shear resistance because majority of the flange does not contact the web. Shear flow is restricted to the flange immediately connected to the web. As a result, majority of the flange does not contribute vertical shear stress. For a SPS section, the continuous

interface permits a direct transfer of shear from the steel layers to the elastomer. Because of the continuous bonding and a high flange thickness to section height ratio, the steel of a 10-50-10 SPS section provided 20% of the overall shear capacity.

5.3.3 Maximum Shear Stress Shape Factor

A shape factor, F_{shape}, can be used to relate the overall shear stress to the maximum average shear stress at the neutral axis. Figure 5.7 is a graphical presentation based on equation 5.3. The figure presents a range of shape factors with varying percentages of elastomer. Using equation 5.4, one can calculate the maximum average shear stress at the elastomer layer.

$$\tau_{\max} = F_{shape} \frac{V}{A} \qquad [5.4]$$

5.3.4 Interface Shear Stress

The strain values recorded by the steel surface gauges from interval and static tests can be used to calculate strain gradients. Equation 5.5 relates the strain gradients between the steel and the elastomer to the shear stress, $\tau_{interface}$, at the interface.

In equation 5.5, $\Delta\varepsilon$ is the averaged differences in surface strain at peak applied load, A_s is the cross-sectional area of one steel plate, b is the SPS width, h is the SPS total height, l is the distance between the strain gauges, and t is the thickness of the steel layer.

Figure 5.8 shows a strain vs. applied load diagram. The averaged strain differences of other geometrically similar locations increase the data confidence statistically.

$$\tau_{\text{int}erface} = \frac{\Delta\varepsilon E_s A_s}{bl}\left(\frac{h-t}{t}\right) \qquad [5.5]$$

Table 5.2 lists the strain values, calculated interface shear stress, and compares the results to equation 5.3 results. For the interval tests, the measured “High” strain values in the table are average strain values from the steel surface gauges located nearest from the

applied load. The “Low” values are from locations nearest the support. Steel strains are values at estimated at the center of the steel layer assuming a linear strain distribution. For the static tests, the high strain values are the average strain from gauge# 2 and #7 and low values are gauge# 3 and #6. The table shows good agreement between equation 5.3 and equation 5.5, suggesting that the assumed linear bending strain distribution is appropriate.

5.4 Deflection of SPS Beams

The overall deflection, δ, of an SPS panel is the summation of two components, a flexure deflection, δ_m, and a shear deflection, δ_v.

5.4.1 Flexural Deflection

Flexural deflection is a function of the moment of inertia of the cross-section. In the case of SPS, the transformed moment of inertia depends primarily on the geometry of the steel plates. The contribution of the elastomer is insignificant. Consequently, the amount of flexural deflection of a SPS beam is depended on steel properties. Table 3.3 lists the ancillary test results for the steel.

5.4.2 Shear Deflection

For a typical steel wide flange section, with web to flange ratio of approximately 1:15, shear deflection is relatively insignificant compare to flexural deflection. The transformed section of an SPS beam is similar to that of a wide flange except the ratio of the web to the flange of the transformed section is approximately 1:300. As a result, shear deflections are significant to the overall deflection of an SPS section. The material properties and geometry of the elastomer control shear deformations.

5.5 Deflection Models

5.5.1 Energy Method

5.5.1.1 Point Load

Using the energy method, for a beam with a point load at mid-span, total deflection is calculated by equation 5.6. Equation 5.6 is intended for a homogeneous prismatic beam. Equation 5.7 is a modified version of equation 5.6 for use with SPS beams. The flexural deformations are based on the transformed section properties. The shearing deformations are controlled by the shearing stress and strain in the elastomer.

$$\delta = \delta_m + \delta_v = \frac{PL^3}{6EI} + \frac{\alpha PL}{2GA} \qquad [5.6]$$

$$\delta = \frac{PL^3}{6E_s I_t} + \frac{PLQ_t}{2GI_t b} = \frac{PL^3}{6E_s I_t} + \alpha \frac{PL}{2G_e A_g} \qquad [5.7]$$

Where $\alpha = \frac{Q_t A_g}{bI_t}$

5.5.1.2 Uniformly Distributed Load

The energy method can also estimate the mid-point deflections from a uniform distributed load (UDL) using equation 5.8. Although UDL is not part of the current test setup, UDL load case is presented because it is one of the typical load cases for design purposes. Similar to the case of a point load, flexural deflections are based on steel layers properties and the shear deflections are based on elastomer properties.

$$\delta = \delta_m + \delta_v = \frac{5wL^4}{384E_s I_t} + \alpha \frac{wL}{8G_e A_g} \qquad [5.8]$$

5.5.2 Coupled Shear Wall Method (CSW)

5.5.2.1 Point Load

A Sandwich Plate System (SPS) beam can be modeled as a coupled shear wall. Using equation 5.9, derived in Sec. 2.4.2.3, one can estimate the SPS mid-span deflection under a point load. Figure 5.9 shows the various values of the adjustment factor F_3 depending on beam geometry.

$$y = \frac{VL^3}{3E_s I} F_3 \qquad [5.9]$$

5.5.2.2 Uniformly Distributed Load

The CSW method can be used to estimate mid-span deflections of SPS loaded under UDL. Equation 5.10 estimates deflection at mid-span of a simply supported SPS panel with uniform distributed load. Similar to point load deflection, UDL deflection calculations require adjustment factors. The factor, $F_{3,w}$, is a function of the material properties and member geometry. Figure 5.10 shows the estimate values of $F_{3,w}$.

$$y = \frac{wL^4}{24E_s I} F_{3,w} \qquad [5.10]$$

5.6 Shear Modulus of Elastomer

The shear modulus of the elastomer is observed to be load rate dependent. Fast loading rates during testing will result in higher shear modulus values. An appropriate shear modulus from a spectrum of values is needed for analysis. The value of shear modulus chosen for analysis should be reasonably compatible to the loading conditions.

The ancillary tests in section 3 provide estimates of the shear modulus. The shear modulus can be estimated from experimental results of the static, interval, and dynamic tests.

The two deflection models (energy and CSW) are used to estimate the G values of the SPS specimens from the interval and dynamic results. Comparing the G values from ancillary tests and analytical G values from the experimental data gives some indication as to the validity of the deflection models.

5.6.1 Static Test Results

Under pure shear and plane stress at the elastomer surface, the diagonal strain gauges (#17 to #20 of figure 3.15) will record the principal strains, $\varepsilon_{principal}$, at the elastomer surface. From equation 5.11 (Ugural & Fenster, 1995) one can estimate the shear modulus (G) from the static test results.

Figure 5.11 shows shear stress vs. principal strain diagram for the two static tests. The slopes of graph at the elastic range, estimated by strains less than 6000 με, are proportional to the estimated G. G gradually decline as τ increases, which is a sign of softening of the beam at higher stresses. B1 has a significantly higher G when compared to A6.

$$G = \frac{\tau}{2\varepsilon_{principal}} \qquad [5.11]$$

5.6.2 Interval Test Data

Table 5.3 shows the shear modulus estimates from the interval tests using the energy and CSW model. The recorded member deflection is related to the shear modulus estimated by each deflection model. Each estimate of the shear modulus is an averaged modulus from the several tests. The table shows that CSW model consistently estimated the shear modulus at about 75% of the energy model. The shear modulus estimated by the CSW model is closer to the results obtained by ancillary tests.

5.6.3 Dynamic Test Data

Table 5.3 shows estimates of shear modulus from the dynamic test results by the energy and CSW model. The ranges of deflection and load were used for the estimations. An averaged shear modulus value based on the dynamic cycles was presented. The CSW model again resulted in lower estimates of the shear modulus.

5.6.4 Shear Modulus Comparison

Table 5.3 lists the estimated shear moduli for each specimen from the ancillary and experiment results. Figure 5.12 shows the data with respect to estimated shear stress rates. There are several observations made from table 5.3 and figure 5.12.

First, the elastomer tension and torsion tests show that the elastomer of both specimen sets have similar shear modulus. Second, a higher load rate produced a higher shear modulus. Third, from the interval and dynamic experimental results, shear moduli estimated for set B are higher than those estimated for set A. Fourth, the energy deflection model estimates higher shear modulus (33%) than the CSW model.

Because the elastomer shear moduli are similar for both specimen sets, the variations of G within the experimental data are depended on factors other than the elastomer material properties.

5.7 Deflection Models

Both deflection models produced estimates of shear modulus that are higher than those obtained from ancillary tests. Although the CSW model provided shear modulus results that are more consistent with ancillary test results, the energy method is the preferred method for deflection calculations based on several practical factors.

First, the energy model has simpler equations to implement compare to CSW. Second, the energy model explicitly separates the two deflection components, allowing flexibility for adjustments to material and geometrical properties. Third, the model can be

arranged so that shear deflection is calculated as a ratio of the flexural deflection. Fourth, the energy model will predict larger deflections given any shear modulus, which is more conservative if maximum deflection is a design criterion. Lastly, as the shear modulus estimated by the two models differs by a consistent ratio of 75%, a factor can be added to the energy model to adjust for the differences.

5.7.1 Span-Depth Ratio

Figure 5.13 shows a diagram of the flexural deflection as a percentage of the total deflection vs. span-depth ratio for a point load or a uniformly distributed load using the energy model. The figure shows that the percentage of flexural deflection for a point load changes with shear modulus. The effect of changing the shear modulus for a uniformly distributed load is insignificant and is not shown in the figure. As expected, a higher G value and longer spans would reduce the proportion of shear of the total deflection.

The figure shows that the total deflection for low span-depth ratio SPS members consisted large percentages of shear. The significance of the shear component reduces as the span ratio increases. At higher span ratios, the shear component is negligible.

The current tests have a span-depth ratio of 20 and shear modulus of 400 MPa. From the figure, the estimated shear component should account for 45% of the total deflection, in reasonable agreement with experimental results.

5.8 Fatigue Data Analysis

5.8.1 Stress Range vs. Stress Intensity

One objective of the test program is to determine the dominant contributing factor for the fatigue of the SPS. Unfortunately, the test results are inconclusive whether stress range or mean stress affects the SPS interface fatigue properties with the current results because of the varying failure modes observed.

Set A specimens failed at the steel-elastomer interface and set B specimens failed in the steel plates with cracks propagating through the elastomer layer. The static test specimens (A6 and B1) failed by yielding of steel layer rather than shear failures at the interface. Because of the failure modes, only results from set A can be used to address whether stress range or mean stress affects interface fatigue. However, the mean stress and the stress range for set A specimens are roughly proportional to each other. Therefore, stress range and mean stress effects cannot be readily differentiated.

5.8.2 Dynamic vs. Interval

Another objective for the experiment is to simplify the fatigue test program. One simplification would be to dispense with the interval tests and obtain all experimental data from the dynamic component only.

Table 5.4 shows the strain amplitudes recorded by steel surface gauges. “Low” values are average amplitudes recorded by strain gauges furthest away from the applied load (gauge #1, #6, #7, and #12 in Fig. 3.12). “High” values are the average strain amplitudes recorded by strain gauges located near the applied load (gauge #3, #4, #9, and #10 of Fig. 3.12). The recorded strain amplitudes between the two test phases should be similar because the applied load ranges, strain gauge locations, and strain gauges used for the two tests phases are identical.

Table 5.4 shows strain values in the dynamic test phase have lower strain amplitudes than in the interval test phase. Section 5.2.3 shows that the interval test strain results are compatible to the recorded applied load. Therefore, the discrepancy is from the errors of the dynamic test. The strain circuitry did not respond fast enough to provide accurate strain data.

5.8.3 Specimen Set Comparisons

All set A specimens failed in fatigue at the interface. In contrast, none of the set B specimens failed at the interface. This suggests differences of material properties or the

interface conditions between the two sets affected the failure modes and the fatigue lives of the specimens.

5.8.3.1 Steel

Table 3.3 shows that set A specimens have lower steel yield strength than set B specimens (350 MPa vs. 450 MPa). With higher strength steel, set B specimens are steel fatigue critical and set A specimens, with lower strength steel, are interface fatigue critical. Because steel was not tested for fatigue properties, it is inconclusive whether the steel strength affected the steel fatigue.

5.8.3.2 Elastomer

The ancillary test results shown in table 5.3 indicate that the elastomer of the two specimen sets have similar shear modulus. Although the yield stress of the elastomer of set B is higher than those in set A, there is no immediate conclusion regarding the fatigue property is affected by the yield stress.

5.8.3.3 Interface

Table 3.8 shows that the interface roughness of set B is higher than set A specimens. The higher roughness may have enhanced the shear stress capacity of the interface, as shown by the torsion test data.

The torsion tests show that fatigue loading did not reduce the interface shear strength or the shear modulus of SPS beams. Consequently, the torsion test results can effectively compare shear strength of the two sets of specimens. Specimens from set A have a lower interface shear capacity than set B specimens.

5.8.3.4 Comparison Conclusions

The ancillary tests show that the steel moduli of elasticity and elastomer moduli of rigidity between the two specimen sets are similar. As a result, the flexural stiffness between the two specimen sets should also be similar. However, from analytical estimations of shear modulus of the experimental data, set B specimens have higher shear modulus compared to set A specimens. The different shear modulus values observed is attributed to the interface properties.

A comparison of the failure modes and shear strengths of the interface for the two specimen sets suggests that the SPS interface fatigue properties are closely related to the interface properties. The difference in shear capacity and roughness can be indications to the fatigue life of the specimens.

5.8.4 SPS Failure Indicators

During fatigue testing, there are subtle indications for approaching failures. The indications are changes in member response or unusual instrument recordings. The observed indicators can serve as a warning of impending failure for future laboratory testing or used as structural maintenance tool.

5.8.4.1 Stiffness Results of Dynamic Test

Stiffness, defined as load amplitude divided by mid-span deflection amplitude, is a measure of the SPS member response. The changing of the stiffness compare to the initial stiffness defines the “Relative stiffness”. Figure 5.14 to 5.23 show the relative stiffness fluctuation of the SPS specimens over the course of the dynamic tests. The results show steady flexural stiffness throughout the early stages of the test with significant stiffness changes before failure. Most SPS members failed after the member stiffness had reduced to between 85% and 90% of the initial stiffness.

5.8.4.2 Stiffness Results of Interval Test

Table 5.5 lists the stiffness fluctuations for interval tests. Figure 5.24 and 5.25 show the relative stiffness vs. cycles diagrams. Although the interval stiffness tends to decrease prior to failure, it is too infrequent to be a reliable indicator of impending failure.

5.8.4.3 Dynamic Strain

Figure 5.26 and 5.27 are samples of steel strain amplitude vs. cycles diagrams. Figure 5.26 shows typical trend of strain amplitudes for specimens with interface failures. Figure 5.27 shows the fluctuation of strain amplitudes for specimens with steel fatigue failures.

For specimens with interface failures, the steel strain amplitudes begin to fluctuate significantly from previous levels when failure approaches. The fluctuation of surface strain for specimens with interface failure is attributed to the gradual delaminating of the bonding interface. The specimen redistributes the applied load within the body to compensate for lost interface contact area. In the process, strain gauges register changes in strain amplitudes.

For steel fatigue failures, the fluctuations in strain amplitude are insignificant prior to failure. The response of the steel plates is uniform throughout the test with no sign of strain amplitude deviations. Continually monitoring dynamic strain amplitudes provided no warning of fatigue failures of the steel plate.

5.8.4.4 Creep

Creep is the gradual increase of deflection of a member caused by sustained applied loads. For the fatigue tests, instead of sustained static loads, constant load ranges were applied. A realistic load intensity to use for creep analysis is the mean load because it is representative of the load range experienced by the specimen.

Equation 5.12 defines the amount of creep for the tests. δ_i is the total deflection at a given cycle under the average load. δ_0 is the initial elastic deflection of the member under the average load. δ_{creep} is the additional deflection with increase cycles. The ϕ factor is a creep coefficient. Figure 5.28 to 5.37 show diagrams of ϕ vs. cycle for the fatigue tests. Table 5.6 lists the ϕ at failure for the specimens.

$$\delta_i = \delta_0 + \delta_{creep} = \delta_0(1+\phi) \qquad [5.12]$$

The creep coefficient prior to member failures ranges from 30% to 200%. Most specimens failed with creep at 50%. As a result of the scatter observed, creep might not be an ideal indicator for failure. However, creep deflection might be of importance for deflection calculations with sustained loads.

Table 5.1: Comparison of recorded and calculated strain with applied load.

Gauge Location	Applied Load (kN)	Calculated Strain	Recorded Strain	Relative Error
Tensile A1	75.18	663.7	634.5	4.6%
Tensile A2	54.47	478.0	462.4	3.4%
Tensile A3	45.06	386.3	374.3	3.2%
Tensile A4	40.79	349.7	348.2	0.4%
Tensile A5	40.87	354.5	346.0	2.4%
Compressive A1	75.18	-663.7	-629.6	5.4%
Compressive A2	54.47	-478.0	-459.5	4.0%
Compressive A3	45.06	-386.3	-375.7	2.8%
Compressive A4	40.79	-349.7	-352.1	-0.7%
Compressive A5	40.87	-354.5	-341.1	3.9%

Table 5.2: Shear stress comparison.

Specimen		**A1**	**A2**	**A3**	**A4**	**A5**	**A6**	**B1**	**B2**	**B3**	**B4**	**B5**	**B6**
Load Amplitude	**kN**	70.2	50.0	40.4	35.6	36.0	38.6	53.3	42.1	60.0	58.6	91.0	80.3
Surface High strain (measured)	με	708	528	414	372	373	-584	-236	517	743	789	1009	908
Surface Low Strain (measured)	με	449	329	267	236	237	479	525	253	356	389	494	424
Steel High Strain (estimated)	με	604	450	354	317	319	-498	-201	433	624	663	861	771
Steel Low Strain (estimate)	με	383	280	228	202	202	409	449	212	299	326	421	360
Strain Difference	με	221	170	125	116	116	-908	651	221	324	336	440	411
Shear Stress	**MPa**	2.94	2.26	1.67	1.54	1.55	6.06	4.34	1.97	2.88	2.99	3.91	3.65
VQ/IT Shear Stress	**MPa**	3.01	2.14	1.70	1.50	1.53	6.04	4.22	2.00	2.85	2.76	3.89	3.50
Percent Error	**%**	2.3	-5.6	1.8	-2.6	-1.3	-0.5	-3.0	1.6	-1.3	-7.7	-0.3	-4.3

Table 5.3: Shear modulus results comparison.

G (MPa)		A1	A2	A3	A4	A5	A6
Interval Data	Energy	301.3	299.1	322.5	285.6	317.3	NA
	CSW	227.9	228.7	247.4	218.3	243.5	NA
CSW/Energy		76%	76%	77%	76%	77%	NA
Dynamic Data	Energy	383.6	371.5	440.3	428.9	413.9	NA
	CSW	297.1	286.0	341.8	332.6	320.1	NA
CSW/Energy		77%	77%	78%	78%	77%	NA
Torsion Test		NA	NA	136.0	142.4	NA	NA
Elastomer Tension		186.6	186.6	186.6	186.6	186.6	186.6
Static Test		NA	NA	NA	NA	NA	211.4

G (MPa)		B1	B2	B3	B4	B5	B6
Interval Data	Energy	NA	449.6	408.8	449.8	488.1	483.5
	CSW	NA	337.3	306.8	338.2	378.8	372.6
CSW/Energy		NA	75%	75%	75%	78%	77%
Dynamic Data	Energy	NA	543.6	494.5	566.7	573.7	617.9
	CSW	NA	410.9	373.4	422.8	447.2	479.0
CSW/Energy		NA	76%	76%	75%	78%	78%
Torsion Test		124.6	155.9	158.7	147.4	145.8	123.8
Elastomer Tension		183.6	183.6	183.6	183.6	183.6	183.6
Static Test		337.3	NA	NA	NA	NA	NA

Table 5.4: Comparison of dynamic and interval strain data.

	Dynamic (με)		Interval (με)		Dynamic as % of Interval	
	High	Low	High	Low	%	%
A1	256	119	708	449	36%	26%
A2	376	236	528	329	71%	72%
A3	181	116	414	267	44%	43%
A4	167	107	372	236	45%	45%
A5	169	107	373	237	45%	45%

Table 5.5: Relative fluctuation of member stiffness recorded by interval tests.

Cycles	A1	A2	A3	A4	A5	B2	B3	B4	B5	B6
1	100%	100%	100%	100%	100%	100%	100%	100%	100%	100%
10	100%	100%	100%	100%	100%	100%	100%	100%	100%	100%
100	101%	101%	99%	101%	100%	100%	100%	101%	100%	100%
1,000	98%	101%	100%	101%	100%	99%	102%	99%	100%	100%
10,000	99%	102%	101%	101%	100%	99%	102%	98%	100%	101%
100,000	0%	98%	98%	95%	99%	99%	100%	99%	99%	100%
250,000		99%	97%	92%	99%	99%	99%	99%	98%	100%
500,000		0%	96%	85%	97%	99%	102%	98%	99%	100%
750,000			94%	0%	30%	100%	101%	99%	102%	99%
1,000,000			94%		0%	101%	102%	99%	0%	100%
1,250,000			96%			98%	104%	101%		101%
1,500,000			94%			98%	103%	100%		101%
1,750,000			80%			98%	103%	100%		100%
2,000,000			33%			97%	101%	99%		100%
2,250,000			0%			99%	102%	99%		101%
2,500,000						97%	99%	99%		101%
2,750,000						99%	99%	99%		100%
3,000,000						0%	96%	100%		100%
3,250,000							99%	85%		101%
3,500,000							99%	0%		101%
3,750,000							99%			100%
4,000,000							101%			99%
4,250,000							100%			101%
4,500,000							100%			100%
4,750,000							101%			99%
5,000,000							101%			99%
5,250,000							98%			100%
5,500,000							99%			100%
5,750,000							99%			99%
6,000,000							98%			100%
6,250,000							98%			100%
6,500,000							99%			100%
6,750,000							101%			100%
7,000,000							99%			99%
7,250,000							100%			98%
7,500,000							101%			99%
7,750,000							100%			99%
8,000,000							101%			99%
8,250,000							101%			100%
8,500,000							100%			100%
8,750,000							100%			100%
9,000,000							99%			100%
9,250,000							101%			100%
9,500,000							100%			100%
9,750,000							101%			100%
10,000,000							101%			99%

Table 5.6: Creep coefficient at end of fatigue test.

Specimen	A1	A2	A3	A4	A5
Final creep	27%	45%	93%	39%	62%

Specimen	B2	B3	B4	B5	B6
Final creep	36%	47%	203%	26%	39%

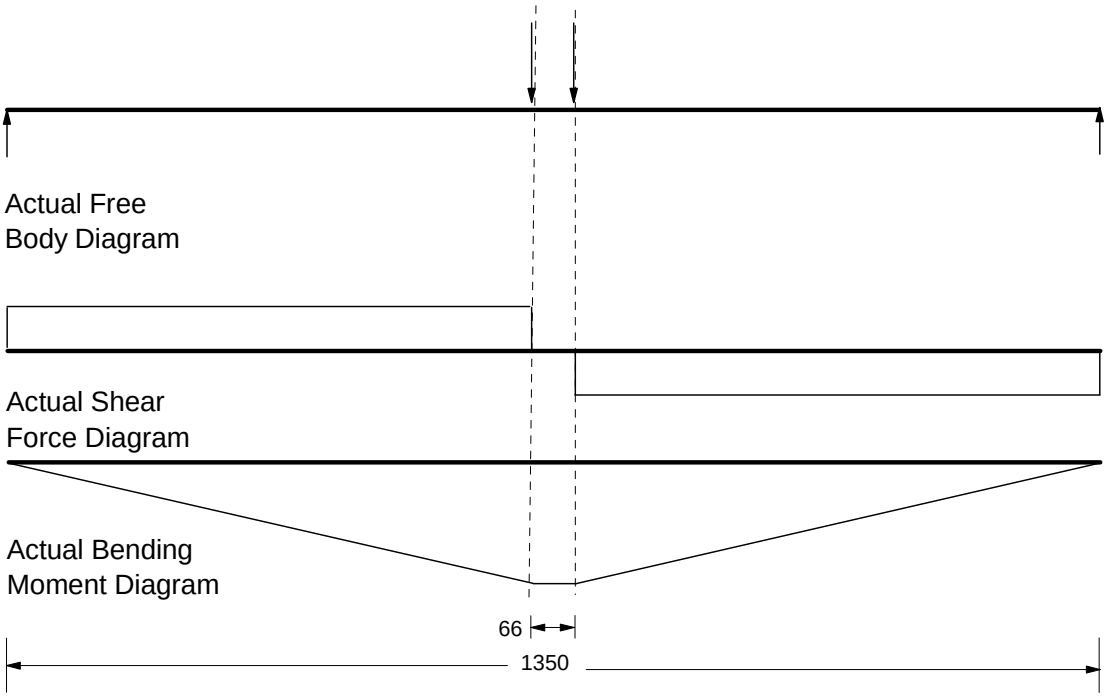

Figure 5.1: BFD, SFD, and BMD for fatigue tests with boundary effects.

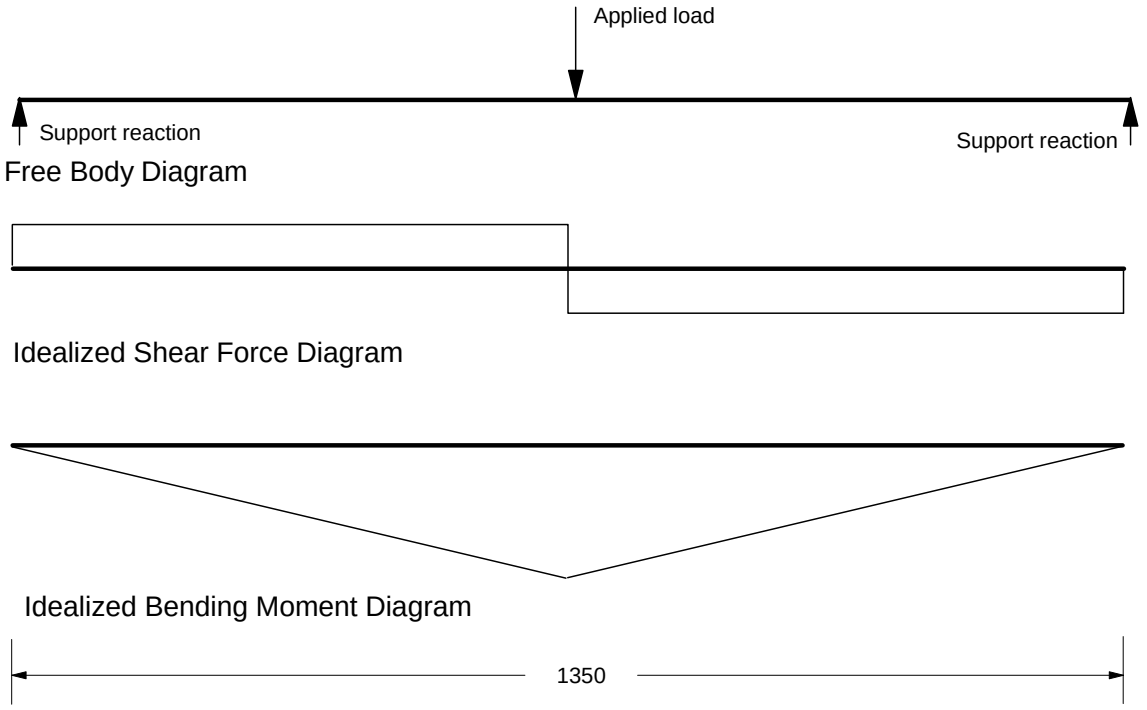

Figure 5.2: Idealized FBD, SFD, and BMD for the fatigue tests.

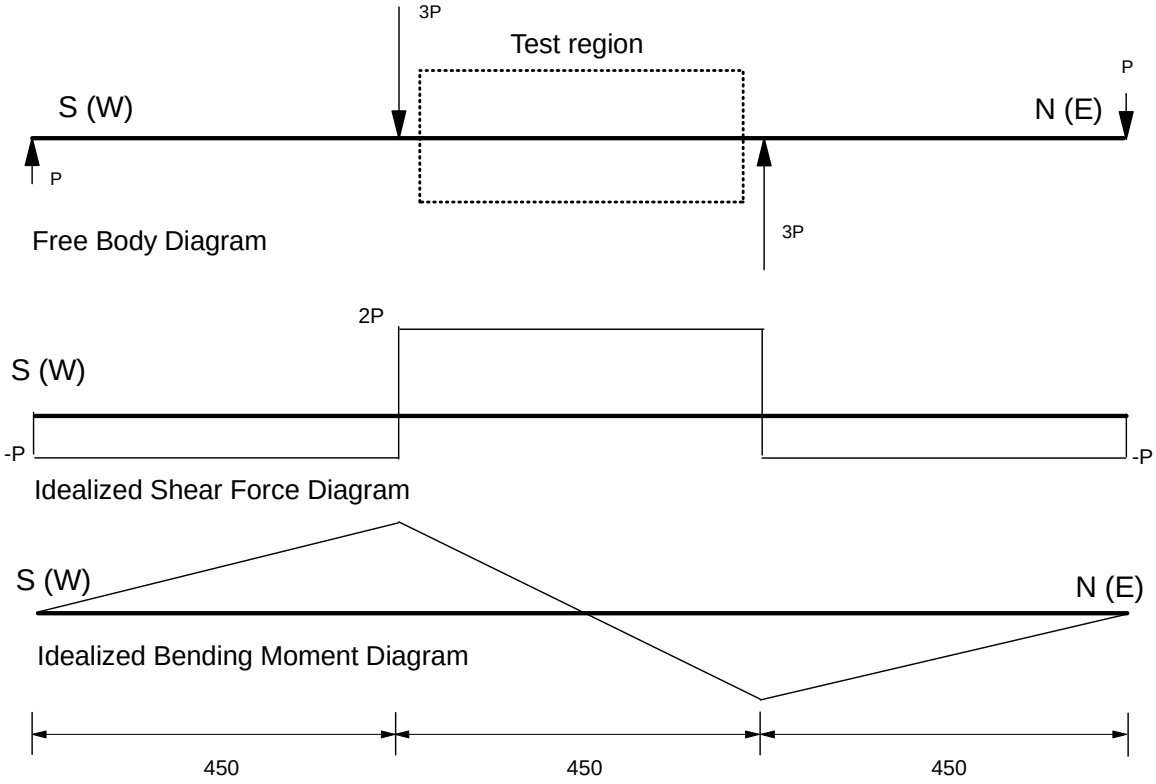

Figure 5.3: Idealized FBD, SFD, and BMD for static test.

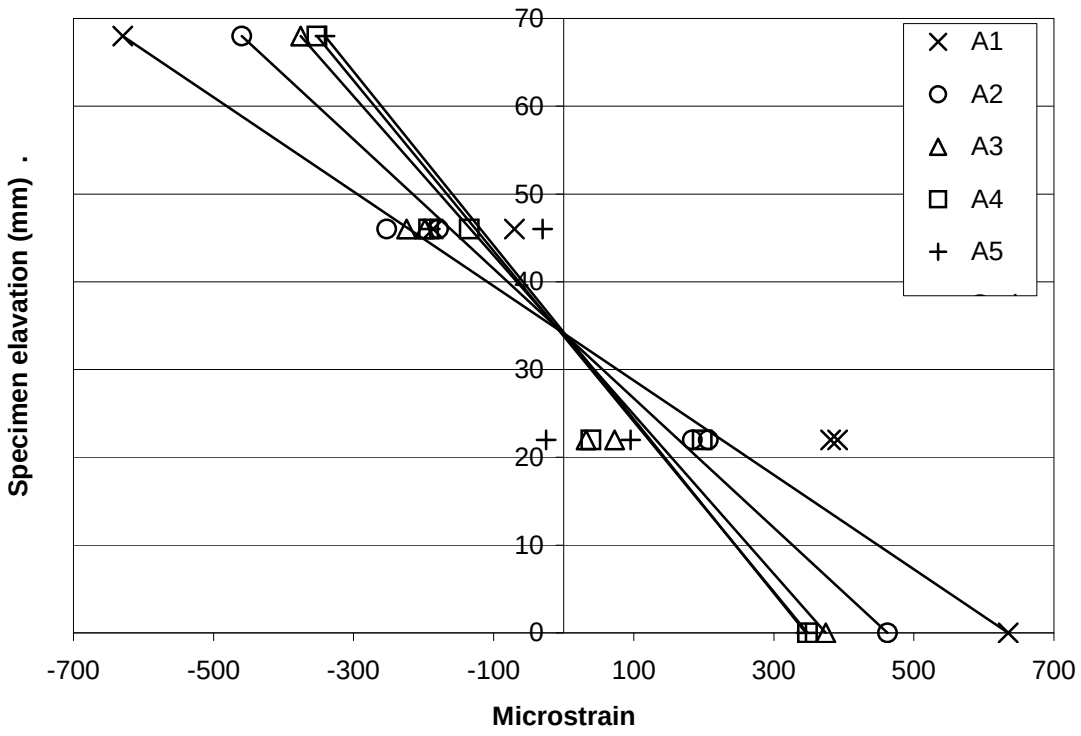

Figure 5.4: Linear strain distribution compared with actual recorded strain data.

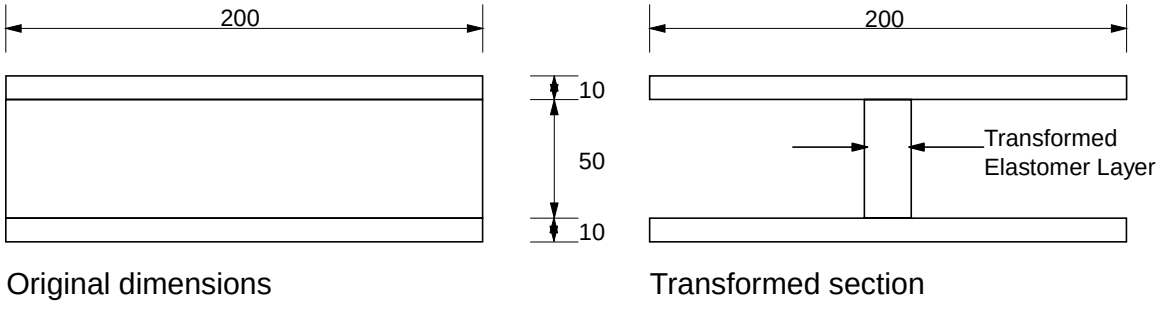

Figure 5.5: Elastomer transformed to steel properties.

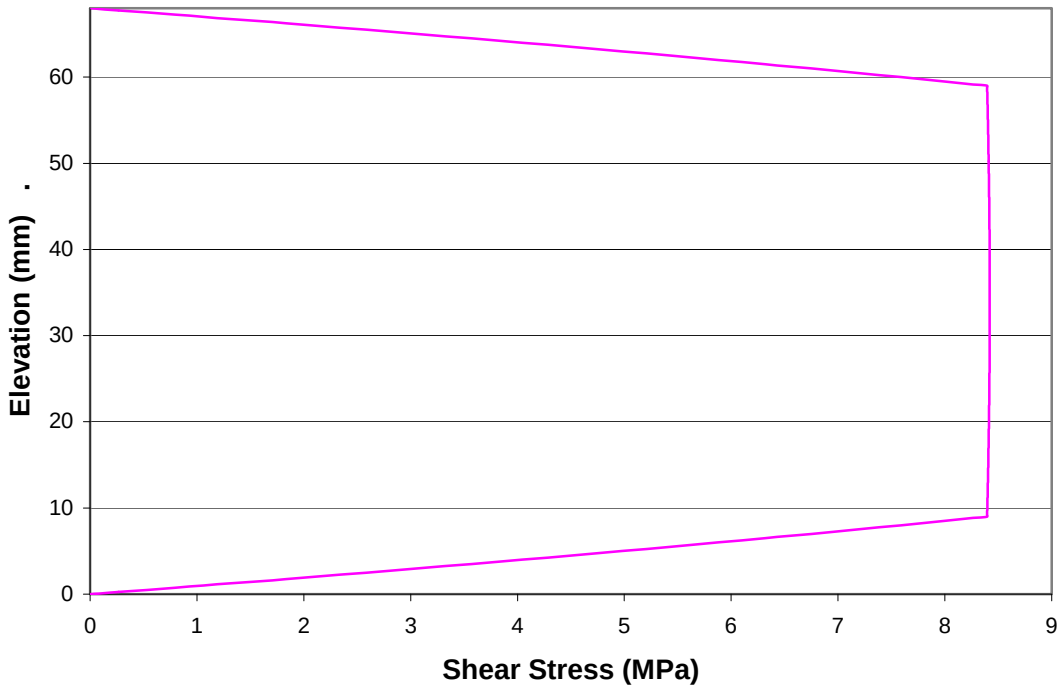

Figure 5.6: Theoretical shear stress distribution vs. SPS elevation.

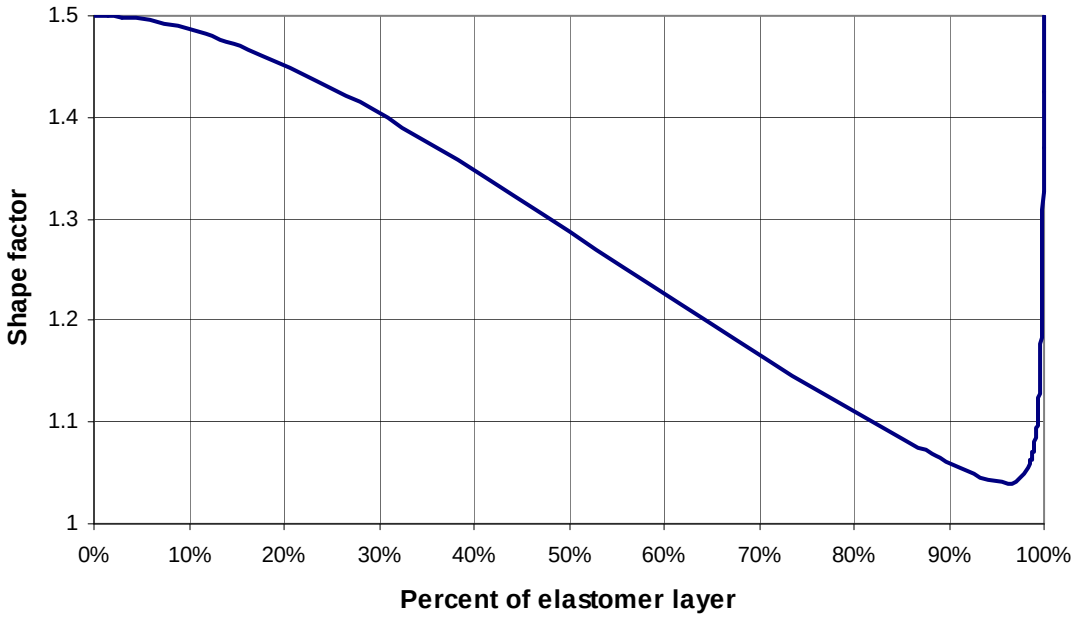

Figure 5.7: Shape factor for 10-50-10 SPS.

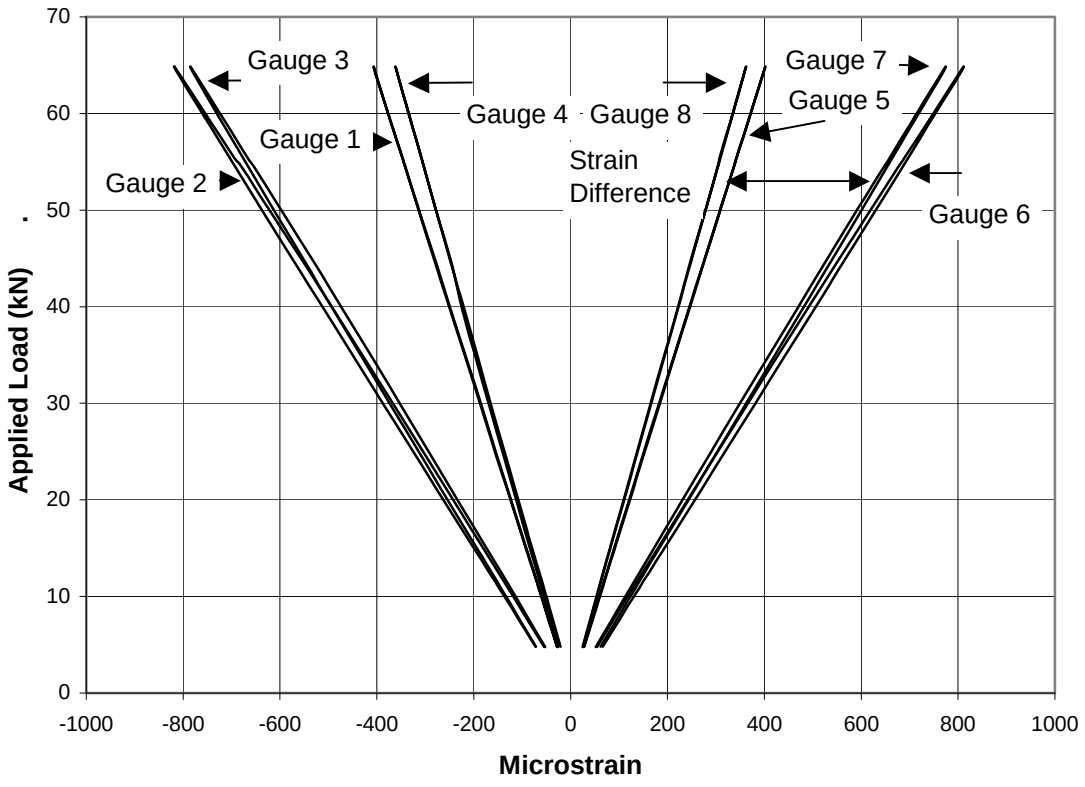

Figure 5.8: Sample steel surface strain vs. applied load diagram. (B3a data shown)

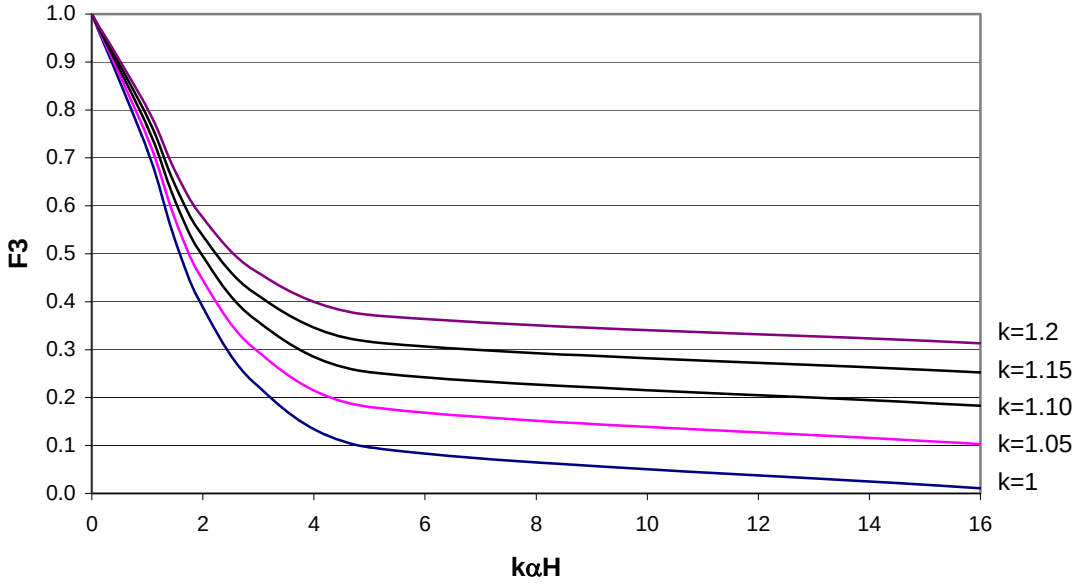

Figure 5.9: F3 factor for mid-span deflection from a mid-span point load.

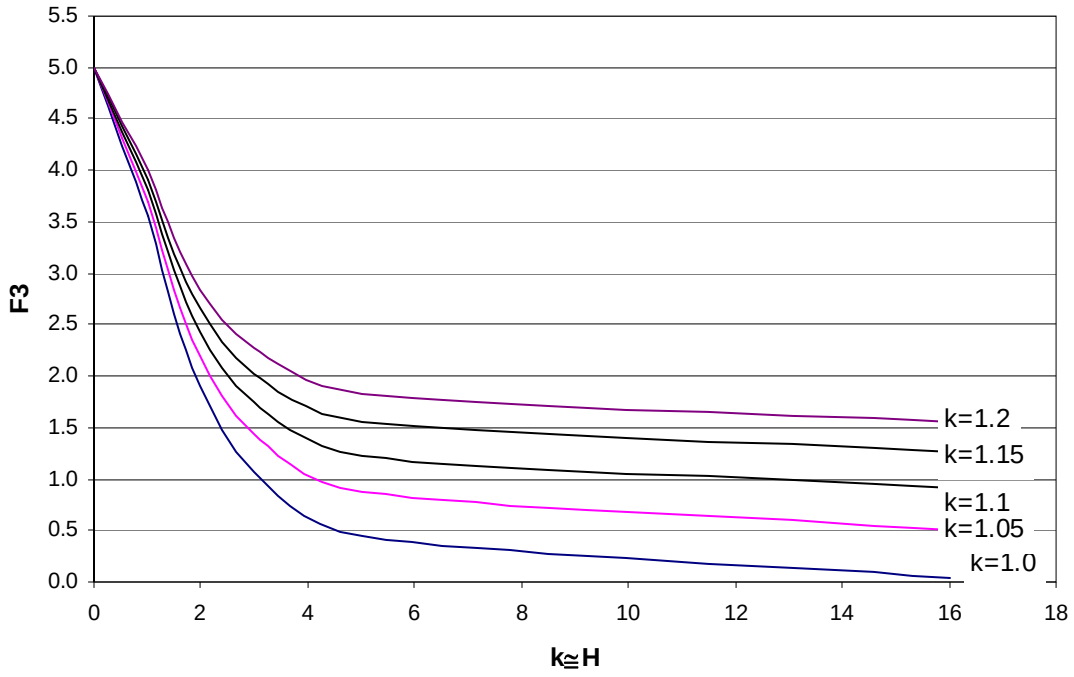

Figure 5.10: F3,w factor for mid-span deflection from a uniform distributed load.

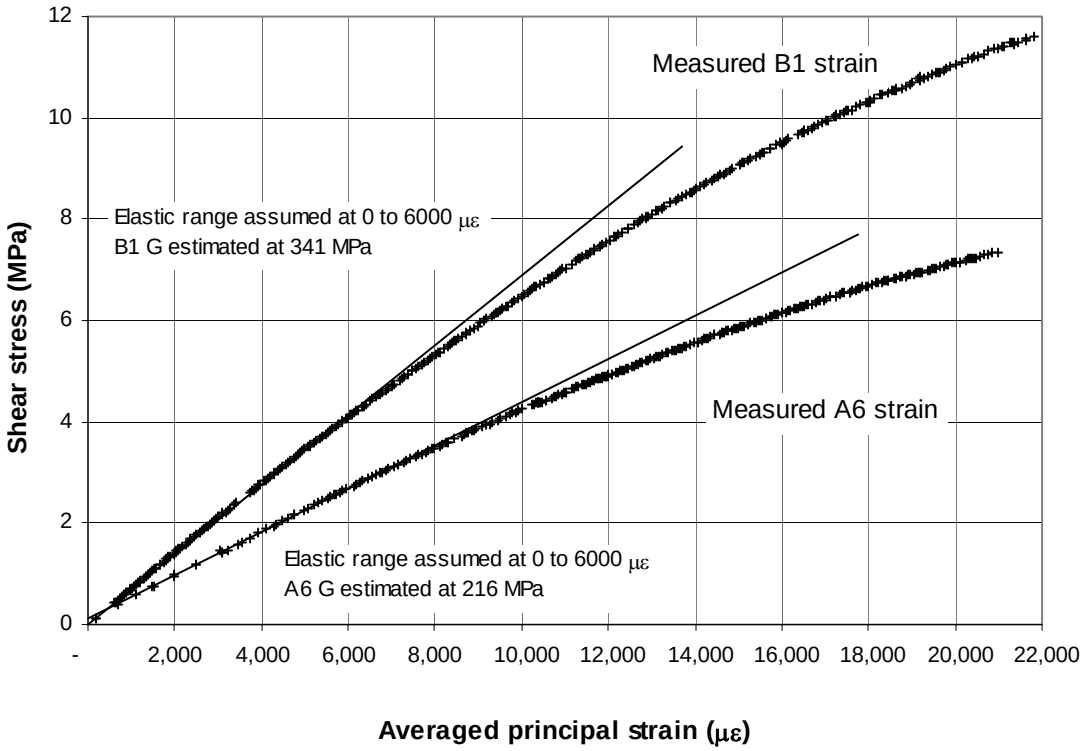

Figure 5.11: Shear modulus estimation from static data.

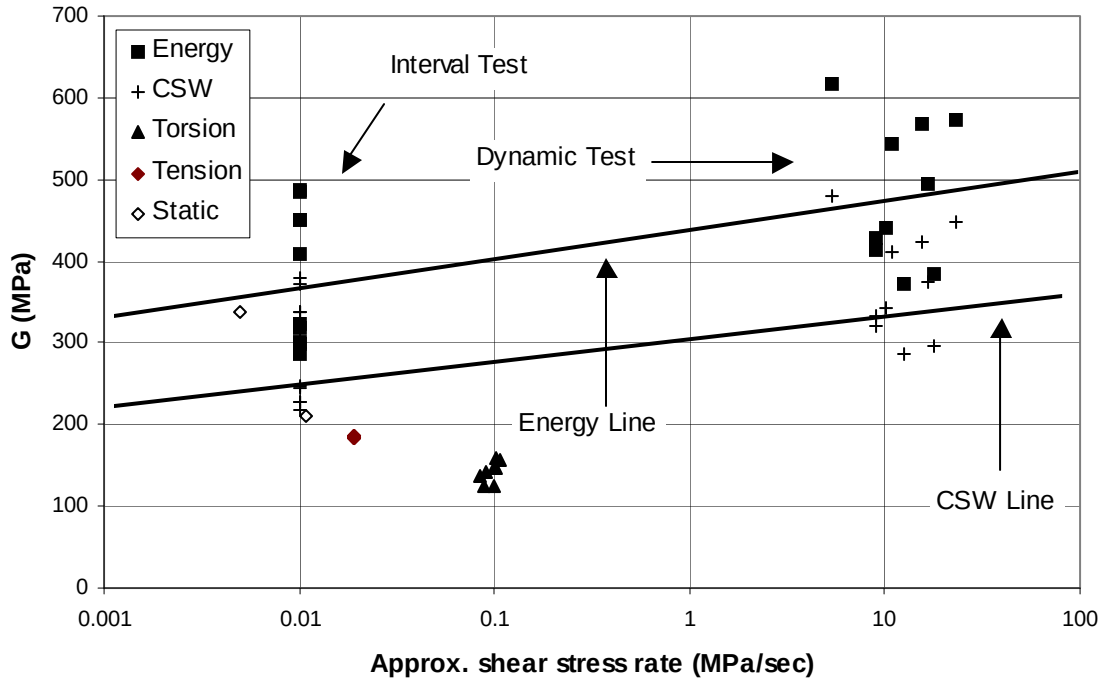

Figure 5.12: Approximate loading rate vs. shear modulus.

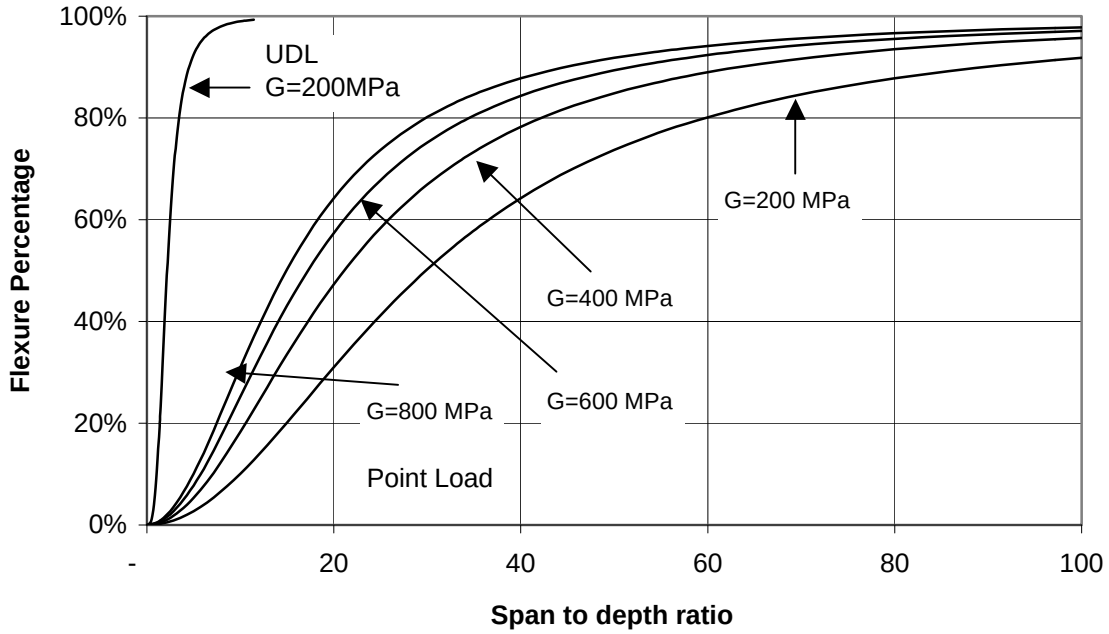

Figure 5.13: Flexural deflection percentage vs. span-depth ratio.

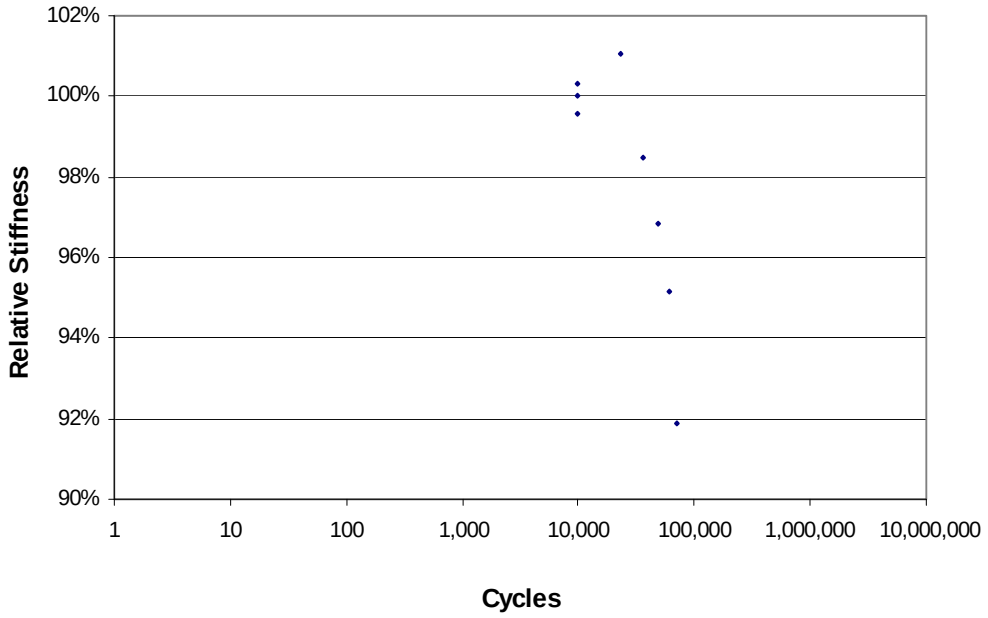

Figure 5.14: Dynamic member stiffness of A1 (Interface failure).

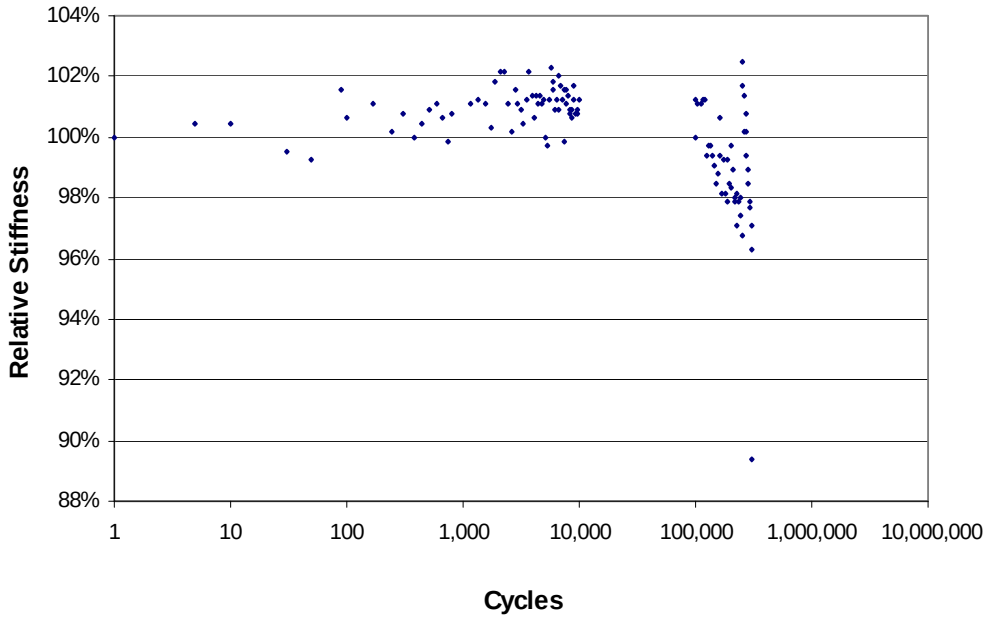

Figure 5.15: Dynamic member stiffness of A2 (Interface failure).

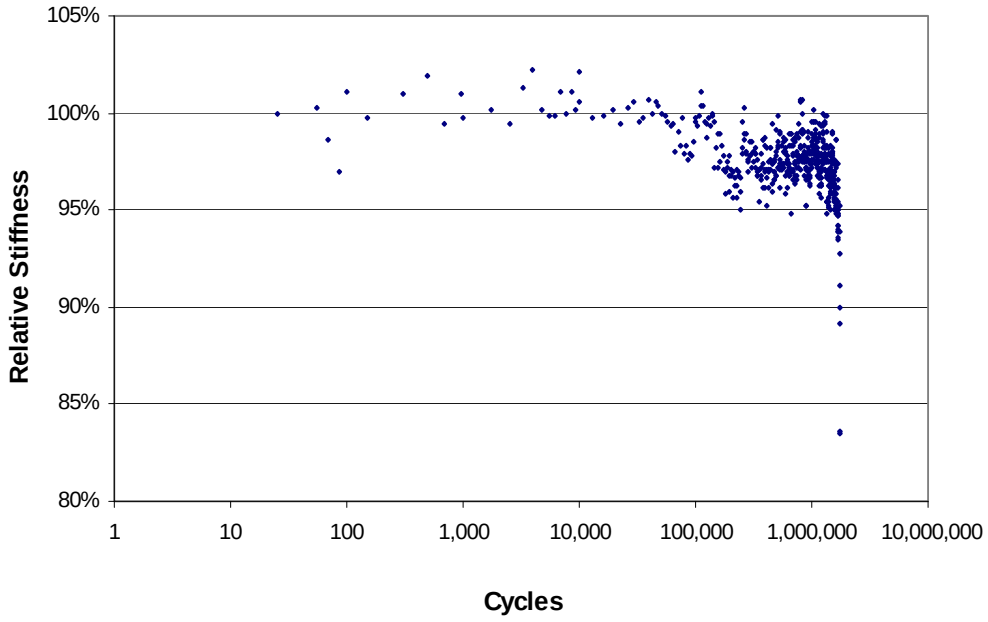

Figure 5.16: Dynamic member stiffness of A3 (Interface failure).

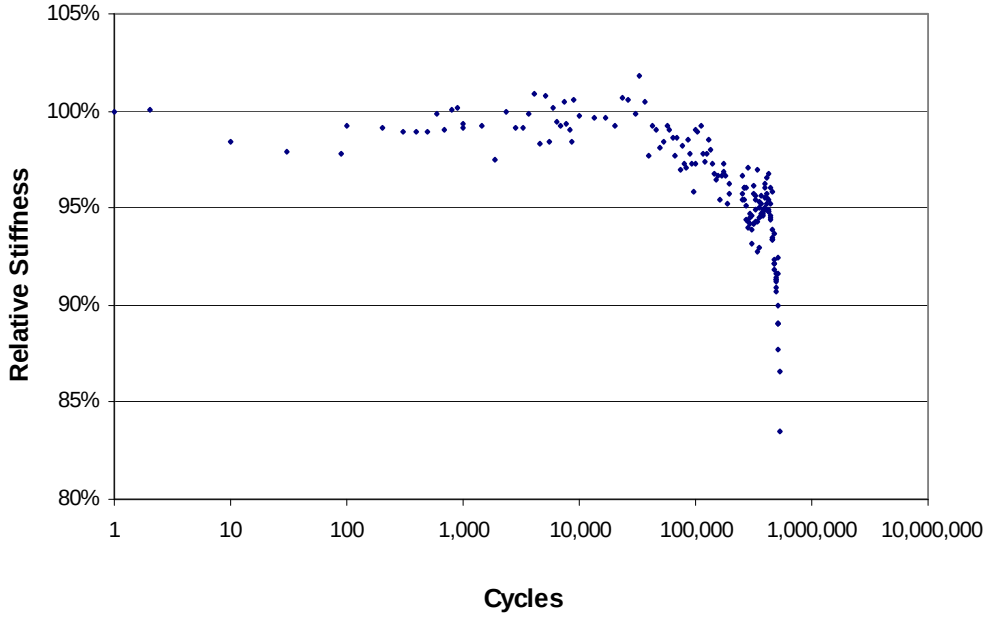

Figure 5.17: Dynamic member stiffness of A4 (Interface failure).

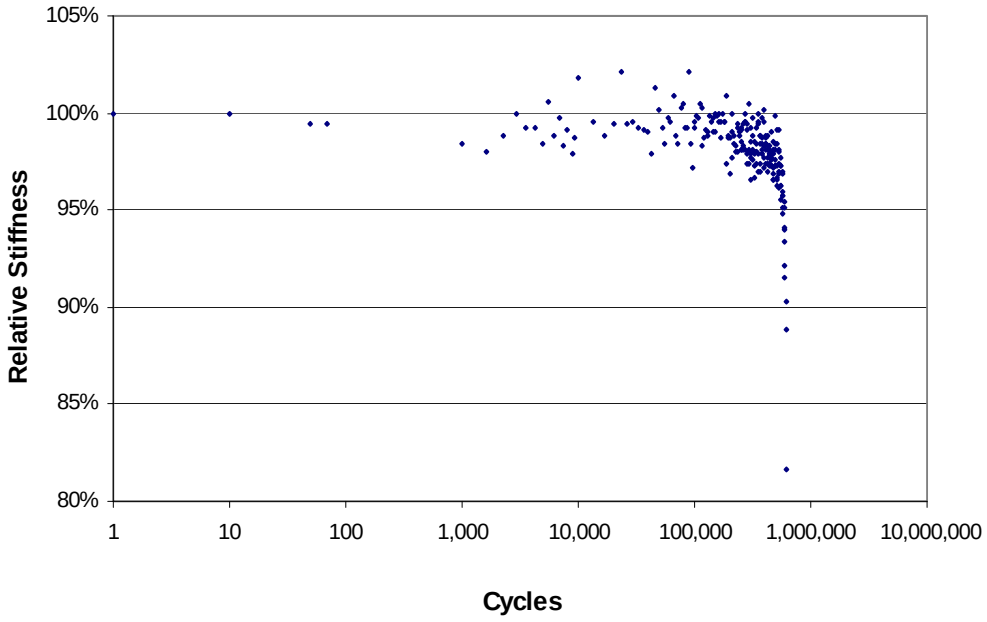

Figure 5.18: Dynamic member stiffness of A5 (Interface failure).

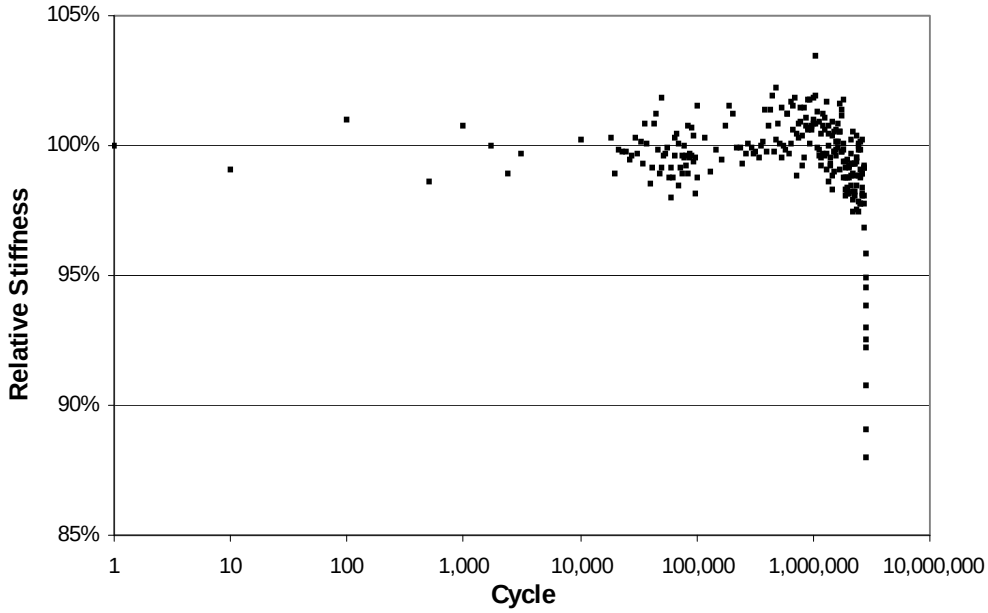

Figure 5.19: Dynamic member stiffness of B2 (Steel failure).

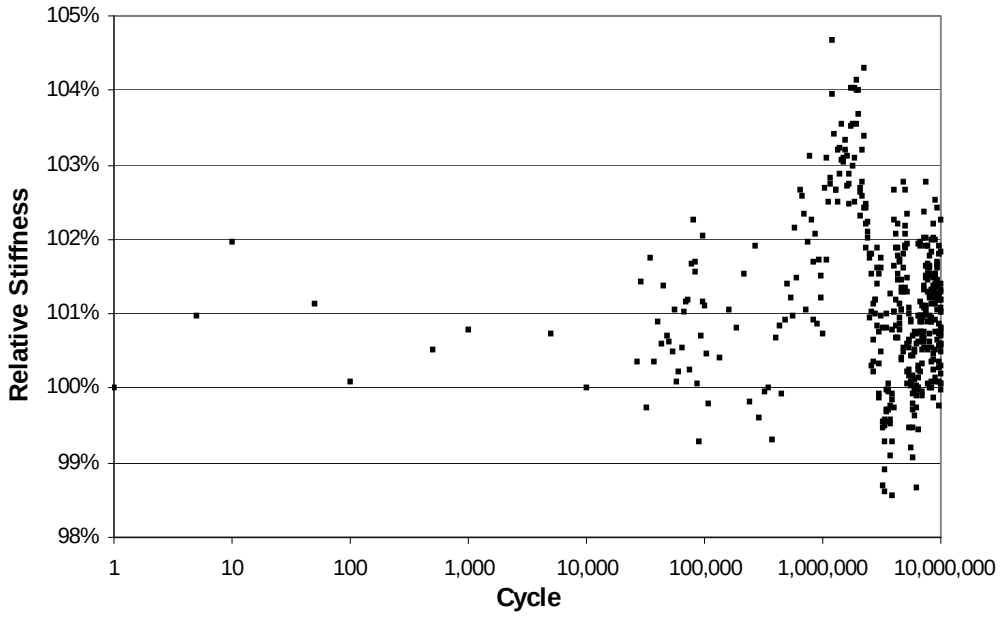

Figure 5.20: Dynamic member stiffness of B3 (No failure after 10 million cycles).

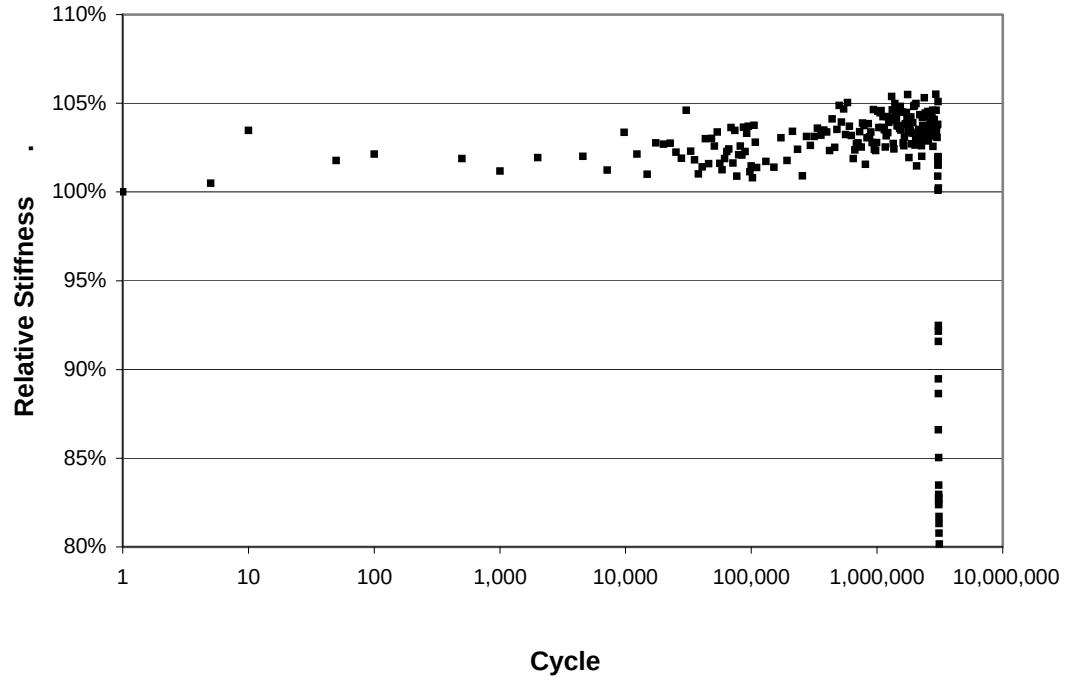

Figure 5.21: Dynamic member stiffness of B4 (Steel failure).

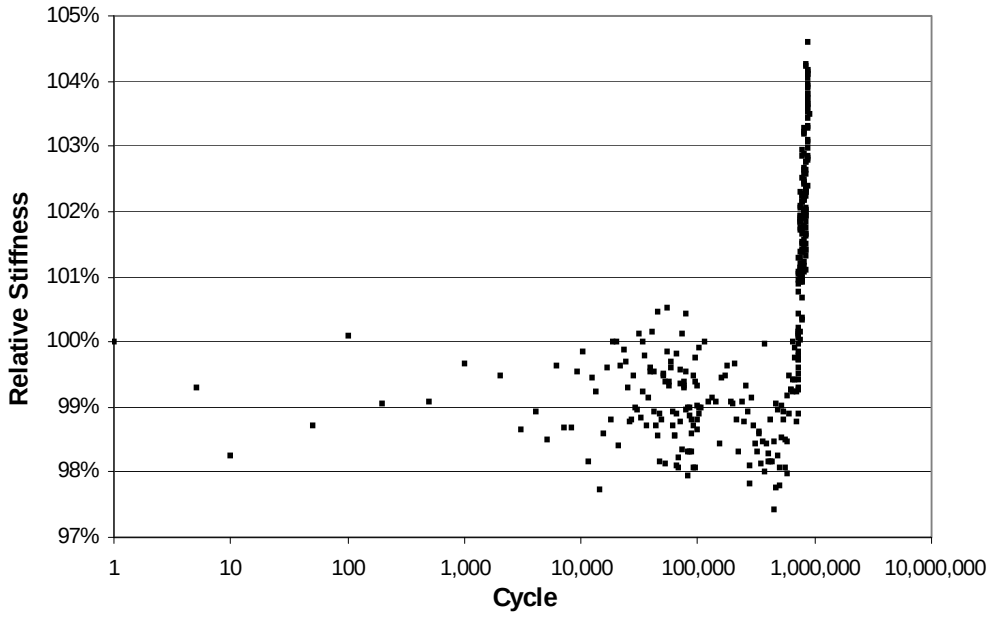

Figure 5.22: Dynamic member stiffness of B5 (Steel failure).

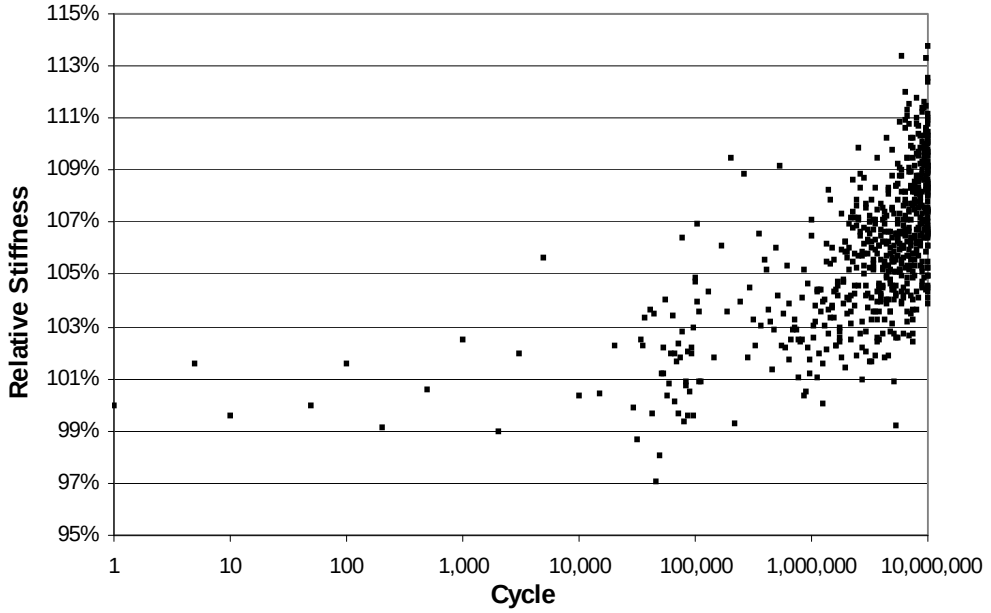

Figure 5.23: Dynamic member stiffness of B6 (No failure after 10 million cycles).

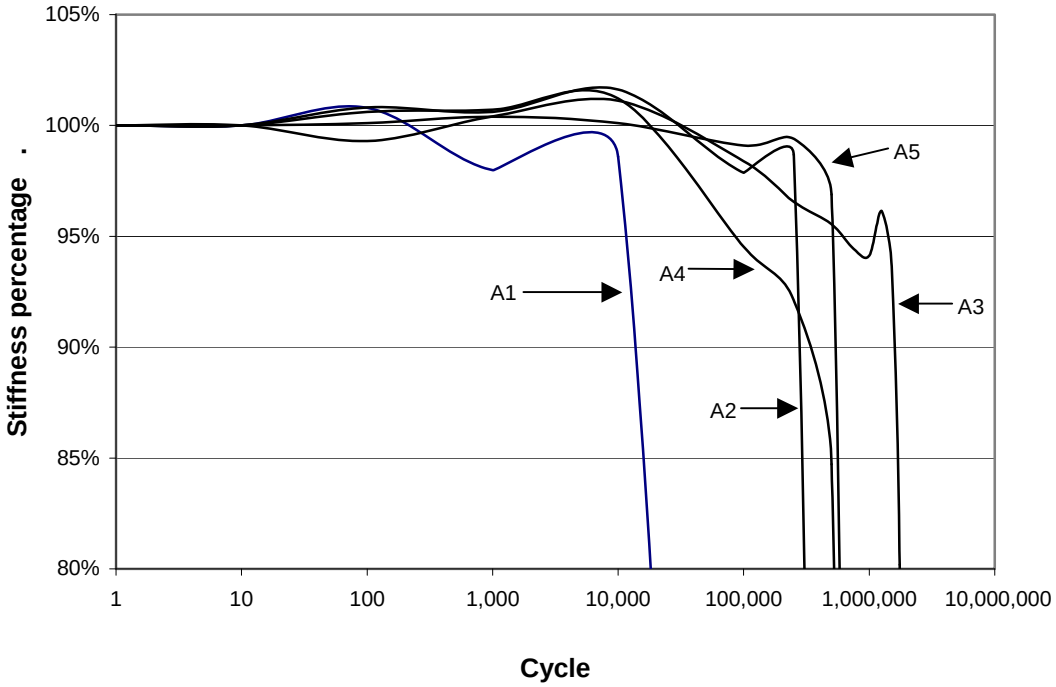

Figure 5.24: Fluctuation of stiffness for Set A specimens.

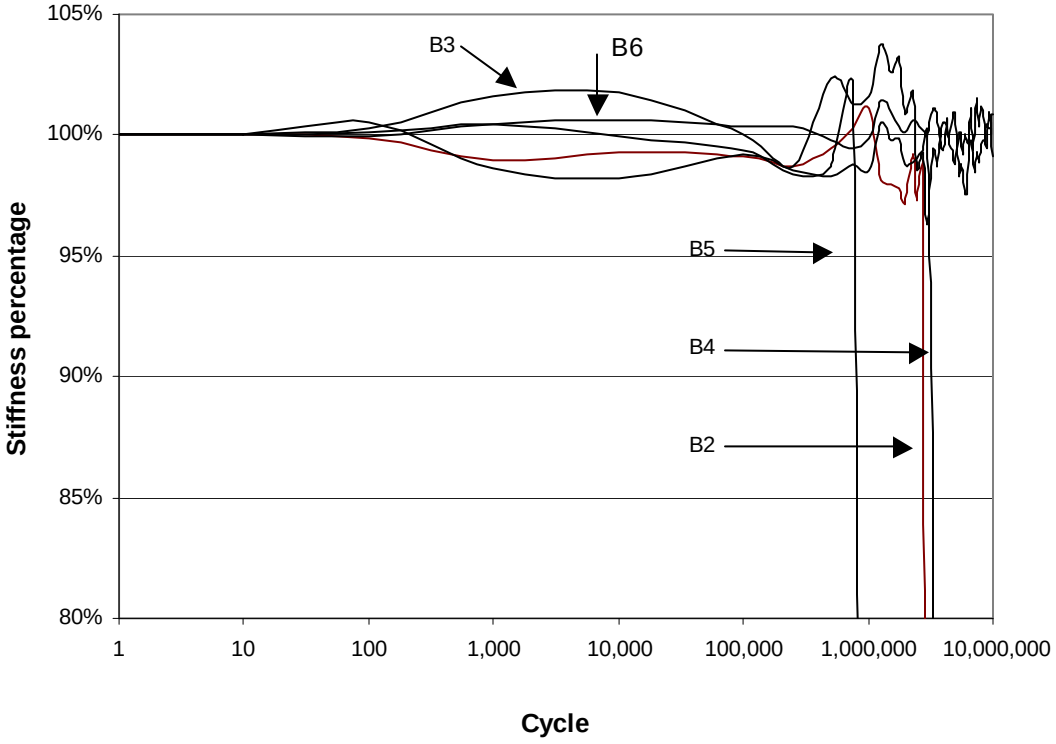

Figure 5.25: Fluctuation of stiffness for Set B specimens.

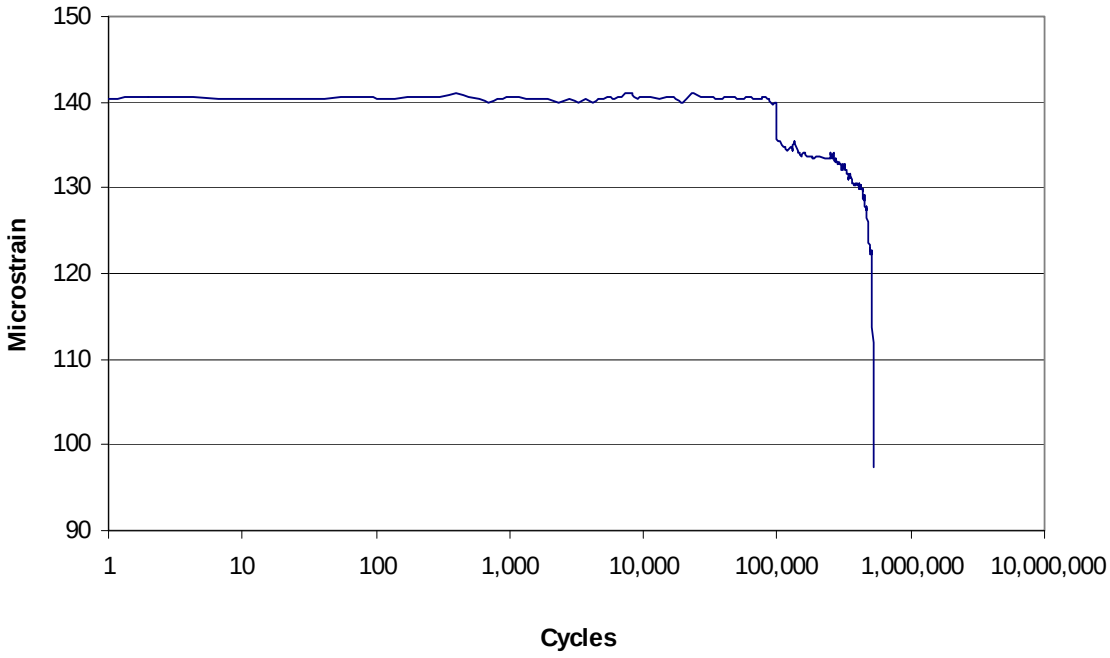

Figure 5.26: Dynamic strain amplitudes. (A4 gauge #2 shown)

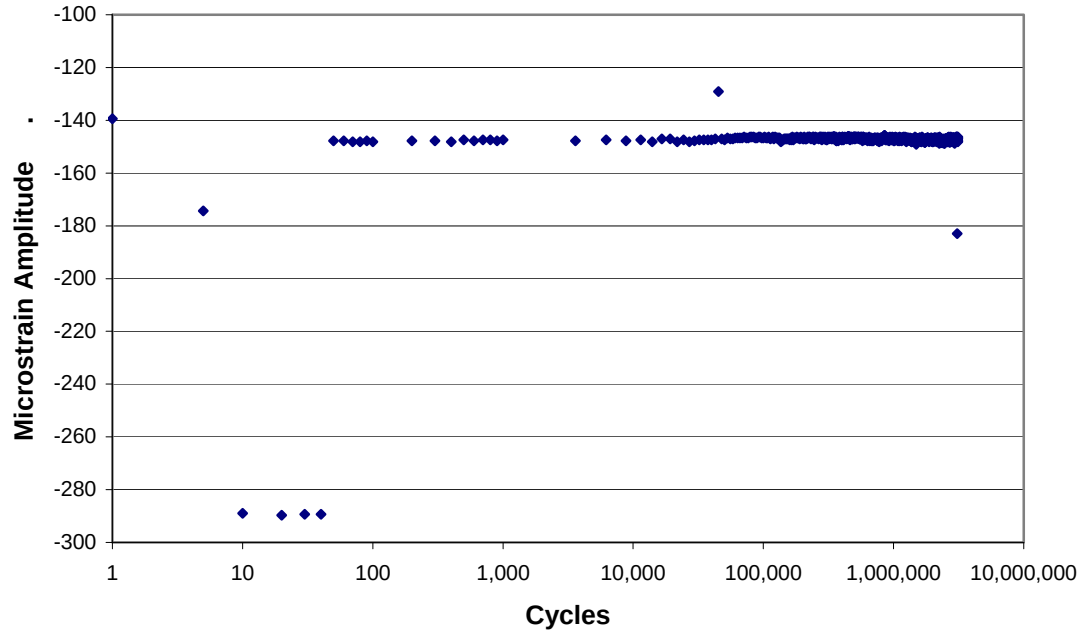

Figure 5.27: Dynamic strain amplitudes. (B4 gauge #8 shown)

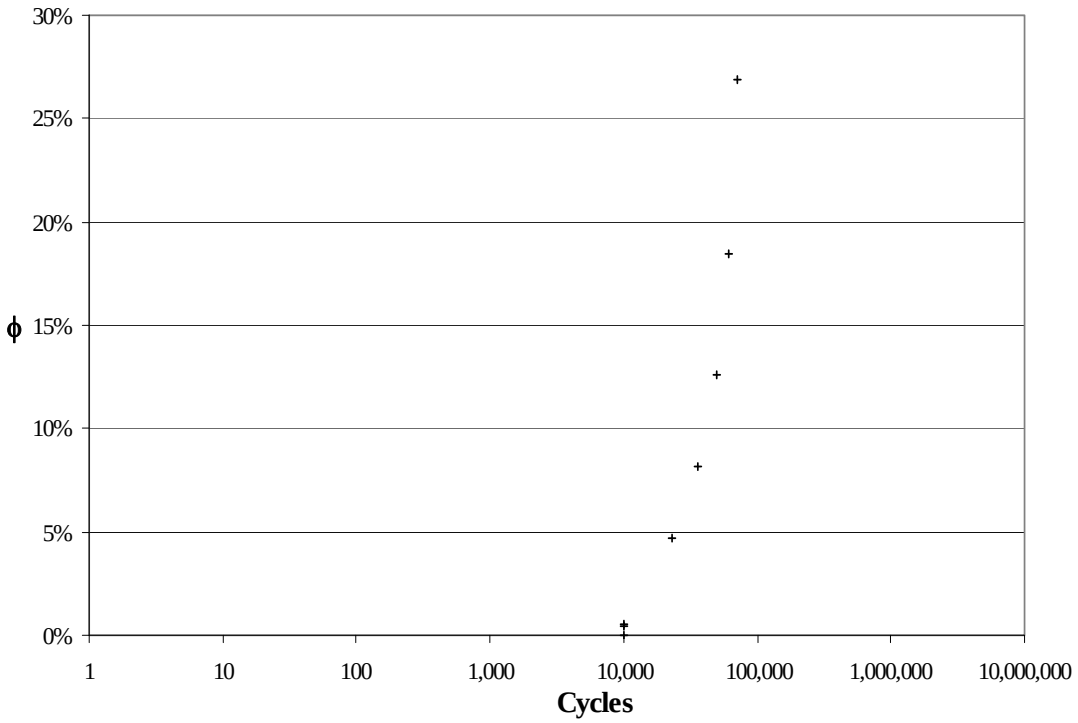

Figure 5.28:Creep coefficient variation vs. cycles of load for A1.

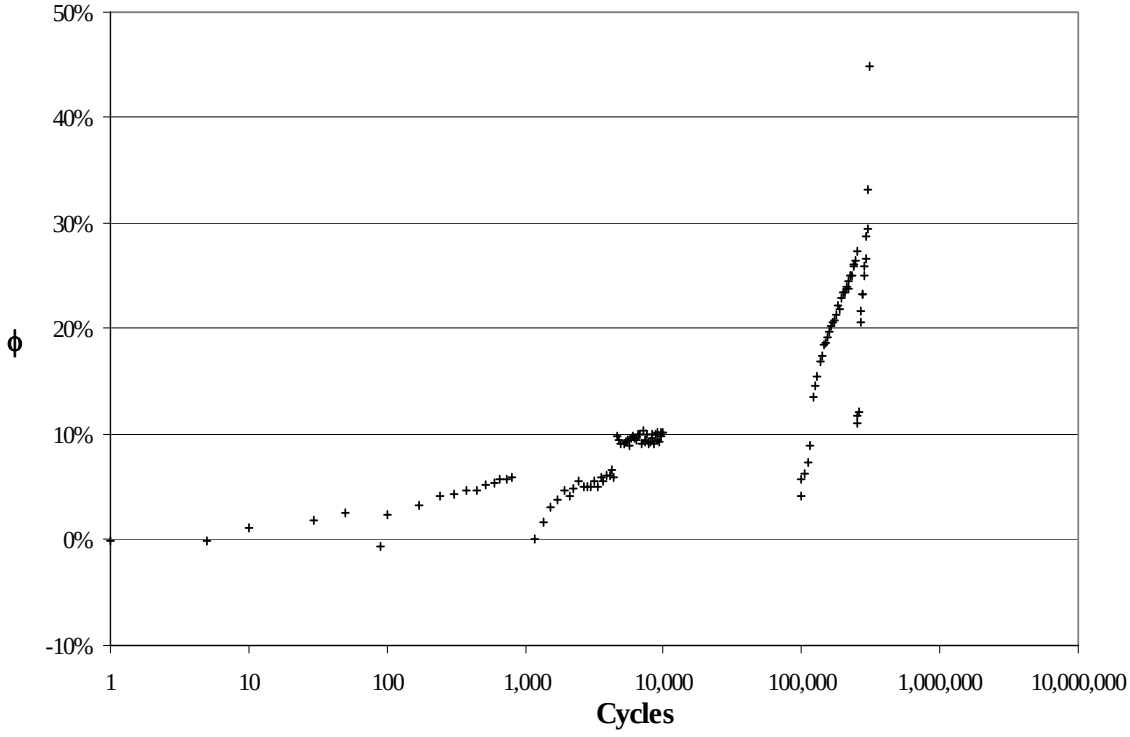

Figure 5.29: Creep coefficient variation vs. cycles of load for A2.

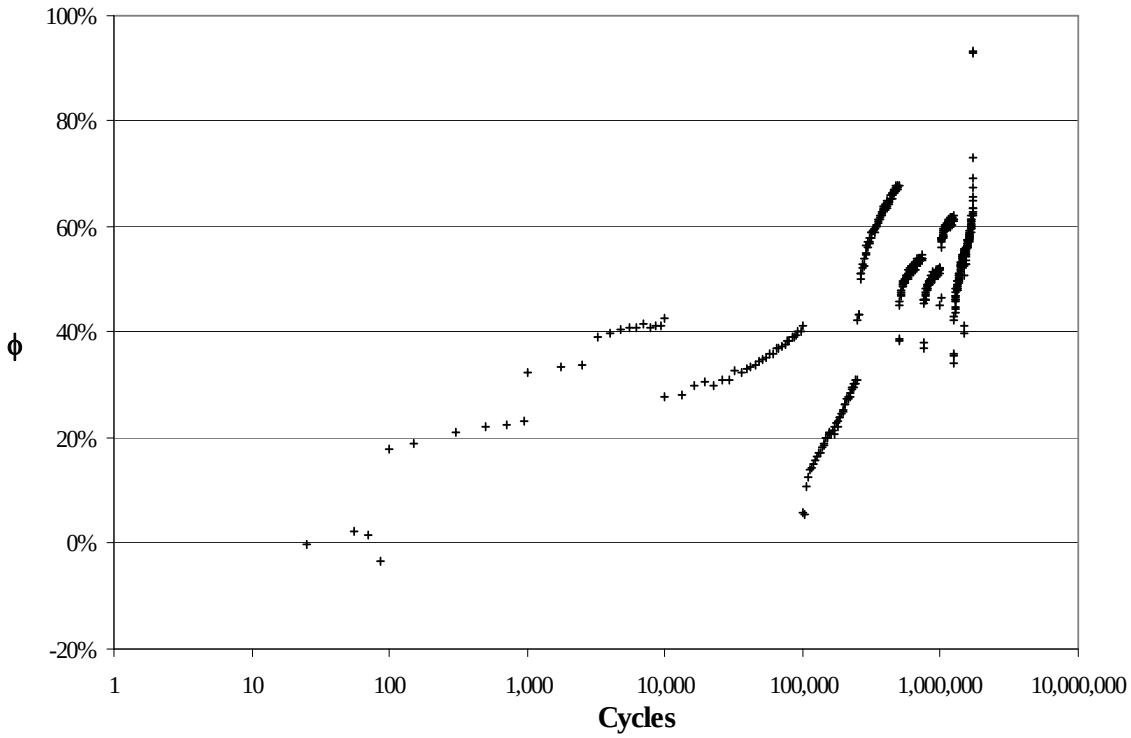

Figure 5.30: Creep coefficient variation vs. cycles of load for A3.

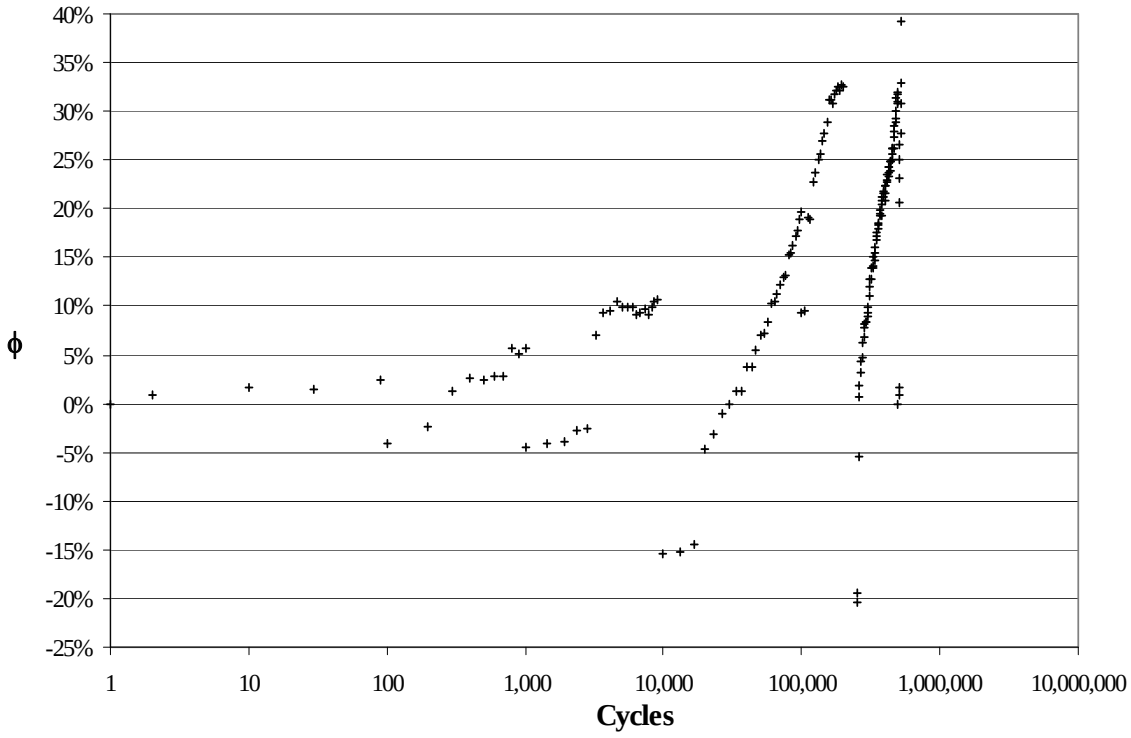

Figure 5.31: Creep coefficient variation vs. cycles of load for A4.

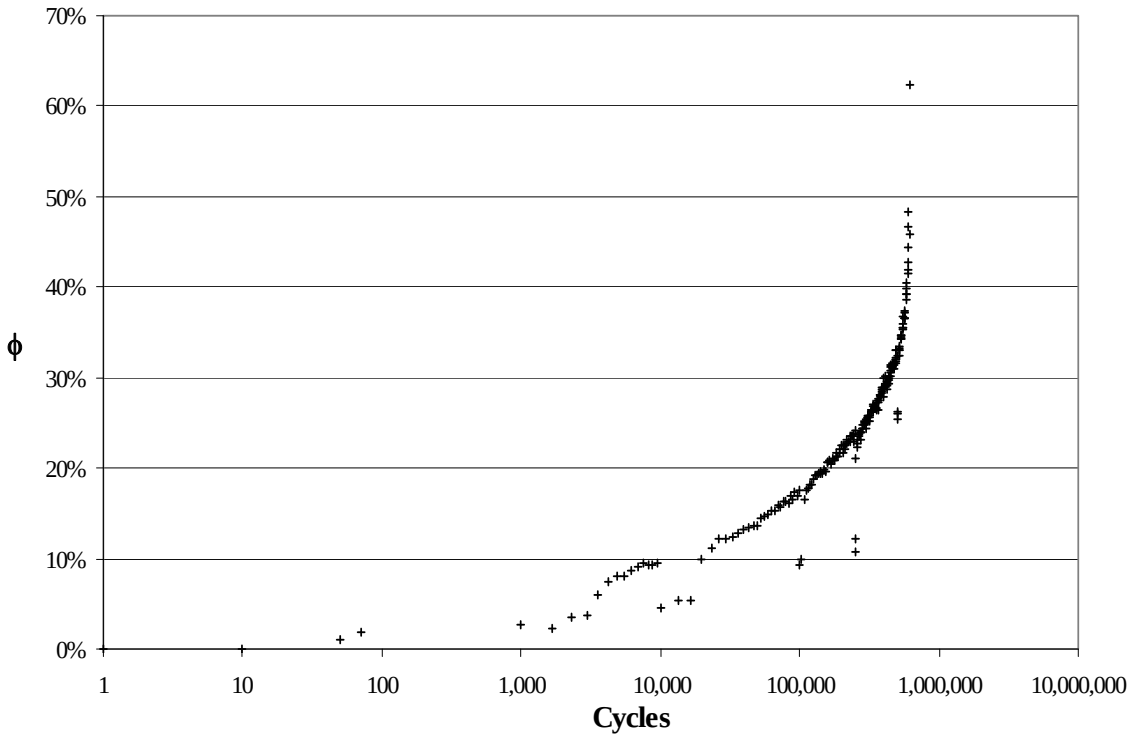

Figure 5.32: Creep coefficient variation vs. cycles of load for A5.

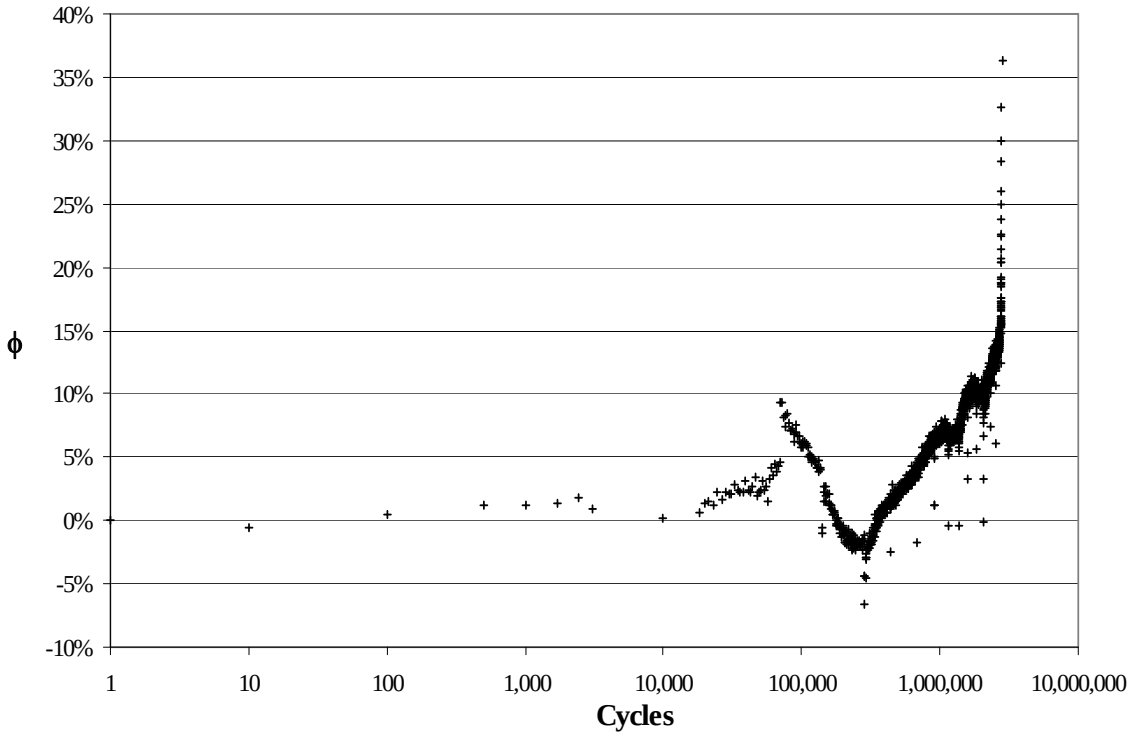

Figure 5.33: Creep coefficient variation vs. cycles of load for B2.

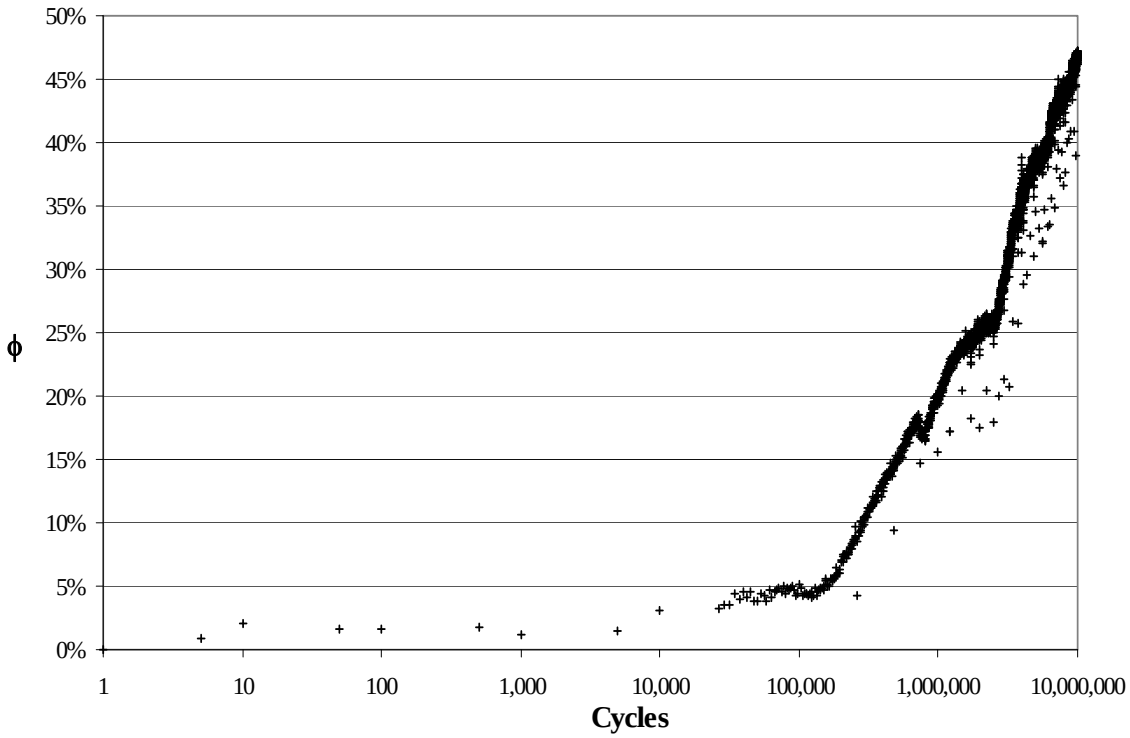

Figure 5.34: Creep coefficient variation vs. cycles of load for B3.

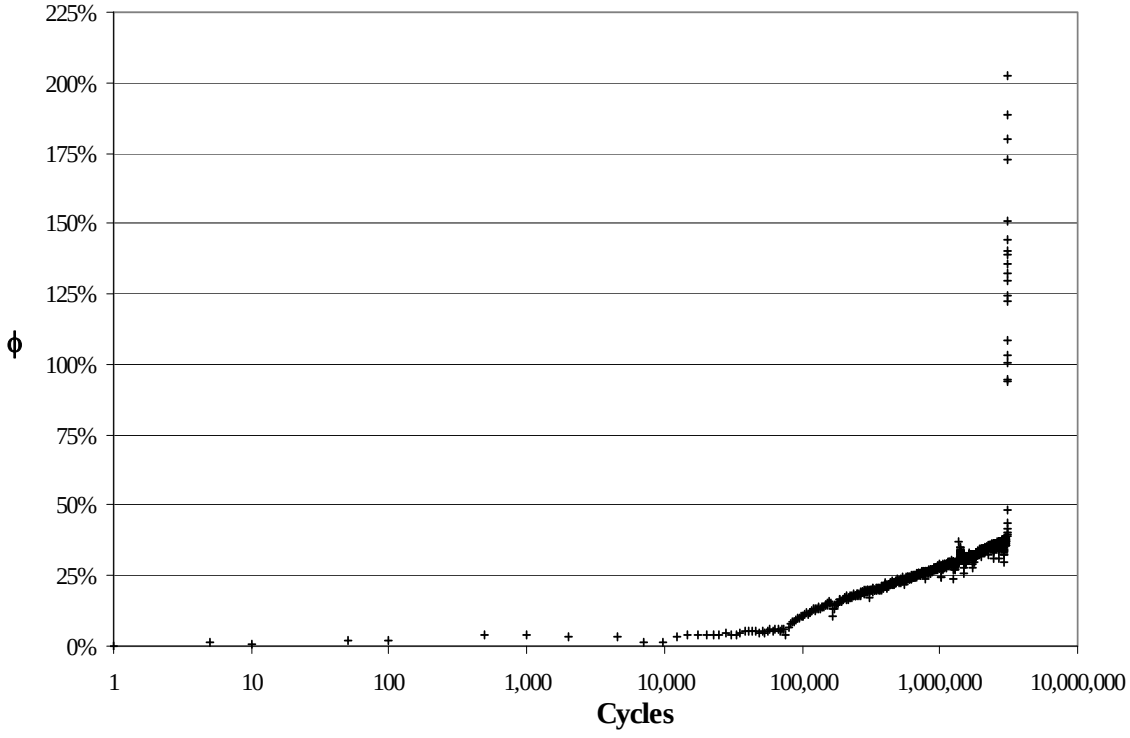

Figure 5.35: Creep coefficient variation vs. cycles of load for B4.

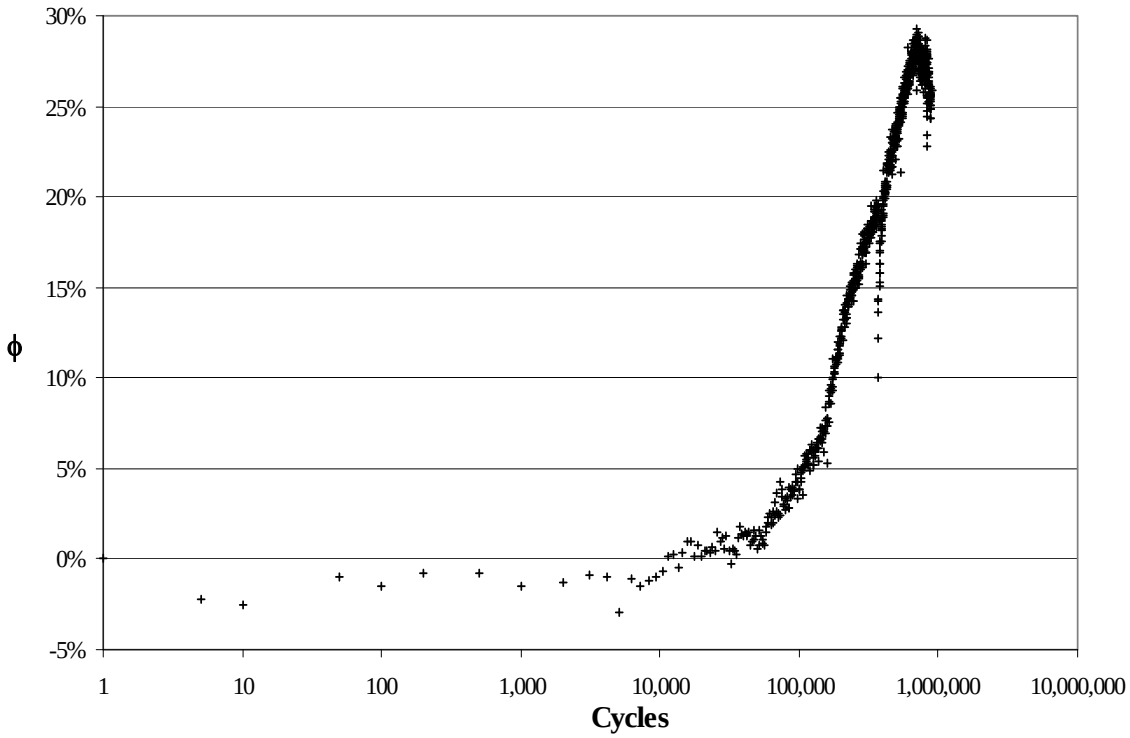

Figure 5.36: Creep coefficient variation vs. cycles of load for B5.

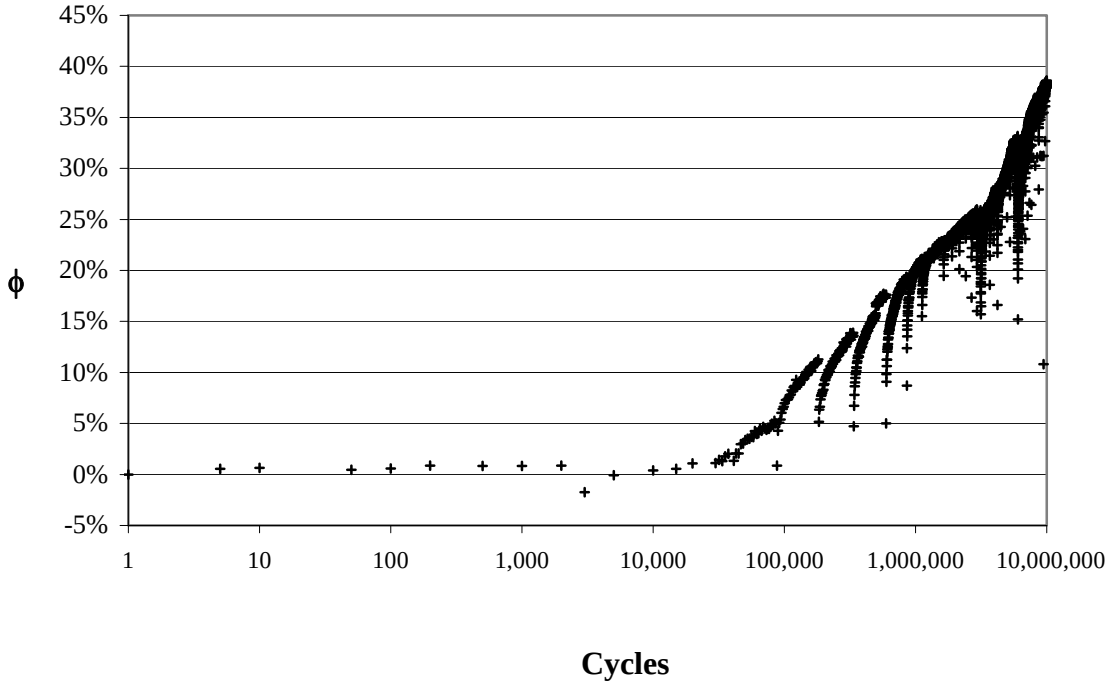

Figure 5.37: Creep coefficient variation vs. cycles of load for B6.

6 SUMMARY and CONCLUSIONS

6.1 Summary

The experimental program consisted of two sets of Sandwich Plate System (SPS) specimens, each with six specimens. Five from each set were tested under dynamic cyclic loads with a point load at mid-span. The remaining specimen was tested under monotonic static load with a four-point loading setup. The material properties were measured by ancillary tests. The ancillary tests included tension coupon, block shear, surface roughness, and torsion tests.

A linear distribution of the bending strain of the SPS was assumed and justified on the basis of static equilibrium. In the elastic range, with a linear distribution of stress, the shear stress distribution was determined. Two models for deflection analysis were explored and compared. The energy model is based on energy principles and the coupled shear wall model is based on static equilibrium principles. The deflections of the SPS beams during fatigue tests increased along with cycles endured which is similar to creep deflection.

6.2 Conclusions

The significant observations and conclusions from the sandwich plate system test program are listed.

1) The experimental data provides no conclusive evidence for stress range or mean stress as the dominating factor for interface fatigue strength from the experimental data.
2) Two fatigue critical locations are observed: the steel surface and the steel-elastomer interface.
3) Favorable interface properties improve interface fatigue strength and remove the interface fatigue as a failure mode.

4) The torsion test shows potential as a quality control tool for interface shear strength and as an alternative fatigue testing method.
5) Data acquisition is currently restricted by instrumentation. Low loading rate tests are needed for proper strain results.
6) The assumption of a linear strain distribution is reasonable. Steel layers provide a portion of the shear resistance.
7) Elastomer material properties are load-rate dependent.
8) The coupled shear wall deflection model provides reasonable estimates of deflection, but the resulting equations are relatively complex.
9) The energy model provides practical deflection equations, but overestimates deflection.
10) The results of the two deflection models are proportional to each other. Consequently, results of one model can approximate the results of the other model by multiplying by a factor.
11) Observed creep deflections were about 50% of the initial elastic deflection at 40 days.

7 REFERENCES

ASA B46.1. (1955). Surface roughness, waviness and lay. ASME.

Barsom, J. M., & Rolfe, S. T. (1999). Fracture and Fatigue Control in Structures: Applications of Fracture Mechanics (3rd ed.). USA: ASTM.

Beer, F. P., & Johnston, E. R. (1992). Mechanics of Materials (2^{nd} ed.). London: McGraw-Hill.

Boresi, A. P., & Sidebottom, O. M. (1985). Advanced Mechanics of Materials (4^{th} ed.). New York: John Wiley & Sons.

Broek, D. (1989). The Practical Use of Fracture Mechanics. Dordrecht: Kluwer Academic.

Ewalds, H. L., & Wanhill, R. J. H. (1989). Fracture Mechanics. London: Edward Arnold.

Intelligent Engineering. (2003). Strength, performance and safety of "SPS" sandwich plate ship structures.

Measurements Group. (1993). "Gauge factor fundamentals".

Miner, M. (1945). Cumulative damage in fatigue. Journal of Applied Mechanics, v12, Sep., pp 159-164.

Naito, K., Hirakata, H., & Fujii, T. (1998). Effect of surface treatment for steel adherends on static and fatigue crack growth of epoxy adhesives. Composite Interfaces, v5, n4, 345-361.

Smith, B. S., & Coull, A.(1991). Tall Building Structures Analysis and Design. New York: John Wiley & Sons.

Stensiö, H., Melander, A., Linder, J., Larsson, M., Gustavsson, A., & Björkman, G. (1999). How defects in an adhesive layer influence the fatigue strength of bonded steel-sheet specimens. Fatigue and Fracture of Engineering Materials and Structures, v22, n5, 421.

Tsai, G. C., Sun, C. T., & Doyle, J. F. (1987) Frequency effects on the fatigue life and damage of graphite/epoxy composites. Journal of Composite Materials, v21, January, 2-13.

Ugural, A. C., & Fenster, S. K. (1995). Advanced Strength and Applied Elasticity (3rd ed.). New Jersey: Prentice Hall.

Vallat, M. F., Schultz, J., & Bistac, S. (1996). Adhesion in polymer/steel sandwiches. Journal of Adhesion, v56, 205-215.

Vincent, L., Chateauminois, A., & Blanchard, C. (1996). New testing methodology for the assessment of fatigue properties of structural adhesives. International Journal of Adhesion and Adhesives, v16, n4, November, 289-299.

Weibull, W. (1961). Fatigue Testing and Analysis of Results. New York: Pergamon Press.